Advances in Image Processing, Optics and Photonics

Research in Computing Science

Research in Computing Science es una publicación trimestral, de circulación internacional, editada por el Centro de Investigación en Computación del IPN, para dar a conocer los avances de investigación científica y desarrollo tecnológico de la comunidad científica internacional. **Volumen 131,** enero del 2017. Tiraje: 500 ejemplares. *Certificado de Reserva de Derechos al Uso Exclusivo del Título* No.: 04-2005-121611550100-102, expedido por el Instituto Nacional de Derecho de Autor. *Certificado de Licitud de Título* No. 12897, *Certificado de licitud de Contenido* No. 10470, expedidos por la Comisión Calificadora de Publicaciones y Revistas Ilustradas. El contenido de los artículos es responsabilidad exclusiva de sus respectivos autores. Queda prohibida la reproducción total o parcial, por cualquier medio, sin el permiso expreso del editor, excepto para uso personal o de estudio haciendo cita explícita en la primera página de cada documento. Impreso en la Ciudad de México, en los Talleres Gráficos del IPN – Dirección de Publicaciones, Tres Guerras 27, Centro Histórico, México, D.F. Distribuida por el Centro de Investigación en Computación, Av. Juan de Dios Bátiz S/N, Esq. Av. Miguel Othón de Mendizábal, Col. Nueva Industrial Vallejo, C.P. 07738, México, D.F. Tel. 57 29 60 00, ext. 56571.

Editor responsable: *Grigori Sidorov, RFC SIGR651028L69*

Research in Computing Science is published by the Center for Computing Research of IPN. **Volume 131**, January 2017. Printing 500. The authors are responsible for the contents of their articles. All rights reserved. No part of this publication may be reproduced, stored in a retrieval system, or transmitted, in any form or by any means, electronic, mechanical, photocopying, recording or otherwise, without prior permission of Centre for Computing Research. Printed in Mexico City, in the IPN Graphic Workshop – Publication Office.

Advances in Image Processing, Optics and Photonics

José Javier Sánchez Mondragón
Rafael Guzmán Cabrera
Miguel Torres-Cisneros (eds.)

SEP
SECRETARÍA DE EDUCACIÓN PÚBLICA

Instituto Politécnico Nacional
"La Técnica al Servicio de la Patria"

Instituto Politécnico Nacional, Centro de Investigación en Computación
México 2017

ISSN: 1870-4069

Instituto Politécnico Nacional (IPN)
Centro de Investigación en Computación (CIC)
Av. Juan de Dios Bátiz s/n esq. M. Othón de Mendizábal
Unidad Profesional "Adolfo López Mateos", Zacatenco
07738, México D.F., México

http://www.rcs.cic.ipn.mx
http://www.ipn.mx
http://www.cic.ipn.mx

Indexed in LATINDEX, DBLP and Periodica

Printing: 500

Printed in Mexico

ISSN 1870-4069

Editorial

This volume of the journal “Research in Computing Science” contains selected papers related to computational image processing, optics and photonics. The papers were carefully chosen by the editorial board on the basis of the at least two reviews by the members of the reviewing committee or additional reviewers. The reviewers took into account the originality, scientific contribution to the field, soundness and technical quality of the papers.

This is a memorable number for the Optics and Photonics community because it includes works presented at the 2017 Latin American Optics and Photonics Workshop held In Guadalajara Jalisco on February 15-26th, 2017. It was held to honor one of the most outstanding Quantum Optics scientist, Prof. J. H. Eberly from the University of Rochester, who has done not only outstanding contributions to the field, but also a strong supporter of our community in the international arena. The Mexican Optics and Photonics workshops have played quite an important catalyzing the growth of our community by partnering with our education graduate programs. By showing the Field Frontier to our youngest community members, by precisely those who created, they have encouraged their further development and leadership onto those areas and research groups. This workshop has continued such tradition and by bestowing such recognition has partially fulfilled a debt to those leaders who adopted our community as his own. The 1982 Optics Workshop held at Cuernavaca Morelos, and published in KINAM, was not only the first one of them, but also a list of the Who is Who of the Optics at the time. Another high point was The Temporal and Spatial Solitons Workshop held at Guadalajara Jal. on January 20-31st, 1997 where was everyone that has to be. In the meantime, we have gone from quite a small community to our current large and fast growing one. Such an effort cannot be sustained without the support of an international community and there is noticeable the academic support of the Optical Society of America and the longstanding support of the Secretaria de Educación Pública and CONACyT. In particular, the 2017 LAOP Workshop was realized with the financial support of the *Secretaría de Educación Pública-Dirección General de Educación Superior* (2016-21-002-080). The works of this volume were presented there by participants.

Those many years have witnessed the growth of the field, from Classic Optics to Optics and Photonics, to express not only the growth of a discipline but also their interests and applications. This number shows that, as far as Optics is concerned, the papers of this volume discuss the polarization of light, Flat convex lens design and measurement of optical scattering in fibers, a Hartman test for aspherical lenses, a rigorous theory for oblique incident Hermite-Gaussian beams, an analysis of the coupling between Fresnel lens and plastic optical fiber and the use of quaternion and rotation matrix to describe the orientation of a camera

As far as photonics is concerned, the papers of this volume describe non-linear transmission and non-invasive methods with applications in medical physics, a proposal for design cloaks using metamaterials and plasmonic structures, a fiber optic sensor for liquid fuel identification, a study entanglement of quantum dots, a comparison on configurations to excite surface plasmons, a generalization of Wootters concurrence for qutrit systems, a method to measure the Stokes vector and the Mueller matrix, a study of nonlinear optical loop mirrors and a discussion on measuring glucose using Raman scattering.

As far as computational applications, the papers of this volume describe digital optical restoration for unfocused images, digital image processing for biological systems, as well as digital image processing of mammography and thermography.

Finally, we would like to thank to the LAOP, Latin American Optics and Photonics, conference and workshops committee for their support during the preparation of this volume.

José Javier Sánchez Mondragón, INAOE, Mexico
Rafael Guzmán Cabrera, UGTO, Mexico
Miguel Torres-Cisneros, UGTO, Mexico

Guest Editors

January 2017

ISSN 1870-4069

Table of Contents

ISSN 1870-4069

Entanglement in Qutrit Systems

J. D. Huerta-Morales

Instituto Nacional de Astrofísica, Óptica y Electrónica (INAOE), Puebla, Mexico

del_hm5@hotmail.com

Abstract. Wootters concurrence is an entanglement measure for bipartite qubit systems. It is defined in terms of a spin inverter. Here, we try to generalize Wootters concurrence for qutrit systems by defining a naïve inverter analogous to the $SU(2)$ qubit inverter given in terms of Pauli matrix σ_y. For qutrits, the corresponding group is $SU(3)$, so the inverter has to be given in terms of Gell-Mann matrices. The naïve inverter proposed here is given in terms of the Gell-Mann matrices analogous to σ_y and we show that it can deliver equivalent information to that given by the formal inverter in just in certain cases.

Keywords: Entanglement, qutrit system.

1 Introduction

Quantum entanglement is a precious resource, thus, there is a need to measure how entangled a quantum systems. Various entanglement measures have been proposed in the literature, but Wootters concurrence is probably the most widely used.

A measure of entanglement in a bipartite qubit system is Wootters concurrence. It is defined in terms of a superoperator that rotates the qutrit spin [1-3]. In this work, we pretend to construct a naïve bipartite qutrit inverter based on Gell-Mann matrices which may be considered as analogous to the superoperator represented by Pauli matrices but, as we will show, is not a proper universal inverter.

Wootters concurrence of a pure state for a qutrit system is defined as follows,

$$C_3(\Psi) \equiv \sqrt{tr(\rho\tilde{\rho})}, \tag{1}$$

where ρ is the density matrix and $\tilde{\rho}$ is given in terms of the naïve inverter,

$$\tilde{\rho} = S_3 \otimes S_3(\rho) = S_y \otimes S_y \rho * S_y \otimes S_y. \tag{2}$$

In this work we study entanglement in a qutrit beam splitter and compare the results produced by the formal inverter and the naïve construction,

$$S_3 \otimes S_3(\rho) = V_3 V_3 [I \otimes I - I \otimes \rho_B - \rho_A \otimes I + \rho], \tag{3}$$

where I is the unitary matrix.

2 Naïve Inverter for a Qutrit System

Let us consider a bipartite qutrit system; a general state vector is given by,

$$|\Psi\rangle_{AB} = \sum_{i,j=0}^{2} C_{ij} |\mathrm{i}\rangle_A \otimes |\mathrm{j}\rangle_B, \tag{4}$$

where the Hilbert space for each qutrit system is span by the vector basis,

$$|2\rangle = \begin{pmatrix} 1 \\ 0 \\ 0 \end{pmatrix}, |1\rangle = \begin{pmatrix} 0 \\ 1 \\ 0 \end{pmatrix} \ and \ |0\rangle = \begin{pmatrix} 0 \\ 0 \\ 1 \end{pmatrix}. \tag{5}$$

We will consider only pure state $\rho = |\Psi\rangle_{AB}\langle\Psi|$, and propose a naïve inverter given in terms of a S_3 superoperator,

$$S_3(\rho) = S_y \rho^* S_y, \tag{6}$$

where the auxiliary matrix is,

$$S_y = \lambda_2 + \lambda_5 + \lambda_7 = \begin{pmatrix} 0 & -i & -i \\ i & 0 & -i \\ i & i & 0 \end{pmatrix}, \tag{7}$$

is choose as an analogous to Pauli matrix σ_y. Of course, this naïve inverter is not the formal inverter corresponding $SU(3)$ but we will choose that it can provide equivalent results in some specific cases.

It is straightforward to calculate Wootters concurrence for the formal inverter,

$$\begin{aligned} C_f(\Psi) \equiv \sqrt{tr(\rho\tilde{\rho})} &= \sqrt{\sum \langle\Psi|\Psi\rangle\langle\Psi|S_3 \otimes S_3(|\Psi\rangle\langle\Psi|)|\Psi\rangle} \\ &= \sqrt{\langle\Psi|S_3 \otimes S_3(|\Psi\rangle\langle\Psi|)|\Psi\rangle}, \end{aligned} \tag{8}$$

and the naïve inverter,

$$\begin{aligned} C_n(\Psi) = \sqrt{\sum \langle\Psi|\Psi\rangle\langle\Psi|S_y \otimes S_y(|\Psi^*\rangle\langle\Psi^*|)S_y \otimes S_y|\Psi\rangle} \\ = \sqrt{\langle\Psi|S_y \otimes S_y|\Psi^*\rangle\langle\Psi|S_y \otimes S_y|\Psi^*\rangle^*} \\ = |\langle\Psi|S_y \otimes S_y|\Psi^*\rangle|. \end{aligned} \tag{9}$$

3 Results

We want to test the results provided by the naïve inverter, which requires less computer resources to calculate, versus those given by the formal inverter. First, we will study a simple test state and, then, we will use as test state the time evolution of two different states under beam splitter dynamics.

3.1 A simple Test State

The first test sate is given by the following expression,

$$|\Psi\rangle = sin\theta|20\rangle + cos\theta|02\rangle. \tag{10}$$

It becomes a separable state for $\theta = 0$ and entangled for all other cases up to a maximum reached at $\theta = \pi/4$. In this case, the density matrix is,

$$\rho = \sin^2\theta\,|20\rangle\langle 20| + sin\theta cos\theta|20\rangle\langle 02| + cos\theta sin\theta|02\rangle\langle 20| + cos^2\theta|02\rangle\langle 02|. \tag{11}$$

We can calculate Wootters concurrence for both the formal and naïve inverter, which are presented in figure 1 where we can see that the formal and naïve inverter, provide the same information in this case.

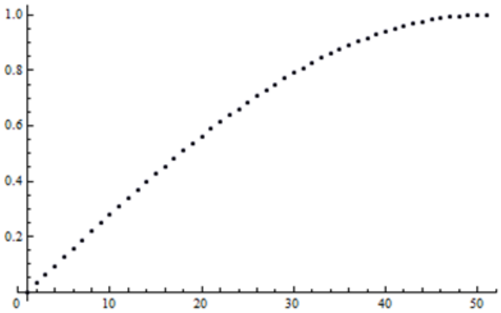

Fig. 1 Wootters concurrence from formal and naive inverter for the test state. The results are identical.

3.2 Beam Splitter

Propagation of two quantized electromagnetic fields through a beam splitter is given the time evolution operator,

$$U(t) = e^{-i\left(a_1^{\dagger}a_2 + a_2^{\dagger}a_1\right)t}. \tag{12}$$

Such that at any given time the state of the two-qutrits are given by,

$$|\Psi(t)\rangle = U(T)|\Psi(0)\rangle. \tag{13}$$

We are interested in the evolution of an initial entangled state,

$$a)\quad |\Psi(0)\rangle = \frac{1}{\sqrt{2}}(|20\rangle + |02\rangle), \tag{14}$$

that yields a time propagated state vector,

$$|\Psi(t)\rangle = \frac{1}{\sqrt{2}}\left(cos^2\theta(t) - sin^2(t)\right)|20\rangle - i2\cos(t)\sin(t)\,|11\rangle \\ + \frac{1}{\sqrt{2}}\left(cos^2\theta(t) - sin^2(t)\right)|02\rangle. \tag{15}$$

The figure 2 shows Wootters concurrences calculated via the formal and naïve inverters, it is possible to see that both measures provide qualitatively the same information.

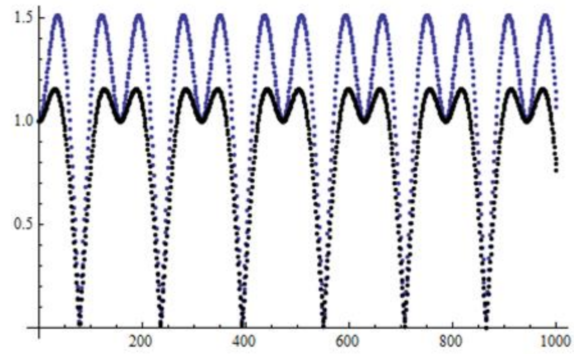

Fig. 2 Wootters concurrence from formal (black dots) and naïve inverter (blue dots) for the test entangled state Eq. (14).

We are also interested in the evolution of an initial separable state,

$$b)\quad |\Psi(0)\rangle = |20\rangle, \tag{16}$$

which yields,

$$|\Psi(t)\rangle = cos^2(t)|20\rangle - i\sqrt{2}\cos(t)\sin(t)\,|11\rangle - sin^2(t)|20\rangle. \tag{17}$$

After calculating the density matrix, we get partial matrices, which are,

$$\rho_A(t) = cos^4(t)|2\rangle\langle 2| + 2cos^2(t)sin^2(t)|1\rangle\langle 1| + sin^4(t)|0\rangle\langle 0|, \tag{18}$$

and,

$$\rho_B(t) = sin^4(t)|2\rangle\langle 2| + 2cos^2(t)sin^2(t)|1\rangle\langle 1| + cos^4(t)|0\rangle\langle 0|. \tag{19}$$

Finally, the Wootters concurrences are:

$$C_f = \frac{1}{8}(13 + 3\cos(4t))sin^2(2t), \tag{20}$$

and

$$C_n = \frac{1}{8}(9 + 7\cos(4t))sin^2(2t), \tag{21}$$

that are shown in figure 3. It is straightforward to notice that the naïve inverter does not provide the same information than the formal inverter in this case.

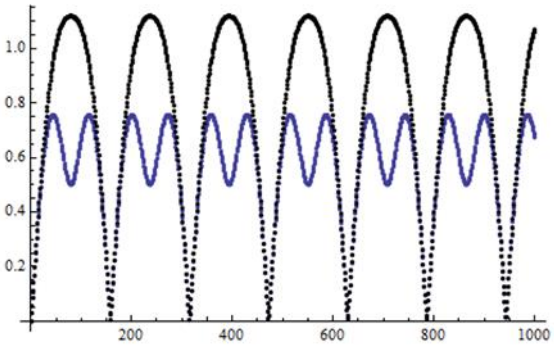

Fig. 3 Wootters the test state in Eq. (16).concurrence from formal (black dots) and naive inverters (blue dots) for the test state in Eq. (16).

4 Conclusions

We have proposed a naïve inverter for bipartite qutrit systems that reduces the computation time used to calculate Wootters concurrence for pure states. This naïve inverter is given in terms of Gell-Mann matrices but it is not a universal inverter. We have shown that in certain cases it provides results that are qualitative equal to those given by the formal inverter but it is not viable for any general state. We will continue exploring entanglement in bipartite qutrit systems through the use of naïve inverters for both pure and mixed states in the future.

Acknowledgments. The author is grateful to his master thesis supervisors, Dr. H. M. Moya Cessa and Dr. B. M. Rodriguez Lara, for their support.

References

1. Rungta, P., Buzek, V., Caves, C. M., Hillery, M., Milburn, G. J.: Phys. Rev. 64, 042315 (2001)
2. Hill, S., Wootters, W. K.: Phys. Rev. Lett. 78, 5022 (1997)
3. Wootters, W. K.: Phys. Rev. Lett. 80, 2245 (1998)

ISSN 1870-4069

Coeficientes de Fresnel para un sistema de conducción multicapa

G. Montiel-González, Juan Sumaya-Martínez, V. M. Galván-Franco

UAEM, Departamento de Óptica de la Facultad de Ciencias, Toluca, México

gmontiel83@yahoo.com.mx

Resumen. Estudiamos las ondas de plasma de superficie de largo alcance encontradas por Sarid usando la configuración de Sarid basada en la reflexión atenuada total (ATR). La influencia de la onda del haz incidente en el acoplamiento con las superficies plasmones se analiza y se compara con los obtenidos utilizando la disposición clásica de Kretschmann. Mostramos que estas ondas superficiales son más sensibles a las características del haz incidente que las ondas superficiales de plasma que excita la configuración de Kretschmann.

Palabras clave: vonducción multicapa, coeficientes de Fresnel.

Fresnel Coefficients for a Multilayer Conducting System

Abstract. We study the long-range surface-plasma waves found by Sarid using the Sarid configuration, based on total attenuated reflection (ATR). The influence of the incident beam wave on the coupling with surfaces plasmons is analyzed and compared with those obtained using the classical Kretschmann arrangement. We show that these surface waves are more sensitive to the characteristics of the incident beam than the surface plasma waves excited by the Kretschmann configuration.

Keywords: multilayer conducting system, Fresnel coefficients.

1. Introducción

Los plasmones de superficie [1] son ondas electromagnéticas con polarización p (T.M.), que se propagan a lo largo de una interfase que separa dos medios, siendo uno de ellos un dieléctrico con constante positiva y el otro un medio metálico con constante dieléctrica compleja y cuya parto real es negativa. Estos modos superficiales también están presentes en medios estratificados, donde pueden estar presentes metales diferentes. Se dice que son ondas de superficie porque su energía está concentrada prácticamente en la interfase. Debido al efecto Joule, su longitud de propagación l es muy corta. A pesar de que esta longitud de propagación es extremadamente pequeña, el estudio de los plasmones de superficie ha sido muy importante en la física del estado sólido, debido principalmente a que las características de su propagación están ligadas a las propiedades de la superficie, disponiéndose así de un método experimental muy eficaz para caracterizar a las superficies metálicas [1].

El estudio de estas ondas de superficie puede llevarse a cabo de dos formas [20]. En una de ellas, se reduce el problema a obtener la relación de dispersión del sistema de películas, la cual es una ecuación que relaciona la frecuencia angular ω de la onda con la constante de propagación α de la misma. Para los metales, esta constante α es compleja, determinando su parte real la velocidad de fase de la onda superficial y su parte imaginaria la longitud de propagación l. En el segundo procedimiento, el cual está más cercano a un estudio experimental, se utiliza el método conocido como reflexión total frustrada para la excitación de los plasmones de superficie. En este método se emplea un prisma en contacto con el sistema estratificado y se hace incidir un haz de luz sobre la interfase que existe entre el prisma y las películas, en condiciones de reflexión total.

Dror Sarid en 1981 encontró que en una película de plata extremadamente delgada (~0.02 µm) y para una longitud de onda λ=0.6328 µm, pueden propagarse un modo simétrico de superficie de largo alcance (l~300 µm) y otro modo asimétrico de corto alcance. Este modo de largo alcance de Sarid se propaga 30 veces más lejos que el modo que existe en una película de plata gruesa, debido a que la energía de la onda se concentra principalmente en el dieléctrico que rodea al metal, reduciéndose así la absorción por efecto Joule. Este plasmón de superficie de largo alcance ha atraído la atención, debido a que su campo eléctrico es muy intenso (~ 60 veces más intenso que el del plasmón de corto alcance). Este intenso campo ha permitido obtener experimentalmente grandes respuestas no lineales, como la generación del segundo armónico y dispersión Raman superficial estimulada (SERS) [3].

En este artículo utilizando la configuración propuesta por D. Sarid [4], basada en la reflexión total atenuada, estudiamos la manera en que las características del haz incidente influyen en la excitación de los plasmones de largo alcance. Para poder apreciar los resultados obtenidos, también analizamos la influencia del haz incidente de la excitación de los plasmones obtenidos con la configuración de Kretschmann. Veremos que los polaritones de largo alcance son, por mucho, más sensibles a las características del haz incidente que los de la configuración de Kretschmann. Consideramos que los resultados de este artículo pueden ser de interés en la excitación de plasmones de superficies en estructuras con dimensiones de algunas longitudes de onda en el vacío.

La teoría que presentamos es general y es adecuada para tratar haces incidentes de cualquier forma con polarización T.E. o T.M. Así, esta teoría también puede ser aplicada en el estudio de ondas guiadas en sistemas estratificados. En particular, en la sección de resultados numéricos supondremos que los haces incidentes o son gaussianos o tienen la forma de un haz Hermite-Gauss [5] [6], estos últimos haces nos servirán para modelar a un haz distorsionado o fuera de foco. De los resultados numéricos concluiremos que los polaritones de largo alcance de Sarid son muy sensibles a la forma del haz incidente y, además, que varios mínimos pueden encontrarse en la reflectividad como función del ángulo de incidencia, dificultando la determinación de la constante de propagación.

2. Teoría para un haz incidente arbitrario

Fijaremos la posición de un punto en el espacio mediante un sistema cartesiano Oxyz. Nuestra configuración consta de n películas homogéneas paralelas al plano Oxz y enumeradas como se ilustra en la Fig. 1.

Cada película está caracterizada por un espesor η_φ y una permitividad compleja ε_j, donde $\varphi = 1, \ldots, n$. El espesor del superestrato y del sustrato es infinito. Así, la primera interfase tiene por coordenada $y_1 = 0$, la segunda interfase $y_2 = -h_2$, la tercera $y_3 = -(h_2 + h_3)$, etc. En lo que sigue admitiremos la dependencia temporal de la forma $\exp(-i\omega t)$ y que un haz independiente de la coordenada z (onda cilíndrica), proviene del medio 1, incide sobre la interfase que separa al medio $\varphi = 1$ del medio $\varphi = 2$.

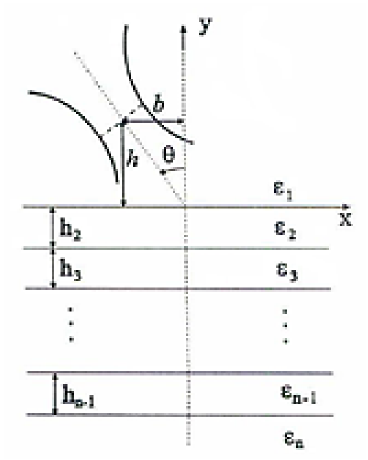

Fig. 1. Nuestro sistema consta de n películas homogéneas paralelas al plano OXZ. Cada película se caracteriza por su espesor h_j y su permitividad compleja ε_j, con j =1,…, n. El espesor del sustrato y el superestrato es infinito. Un haz incide del medio 1 con un ángulo de inclinación θ_0.

Dado que nuestro sistema tiene simetría cilíndrica, en cada película se debe verificar la ecuación escalar de Helmholtz [7]:

$$\frac{\partial^2 U_j}{\partial x^2} + \frac{\partial^2 U_j}{\partial y^2} + k_0^2 \varepsilon_j U_j = 0, \qquad (1)$$

donde $\varphi = 1, \ldots, n$. La función $U_j(x, y)$ depende de la polarización

$$U_j = \begin{cases} E_j & en\ caso\ T.E. \\ H_j, & en\ caso\ T.M. \end{cases} \qquad (2)$$

y k_0 es la magnitud del vector de onda en el vacío $(k_0 = \omega/c)$.

La solución general de la Ec. (1) es

$$\begin{aligned} U_j(x,y) = {} & \frac{1}{\sqrt{2\pi}} \int_{-k_1}^{k_1} A_j(\alpha) exp\big[i\big(\alpha x - \beta_j y\big)\big] d\alpha \\ & + \frac{1}{\sqrt{2\pi}} \int_{-k_1}^{k_1} B_j(\alpha) exp\big[i\big(\alpha x + \beta_j y\big)\big] d\alpha, \end{aligned} \tag{3}$$

donde $k_j^2 = k_0^2 \mathcal{E}_j$ y β_j es alguna raíz de $\beta_j^2 + \alpha^2 = k_0^2 \mathcal{E}_j$. Arbitrariamente seleccionaremos esta raíz de la forma que $\beta_j > 0$ si β_j es real y $Im(\beta_j) > 0$si β_j es compleja. Hacemos notar que cada integrando es una onda plana con vector de onda $(\alpha, \pm\beta_j)$ y amplitud $A_j(\alpha)$ o $B_j(\alpha)$. Luego, el campo $U_j(x,y)$ está expresado como una superposición de ondas planas con parámetro $\alpha \in [-k_1, k_1]$. En la literatura se acostumbra a decir que el campo U_j está expresado mediante un “desarrollo de ondas planas” [7].

La definición de transformada de Fourier en x del campo $U_j(x,y)$ que utilizaremos es

$$U_j(x,y) = \frac{1}{\sqrt{2\pi}} \int_{-\infty}^{\infty} \hat{U}_j(\alpha, y) exp(i\alpha x) d\alpha, \tag{4}$$

y cuya transformada inversa está dada por

$$\hat{U}_j(\alpha, y) = \frac{1}{\sqrt{2\pi}} \int_{-\infty}^{\infty} U_j(x,y) exp(-i\alpha x) dx. \tag{5}$$

Las funciones $A_j(\alpha)$ o $B_j(\alpha)$ no son independientes de las funciones $A_{j+1}(\alpha)$ o $B_{j+1}(\alpha)$, ya que están relacionadas por las condiciones de frontera en la interfase en $y = y_j$, las cuales, en términos de las transformadas de Fourier de los campos, se expresan [7] de la siguiente manera:

$$\hat{U}_j = \hat{U}_{j+1}, \tag{6}$$

$$\frac{1}{\upsilon_j} \frac{\partial \hat{\hat{U}}_j}{\partial y} = \frac{1}{\upsilon_{j+1}} \frac{\partial \hat{\hat{U}}_{j+1}}{\partial y}, \tag{7}$$

donde

$$\upsilon_j = \begin{cases} 1, & en\, caso\, T.E. \\ \mathcal{E}_j, & en\, caso\, T.M. \end{cases} \tag{8}$$

En lo que sigue supondremos que un haz incidente proveniente del medio 1 choca con la interfase 1-2, con esto en mente y considerando que $j = 1$, es fácil identificar a la onda incidente con la primera integral de la Ec. (3):

$$U^{i}(x,y)=\frac{1}{\sqrt{2\pi}}\int_{-k_1}^{k_1}A_j(\alpha)exp\left[i\left(\alpha x-\beta_j y\right)\right]d\alpha, \tag{9}$$

siendo la segunda integral el haz reflejado

$$U^{R}(x,y)=\frac{1}{\sqrt{2\pi}}\int_{-k_1}^{k_1}B_j(\alpha)exp\left[i\left(\alpha x+\beta_j y\right)\right]d\alpha. \tag{10}$$

Por otro lado, el haz transmitido está dado con $j=n$, por

$$U^{T}(x,y)=\frac{1}{\sqrt{2\pi}}\int_{-k_1}^{k_1}A_n(\alpha)exp[i(\alpha x-\beta_n y)]d\alpha, \tag{11}$$

en esta última ecuación hemos supuesto que $B_n(\alpha)=0$, ya que no hay un haz incidente que provenga a través del sustrato desde $y=-\infty$.

Si se admite que el haz sea convergente y se consideran las secciones transversales del mismo, se encontrará que hay una sección transversal mínima. A esta sección transversal mínima se le conoce con el nombre de la cintura del haz, es decir, la cintura es la parte más delgada de un haz convergente.

A partir de la cintura, el haz diverge. Hemos ilustrado estas consideraciones en la Fig. 1, siendo los parámetros b y h los que determinan la posición del centro de la cintura del haz convergente con respecto de los ejes O_y y O_x, respectivamente.

Consideraremos como haz incidente la versión en dos dimensiones de un haz Hermite-Gauss, es decir, consideraremos una onda cilíndrica paralela al eje Oz. A incidencia normal y con el centro de la cintura del haz coincidiendo con el origen de coordenadas $(b=0\ y\ h=0)$, tenemos que sobre la interfase que separa el prisma y la primera película de nuestro sistema estratificado, el campo incidente está dado por [5, 6]:

$$U_n^{i}(x,y=0)=H_n\left(\frac{2x}{L}\right)exp\left(-\frac{2x^2}{L^2}\right), \tag{12}$$

donde H_n es el polinomio de Hermite de orden n y L es el ancho de la gaussiana que interviene en la intensidad sobre la interfase, determinada por el cuadrado de la Ec. (12). Luego, un haz Hermite-Gauss simplemente es un haz cuya sección transversal en $y=0$ está determinada por una gaussiana, pero siendo modulada por un polinomio de Hermite. Así, en el orden más bajo del polinomio de Hermite $n=0$, se tiene un haz gaussiano.

En los resultados numéricos supondremos un haz Hermite-Gausss incidente oblicuamente, pero es difícil generalizar la Ec. (12) a este caso. Es más conveniente obtener la amplitud $A_1(\alpha)$ para un haz con incidencia oblicua, la cual está dada por [5, 6]:

$$A_1(\alpha) = \frac{L}{2}(i)^n H_n\left[-\frac{L}{2}(\alpha cos\theta_0 - \beta_1 sin\theta_0)\right]\left(cos\theta_0 + \frac{\alpha}{\beta_1}sin\theta_0\right) \\ \times exp[-(\alpha cos\theta_0 - \beta_1 sin\theta_0)^2 L^2/8], \tag{13}$$

donde θ_0 es el ángulo de incidencia medido con respecto al eje O_y y como mencionamos el centro de la cintura del haz coincide con el origen de coordenadas $(b = 0 \; y \; h = 0)$.

Como hemos mencionado, en este artículo estamos interesados en el estudio de haces convergentes y su influencia en los plasmones de superficie. En este tipo de haces, el ancho de las secciones transversales cambia con la distancia a lo largo del eje de propagación, teniéndose así un ancho mínimo en la cintura del haz. La Ec. (12) nos indica la forma que aquella para la cual $y = 0$. La transformada de Fourier en x de la Ec. (12) nos proporciona la amplitud $A_1(\alpha)$, la cual al ser introducida en la Ec. (9) nos permite la determinación del haz en todo el espacio. Este último cálculo ha sido realizado numéricamente y el resultado se presenta en la Fig. 2 de la Ref. 16. En esta figura se muestran las curvas de nivel del cuadrado del campo eléctrico, resultando que la forma del haz es muy parecida a la que se ilustra en la Fig. 1 del presente artículo. Finalmente, es importante mencionar que la noción de un haz convergente ha sido considerada por otros autores [15], [16], [19].

3. Solución matricial

En esta sección expresaremos las amplitudes $B_1(\alpha)$ y $A_n(\alpha)$que intervienen en las Ecs. (10) y (11), respectivamente, en términos de la amplitud del haz incidente $A(\alpha)$. Para esto, utilizaremos un método matricial que es susceptible de ser aplicado a un sistema arbitrario de películas. Debemos mencionar que la solución que presentaremos en esta sección difiere de la normalmente utilizada en la literatura, en la cual se supone siempre una onda plana incidente. La teoría de esta sección es adecuada para el tratamiento de un haz arbitrario incidente.

La Ec. (3) puede expresarse de la siguiente forma:

$$\widehat{U}_j(\alpha, y) = A_j(\alpha)exp(-i\beta_j y) + B_j(\alpha)exp(i\beta_j y), \tag{14}$$

y denotaremos como $U_j^-(\alpha, y)$ y $U_j^+(\alpha, y)$ a

$$U_j^-(\alpha, y) = A_j(\alpha)exp(-i\beta_j y), \tag{15}$$

$$U_j^+(\alpha, y) = B_j(\alpha)exp(i\beta_j y). \tag{16}$$

Si tomamos en consideración las condiciones de frontera en $y = y_j$, se tendrá que la solución en la capa j está relacionada a la solución en la capa j+1 por la siguiente expresión matricial

$$\begin{bmatrix} U_j^+(\alpha, y_j) \\ U_j^-(\alpha, y_j) \end{bmatrix} = \begin{bmatrix} \omega_{j,j+1}^+ & \omega_{j,j+1}^- \\ \omega_{j,j+1}^- & \omega_{j,j+1}^+ \end{bmatrix} \begin{bmatrix} U_{j+1}^+(\alpha, y_j) \\ U_{j+1}^-(\alpha, y_j) \end{bmatrix}, \tag{17}$$

donde

$$\omega_{j,j+1}^{\pm} = \frac{\beta_j \nu_{j+1} \pm \beta_{j+1} \nu_j}{2\beta_j \nu_{j+1}}. \tag{18}$$

A la matriz 2 x 2 dada en la Ec. (17) la llamaremos matriz de paso de la capa j a la j+1 y la denotaremos por $T_{j,j+1}$, luego la Ec. (17) se expresa como

$$\begin{bmatrix} U_j^+(\alpha, y_j) \\ U_j^-(\alpha, y_j) \end{bmatrix} = T_{j,j+1} \begin{bmatrix} U_{j+1}^+(\alpha, y_j) \\ U_{j+1}^-(\alpha, y_j) \end{bmatrix}. \tag{19}$$

Por otro lado, para la capa j, se tendrá que la solución en $y = y_{j-1}$ y en $y = y_j$ están relacionadas por

$$\begin{bmatrix} U_j^+(\alpha, y_{j-1}) \\ U_j^-(\alpha, y_{j-1}) \end{bmatrix} = \begin{bmatrix} exp(i\beta_j h_j) & 0 \\ 0 & exp(-i\beta_j h_j) \end{bmatrix} \begin{bmatrix} U_j^+(\alpha, y_j) \\ U_j^-(\alpha, y_j) \end{bmatrix}. \tag{20}$$

A la matriz 2 x 2 la llamaremos matriz de paso en la capa j del punto $y = y_j$ al punto $y = y_j$, y la denotaremos por D_j, expresándose la Ec. (20) así

$$\begin{bmatrix} U_j^+(\alpha, y_{j-1}) \\ U_j^-(\alpha, y_{j-1}) \end{bmatrix} = D_j \begin{bmatrix} U_j^+(\alpha, y_j) \\ U_j^-(\alpha, y_j) \end{bmatrix}. \tag{21}$$

De las Ecs. (19) y (21) se sigue que la solución en la capa j = 1 en $y = y_j$ y, está relacionada a la solución en la capa j = n en $y = y_j$, por

$$\begin{aligned} &\begin{bmatrix} U_1^+(\alpha, y_1) \\ U_1^-(\alpha, y_1) \end{bmatrix} \\ &= T_{1,2} D_2 T_{2,3} D_3 \dots T_{j,j+1} D_{j+1} \dots D_{n-1} T_{n-1,n} \begin{bmatrix} U_n^+(\alpha, y_{n-1}) \\ U_n^-(\alpha, y_{n-1}) \end{bmatrix}. \end{aligned} \tag{22}$$

Denotemos por Q_{1n} al producto de las matrices de paso

$$Q_{1n} = T_{1,2} D_2 T_{2,3} D_3 \dots T_{j,j+1} D_{j+1} \dots D_{n-1} T_{n-1,n} \ , \tag{23}$$

expresándose la Ec. (22) así:

$$\begin{bmatrix} U_1^+(\alpha, y_1) \\ U_1^-(\alpha, y_1) \end{bmatrix} = Q_{1n} \begin{bmatrix} U_n^+(\alpha, y_{n-1}) \\ U_n^-(\alpha, y_{n-1}) \end{bmatrix}. \tag{24}$$

Para el caso particular que trataremos en este artículo, que es cuando un haz incide del medio j = 1, se tiene que $U_n^+(\alpha, y_{n-1}) = 0$. Bajo estas circunstancias la Ec. (24) nos conduce a

$$B_1(\alpha) = r(\alpha)A_1(\alpha), \tag{25}$$

$$A_n(\alpha) = t(\alpha)A_1(\alpha), \tag{26}$$

donde $r(\alpha)$ y $t(\alpha)$ son los coeficientes de Fresnel de reflexión y de transmisión de nuestro sistema, respectivamente, y son dados por

$$r(\alpha) = \frac{(Q_{1n})_{12}}{(Q_{1n})_{22}} \exp(-2i\beta_1 y_1), \tag{27}$$

$$t(\alpha) = \frac{1}{(Q_{1n})_{22}} \exp[i(-\beta_1 y_1 + \beta_n y_{n-1})]. \tag{28}$$

Es interesante hacer notar que a partir de las Ecs. (25) y (26) se obtiene que las amplitudes $B_1(\alpha)$ y $A_n(\alpha)$ que intervienen en las expresiones del campo reflejado y transmitido [Ecs. (l0) y (11)] son proporcionales a la amplitud del campo incidente $A_1(\alpha)$ [7].

4. Resultados

Existen tres configuraciones muy utilizadas, basadas en el método de reflexión total frustrada, para la excitación de los plasmones de superficie [4]: la configuración de Kretschmann, la de Otto y más recientemente la de Sarid. En la configuración de Sarid se tiene una película metálica extremadamente delgada del orden de $0.02\mu m$. En las dos primeras se excitan plasmones de superficie de corto alcance. Mientras que en la configuración de Sarid es posible además de excitar un plasmón de corto alcance, uno de largo alcance para el cual en el visible l es del orden de $300\mu m$. En la Fig. 2 ilustramos la configuración de Kretschmann y de Sarid $(h_3 \sim 0.02\mu m)$.

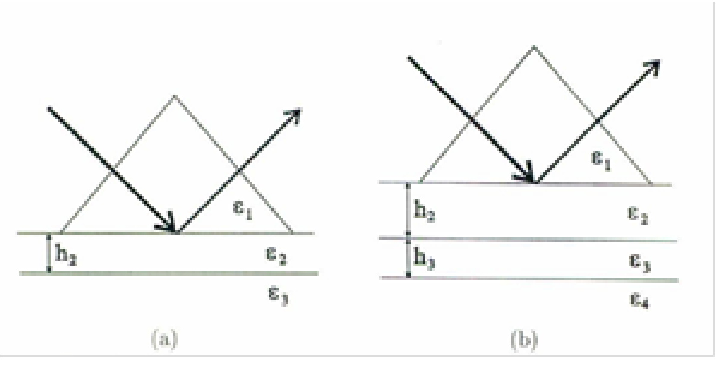

Fig. 2. En la figura (a) mostramos la configuración de Krestchmann, y en la figura (b) la propuesta por Sarid para la excitación de plasmones de largo alcance.

Hasta donde conocemos, la excitación de los plasmones de superficie con las configuraciones de Kretschmann y Sarid, se ha llevado a cabo mediante una onda plana incidente. Por otro lado, los sistemas utilizados actualmente en la óptica integrada o en la optoelectrónica tienden a minimizarse, siendo común tener estructuras del orden de unas cuantas longitudes de onda. Para estas estructuras la noción de una onda plana no tiene sentido y es necesario tomar el caso más realista de un haz incidente muy estrecho. Como se sabe desde hace muchos años, la noción de un haz incidente conduce a nuevos efectos no presentes con ondas planas, siendo uno de ellos el efecto Goos-Hänchen [10]. Con esta idea en mente, es nuestra intención en este artículo investigar si la forma del haz incidente influye o no en la excitación de los plasmones de superficie de largo alcance descubiertos por Sarid. Para poder apreciar los resultados, analizaremos también la influencia del haz incidente en los plasmones de superficie de la configuración Kretschmann.

Es importante hacer un comentario con respecto al diámetro mínimo que un haz puede tener en la práctica. Este diámetro está limitado por los efectos de difracción producidos por los objetivos de los microscopios utilizados para hacer converger el haz. Así, un láser de argón tiene un diámetro mínimo de $1\mu m$ [14] este diámetro es comparable a la longitud de onda del láser de argón. Estos haces extremadamente angostos han sido utilizados en la grabación de discos compactos [14]. En todos los casos considerados a continuación, los parámetros optogeométricos que utilizaremos son los mismos que emplearon J.C. Quail et al., en la Ref. 12, y cuyos resultados experimentales nos servirán de referencia.

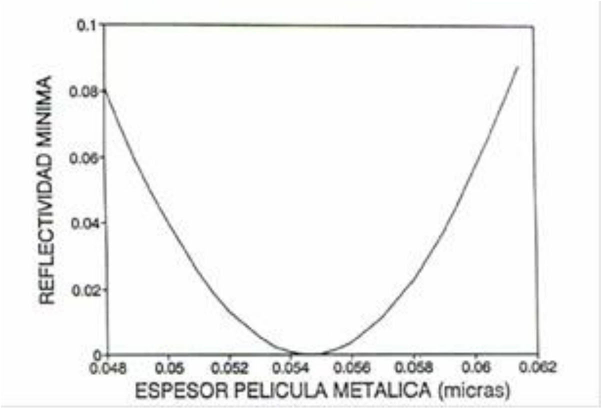

Fig. 3. Determinación del espesor óptico h_{opt} de la película metálica en la configuración de Kreschmann. Graficamos el mínimo de la reflectividad como función del espesor h_2 de la película metálica (en micras). El valor mínimo de la reflectividad se encuentra en h_{opt}=0.0546µm.

El haz incidente tendrá la longitud de onda de un láser He-Ne, $\lambda = 0.6328\,\mu m$. La película metálica es de plata y a esta longitud de onda la permitividad eléctrica es $\varepsilon = -18 + i0.47$. El prisma tiene un índice de refracción $n_1 = 1.4564$. En la configuración de Kretschmann el índice de refracción del sustrato es $n_3 = 1.4569$. En la configuración de Sarid el índice del sustrato es $n_4 = 1.4569$ y el del dieléctrico que se encuentra entre el prisma y la película de plata es $n_2 = 1.4564$. Así que en la configuración de Sarid se tiene el caso de una película casi simétrica, dando lugar a dos modos superficiales, uno simétrico de largo alcance y otro asimétrico de corto alcance.

4.1. Configuración de Khetschmann

Esta configuración está ilustrada en la Fig. 2a. Cuando una onda plana incide a través del prisma en condiciones de reflexión total interna y se varía el ángulo de incidencia θ_0 (medido dentro del prisma), se encuentra que para cierto ángulo θ_{min} , la reflectividad es un mínimo y se dice que hay una resonancia. Para este ángulo de incidencia θ_{min} se tiene que la componente horizontal del vector de la onda incidente k_1 sin θ_{min} coincide con la parte real de la constante de propagación del plasmón de superficie $\alpha'(\alpha' = k_1$ sin $k_1)$ a la frecuencia ω, dando lugar a la excitación del mismo. Por otro lado, la parte imaginaria de la constante de propagación α'' está relacionada con el ancho medio de la resonancia.

Para determinar el espesor óptimo de la película metálica h_{opt}, para el cual la reflectividad es la más pequeña posible y por lo tanto el acoplamiento con el plasmón es el óptimo, variamos h_2 y graficamos la reflectividad mínima para cada valor de h_2. En este cálculo el haz incidente fue una onda plana. Los resultados se muestran en la Fig. 3, resultando que el espesor óptimo es h_{opt} = 0.0546µm. Para este espesor, la reflectividad es muy pequeña $R = 2.56 \times 10^{-5}$, cuando el ángulo de incidencia es $\theta_{min} = 53.000°$.

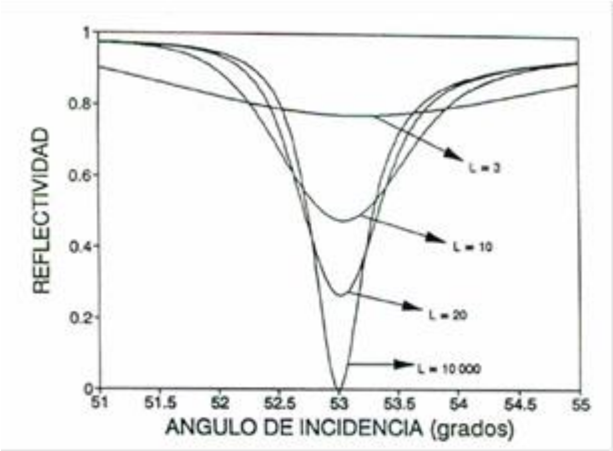

Fig. 4. Influencia del ancho L de un haz gaussiano incidente en el acoplamiento con el plasmón de superficie obtenido con la configuración de Kretschmann. Se consideran los siguientes anchos: L= 10000 µm (onda plana), L= 20 µm, L= 10 µm y L= 3µm. El espesor de la película metálica es h_{opt} = 0.0546µm.

En la Fig. 4 mostramos cómo influye el ancho L de un haz gaussiano [n=0 en la Ec. (12)] en el acoplamiento con el plasmón de superficie. Como puede verse en esta figura el acoplamiento para L=10000µm (onda plana) es excelente, ya que la reflectividad es casi nula, sin embargo este acoplamiento se degrada cuando el ancho disminuye. Hemos encontrado que existe un ancho mínimo L_{min}

($L_{\min} = 150\mu m$ o en unidades de longitud de onda $L_{\min}/\lambda = 237$) a partir del cual la reflectividad, como función del ángulo de incidencia, es prácticamente la misma que la producida por una onda plana incidente, es decir, cuando $L > L_{\min}$ la reflectividad es insensible al ancho de la gaussiana incidente. Así, para $L < L_{\min}$ y conforme el ancho de la gaussiana disminuye el acoplamiento se empeora, dando por resultado que el plasmón de superficie se lleve menos energía incidente, como puede observarse del aumento del mínimo, y además, el ancho angular de la resonancia aumenta. Hemos determinado la constante de propagación para la interfase dieléctrico-metal que estamos considerando y hemos obtenido $\alpha = \alpha' + i\alpha'' = 15.3956 + i0.02682$. Para este caso la longitud de propagación es $\ell = 1/\alpha'' = 37.28\mu m$. De la Fig. 4 obtenemos que la posición angular de todos los mínimos es la misma $\theta_{\min} = 53.000°$, luego, tenemos que $\alpha' = k_1 \sin\theta_{\min} = 15.4095$, valor muy cercano al de la parte real de α. Así obtenemos el importante resultado para haces gaussianos: que el mínimo en la reflectividad nos conduce al valor correcto de la parte real de la constante de propagación. Como veremos éste no es el caso en general.

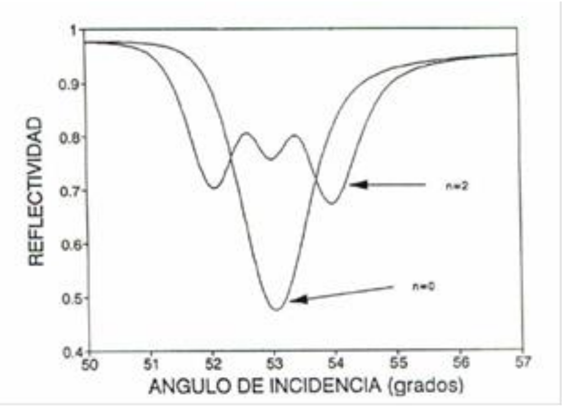

Fig. 5. Influencia de la forma del haz incidente en la excitación del plasmón de superficie de la configuración de Krestchmann. El haz incidente es un haz Hermite-Gauss, con n=2 y ancho L= 10μm. Se presenta también el resultado de un haz incidente gaussiano (n=0) del mismo ancho.

Podemos dar una explicación al resultado obtenido de la Fig. 4, el cual se enuncia así: cuando L disminuye a partir de un ancho mínimo, el mínimo de la resonancia aumenta, disminuyendo con esto el acoplamiento con el plasmón de superficie. Para $\theta = \theta_{\min}$, cuando L es muy grande con respecto a la longitud de onda, podemos considerar al haz incidente como una onda plana, con vector de onda bien determinado y cuya componente horizontal es $\alpha = k_1 \sin\theta_{\min}$ En términos de la amplitud $A(\alpha)$ podemos decir que esta función es nula para valores diferentes de $\alpha = k_1 \sin\theta_{\min}$, obteniéndose así un perfecto acoplamiento. Pero, cuando L disminuye con $L < L_{\min}$, el haz deja de ser una onda plana, resultando ahora que $A(\alpha)$ es nula fuera de un intervalo en α alrededor de $\alpha = k_1 \sin\theta_{\min}$. Este intervalo es cada vez más grande conforme L disminuye, dando por resultado que más ondas planas sean reflejadas, incrementando con esto el mínimo de la resonancia.

En la Fig. 5 mostramos la influencia de la forma del haz incidente en la excitación del plasmón de superficie obtenido con la configuración de Kretschmann. Consideramos un haz Hermite-Gauss de orden n=2 y de ancho L=10μm. Como comparación superponernos en la misma figura el resultado de la Fig. 4 para una gaussiana (n=0) del mismo ancho. Es notable observar la presencia de tres mínimos en la reflectancia, encontrándose uno de ellos precisamente en la misma posición angular que el mínimo de la gaussiana, $\theta_{\min} = 53.000°$ ¿Cuál es el significado de estos mínimos? La presencia de estos tres mínimos no implica que se estén excitando tres plasmones de superficie diferentes, ya que la relación de dispersión para una interfase dieléctrico-metal contiene una sola rama y así un solo plasmón puede excitarse, siendo el mínimo central el que proporciona la correcta constante de propagación. Este ejemplo nos muestra que cuando se excitan los plasmones con un modo de un láser diferente al fundamental o con un haz distorsionado, es necesario tomar precauciones, ya que obtener la constante de propagación a partir de la posición angular de cualquier mínimo en la reflectividad puede llevar a resultados incorrectos.

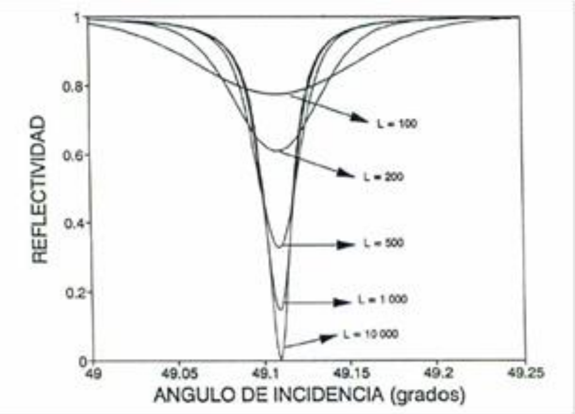

Fig. 6. Influencia del ancho L de un haz gaussiano incidente en el acoplamiento con el plasmón de superficie de largo alcance en la configuración de Sarid. Se consideran los siguientes anchos: L=10000μm (onda plana), L=1000μm, L=500μm, L=200μ y L=100μm. Los espesores de las películas dieléctrica y metálica son h_2=1.28μm y h_3=0.0170μm, respectivamente. Compare el ancho angular de las resonancias con los de la configuración de Kretschmann en la Fig. 4.

4.2. La configuración de Sarid

En la Fig. 2b se muestra la configuración de Sarid. En esta configuración cuando la película metálica es gruesa $\sim 500\dot{A}$, se excitan dos plasmones de superficie de corto alcance, como puede verse en la Fig. lb de la Ref. 12. Sin embargo, cuando el espesor de la película metálica disminuye mucho $\sim 200\dot{A}$, Sarid ha mostrado que se excita un polaritón de largo alcance (modo simétrico) y otro de corto alcance (modo asimétrico). En esta última parte mostraremos la influencia del haz incidente en los plasmones de superficie de largo alcance. Es interesante ver la Ref. 13, en donde se presenta un análisis detallado de los modos de largo alcance que pueden existir en una película delgada.

Hacemos notar que en este artículo no mostramos la influencia del haz incidente en el modo de superficie de corto alcance que se genera con la configuración de Sarid, debido a que las conclusiones son muy parecidas a las que obtuvimos con los plasmones de superficie generados mediante la configuración de Kretschmann.

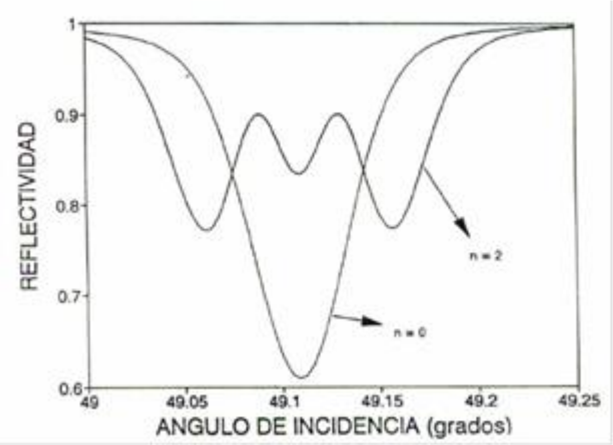

Fig. 7. Influencia de la forma del haz incidente en la excitación del plasmón de superficie de largo alcance de la configuración de Sarid. El haz incidente es un haz Hermite-Gauss, con n=2 y ancho L=200µm. Se presenta también el resultado de un haz incidente gaussiano (n=0) del mismo ancho.

Al igual que con la configuración de Kretschmann hemos optimizado el espesor de la película dieléctrica h_2 y el de la película metálica h_3, y hemos obtenido $h_2 = 1.28\mu m$ y $h_3 = 0.0170\mu m$. En la Fig. 6 mostramos la influencia del ancho de un haz gaussiano en el polaritón de largo alcance. Si comparamos esta figura con la Fig. 4 de la configuración de Kretschmann, concluiremos que el polaritón de largo alcance es más sensible al ancho del haz gaussiano. En este último caso, el ancho mínimo a partir del cual la reflectividad es insensible al ancho de la gaussiana es $L_{\min} = 1500\mu m$, que en términos de la longitud se expresa $L_{\min} = 2370\lambda$. De la Fig. 6, se tiene que para un ancho $L = 500\mu m$ la reflectividad ha subido en un 32% con respecto a la reflectividad (≈0) de una onda plana. Como es de esperarse la posición angular de todos los mínimos coincide en $\theta_{\min} = 49.109°$, dando por resultado que la parte real de la constante de propagación sea $\alpha' = k_1 \sin\theta_{\min} = 14.5860$. También hacemos notar que el pequeño ancho angular $\Delta\theta$ que caracteriza a los plasmones de largo alcance excitados por una onda plana $(\Delta\theta = 0.016° \text{ de la figura})$, se incrementa cuando el ancho del haz disminuye.

En la Fig. 7 mostramos cómo la forma del haz incidente influye en la reflectividad. Consideramos un haz Hermite-Gauss de orden n=2, con L=200µm, como referencia en la misma figura superponemos el resultado de un haz gaussiano con el mismo ancho. De nuevo se tienen tres mínimos, pero sólo el mínimo central nos proporciona la correcta constante de propagación. Es de hacer notar que el ancho angular de la resonancia se ha incrementado notablemente.

5. Conclusiones

En este artículo hemos analizado la influencia de un haz incidente en los polaritones de largo alcance de Sarid. Para esto, hemos utilizado el método de reflexión frustrada. Hemos encontrado que los plasmones de Sarid son, por mucho, más sensibles a la forma del haz incidente que los plasmones de superficie generados con la configuración de Kretschmann. Cuando el haz incidente no es una onda plana, es posible tener varios mínimos en la reflectividad que pueden dificultar la determinación de la constante de propagación.

Referencias

1. Agranovich, V. M., Mills, D. L.: SurJaee Polaritons. North-Holland, Amsterdam (1982)
2. Sarid, D.: Physical Review Letters. 47, pp. 1927 (1981)
3. Deck, R. T., Sarid, D. J.: Opto Soco Am. 72, pp. 1613 (1982)
4. Sarid, D., Deck, R., Craig, A., Hickernell, R., Jameson, R., Fasano, J.: Appl. Optics. 21, pp. 3993 (1982)
5. Zuñiga-Segundc, A., Mata-Méndez, O.: Phys. Rev. B. 46, pp. 536 (1992)
6. Mata-Mendez, O., Chavez-Rivas, F.: Opto Soco Am. A12, pp. 2440 (1995)
7. Mata-Mendez, O.: Rev. Mex. Fís. 38, pp. 850 (1992)
8. Vigoureux, J. M.: J. Opto Soco Am. A8, pp. 1697 (1991)
9. Mata-Mendez, O., Halevi, P.: Phys. Rev. B. 36, pp. 1007 (1987)
10. Regan, J. J., Andersen, D. R.: Computers in Physics. pp. 49 (1991)
11. Quail, J. C., Rako, J. C., Simon, H. J.: Opt. Lett. 8, pp. 377 (1983)
12. Yang, F., Sambles, J. R., Bradberry, G. W.: Phys. Rev. B. 44, pp. 5855 (1991)
13. Burstein, E., Chen, W. P., Chen, Y. J., Hartstein, A. J.: Vaco Sci. Technol. 11, pp. 1004 (1974)
14. Bloembergen, N.: Rev. Mex. Fís. 40, pp. 175 (1994)
15. Mata-Mendez, O., Chavez-Rivas, F.: Rev. Mex. Fís. 39, pp. 371 (1993)
16. Krieziz, E. E., Pandelakis, P. K., Papagiannakis, A. G.: J. Opt. Soc. Am. A. 11, pp. 630 (1994)
17. Hodgson, N., Haase, T., Kostra, R., Weber, H.: Optical and Quantum Electronics. 24, pp. 927 (1992)
18. Kraus, H. G.: J. Opt. Soc. Am. A7, pp. 47 (1990)
19. Belland, P., Crenn, J. P.: Appl. Optics. 21, pp. 522 (1982)
20. Halevi, P.: Polaritons at the interface between two dielectric media. In: Electromagnetic SurJace Modes, Editor A.D. Boardman, John Wiley & Sons Ltd, Cap.7 (1982)

ISSN 1870-4069

Conversion cuántica de frequencia

Oscar Adrián Jiménez Gordillo[1], Yiming Lai[2], Antonio Badolato[2]

[1] Instituto Nacional de Astrofísica, Óptica y Electrónica, Coordinacion de Óptica, Puebla,
México

[2] University of Rochester, Physics and Astronomy Department, New York,
E.U.A

oscar.jimenez@inaoep.mx, badolato@pas.rochester.edu

Resumen. La conversión de frecuencia cuántica de estados de luz no clásicos permite la integración de diferentes sistemas cuánticos que funcionan a diferentes energías. El proceso de conversión consiste en combinar dos campos ópticos en un medio no lineal para generar un tercer campo que es igual a la suma de las dos entradas. Para cumplir con la conservación de impulso requerida por este proceso, necesitamos compensar la falta de correspondencia del vector de onda entre los haces de salida y de entrada. Esto se logra mediante el uso de una rejilla en el medio no lineal, un proceso llamado cuasi-coincidencia de fase. En este trabajo usaremos una guía de ondas Lithium Niobate LiNbO3 (PPLN) polarizada periódicamente como el material no lineal. Nuestro objetivo es desarrollar una conversión de frecuencia cuántica de alta eficiencia, baja pérdida y alta fidelidad. El objetivo específico es transducir fotones emitidos por puntos cuánticos desde longitudes de onda NIR (λ> 1.1 μm) a longitudes de onda visibles (<0.70 μm), donde los detectores de silicio de fotón único rinden mejor.

Keywords: conversion cuántica, frequencia.

Quantum Frequency Conversion

Abstract. Quantum frequency conversion of non-classical states of light allows the integration of different quantum systems working at different energies. The conversion process consists in combining two optical fields in a nonlinear medium to generate a third field that is equal to the sum of the two inputs. To fulfill the momentum conservation required by this process, we need to compensate for wave vector mismatch between the output and input beams. This is achieved by using a grating in the nonlinear medium, a process named quasi-phase matching. In this work we will use a periodically poled Lithium Niobate LiNbO3 (PPLN) waveguide as the nonlinear material. We aim to develop high efficiency, low loss, and high fidelity quantum frequency conversion. The specific objective is to transduce photons emitted by quantum dots from NIR wavelengths (λ > 1.1 μm) to visible wavelengths (< 0.70 μm), where single photon silicon detectors perform best.

Keywords: Quantum conversion, frequency.

1. Introducción

De una manera simple, la conversión cuántica de frecuencia (CCF) describe los métodos mediante los cuales la longitud de onda de un fotón es cambiada sin destruir su estado cuántico (Ates, 2012). De manera más precisa, en un dispositivo de QFC, el estado cuántico de un fotón de entrada con una longitud de onda λa, es transferido a un fotón de salida con λb, donde el fotón con λa es aniquilado y el fotón con λb es creado (Boyd, 1968). Para este fin, se utilizan las no linealidades intrínsecas en cristales de estado sólido (Fejer, 1992). El proceso de conversión tiene que ser bombeado por uno o dos láseres de bombeo bastante potentes. Se denomina conversión de bajada cuando la longitud de onda de entrada es más corta que la de salida (λa < λb) y conversión de subida cuando ocurre el caso contrario.

La CCF fue propuesta por primera vez por Kumar (1990) y fue demostrada experimentalmente dos años después por Huang y Kumar (1992). Los autores demostraron correlaciones de intensidad no clásicas entre el haz de entrada y el haz convertido.

Grupos como el de Kwiat (2004), Wong (2004) y Fejer (2004) han investigado la conversión de frecuencia para solucionar el problema de la ineficiencia de los detectores de fotones con longitud de onda en el rango de telecomunicaciones. Más adelante, Tanzilli et al. (2005) reportaron un experimento en el que demostraron que el entrelazamiento de energía-tiempo entre dos qubits fotónicos se mantenía durante la conversión de frecuencia de subida. El objetivo de este trabajo es desarrollar conversión cuántica de frecuencia altamente eficiente para convertir fotones emitidos por puntos cuánticos con longitudes de onda mayores que 1.1μm (en el infrarrojo cercano) a longitudes de onda menores que 0.70μm (en el visible), donde los detectores de fotones individuales de silicio tienen mejor rendimiento.

2. Materiales y métodos

Para lograr los objetivos de este trabajo se utilizará como material no lineal una guía onda de Niobato de Litio (LiNbO3) periódicamente polarizada (PPLN-WG) de 4cm de longitud para llevar a cabo el proceso no lineal de generación de suma de frecuencias (GSF). La polarización periódica de la guía de onda es necesaria para lograr la condición de cuasi-adaptación de fase (QPM) con la que satisface la conservación de momento requerida por este proceso.

Este trabajo constituye la primer etapa del proyecto que consiste en la caracterización de la PPLN – WG y para esto se utilizará un láser New Focus TLB-6700 a 1175nm como la señal a convertir y un láser semiconductor ajustable Santec TLS-150 a 1560nm como fuente de bombeo, las altas potencias necesarias se lograrán amplificante este mediante un amplificador de fibra óptica dopada con Erbio (EDFA) de la marca Amonics AEDFA-B.

En la Fig. 1 se muestran las dimensiones físicas del dispositivo que contiene la guía de onda fabricado por la empresa NTT Electronics. El dispositivo cuenta con 12 guías de onda y para este trabaja se escogió la de nombre WG1 del grupo 2, en la Tabla 1 se muestran sus especificaciones.

Tabla 1. Especificaciones de la guía de onda utilizada dadas por el fabricante.

Grupo	Periodo de polarización (μm)	Grosor (μm)	Guía de onda	Altura (μm)	Temperatura de acoplamiento de fase (ºC)
G2	13.160	9.4	WG1	11.9	54

La temperatura del dispositivo PPLN-WG tiene que ser cuidadosamente controlada para que se cumpla la condición de QPM. En este trabajo se utiliza como elemento térmico un enfriador termoeléctrico (TEC) conectado a un controlador de temperatura (Thorlabs TED 200 C) y la temperatura es detectada mediante un termistor.

Se cuenta con un elemento polarizador para cada láser ya que ambos tienen que tener la misma polarización para que se lleve a cabo el proceso no lineal de GSF. En la Figura 8 se puede observar el arreglo experimental de este trabajo.

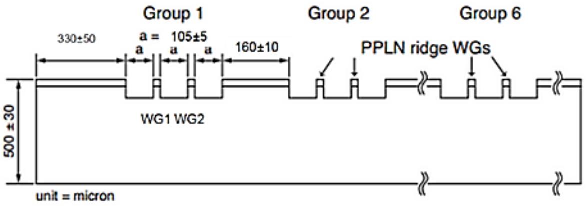

Fig. 1. Diagrama del dispositivo que contiene las guías de onda.

3. Resultados

En esta sección se presentan los resultados de esta primera etapa del proyecto que consiste en la caracterización y rendimiento de la PPLN-WG.

3.1. Potencia de salida

En las siguientes figuras se muestra la potencia obtenida de la luz convertida a la salida del dispositivo.

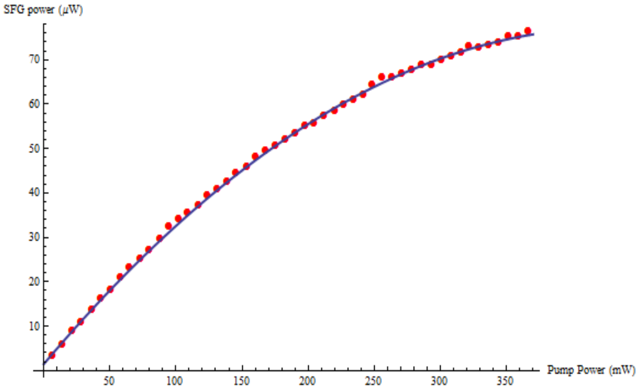

Fig. 2. Generación de GSF con potencia de señal constante a 0.111mW.

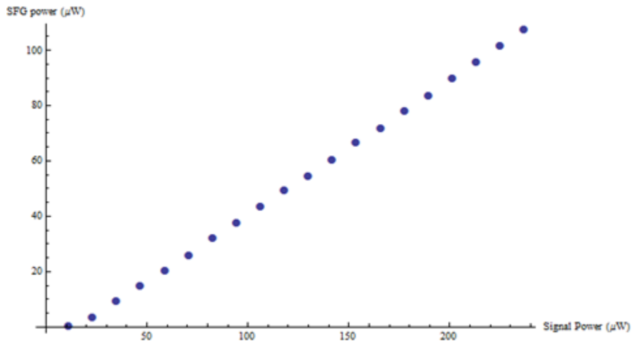

Fig. 3. Generación de GSF con potencia de bombeo constante a 170mW.

3.2. Eficiencia de conversión

En las siguientes figuras se muestra cómo varía la eficiencia de conversión (Potencia de la señal a la entrada de la PPLN-WG / Potencia de la luz convertida a la salida de la PPLN-WG) para diferentes valores de potencia de la señal y del bombeo.

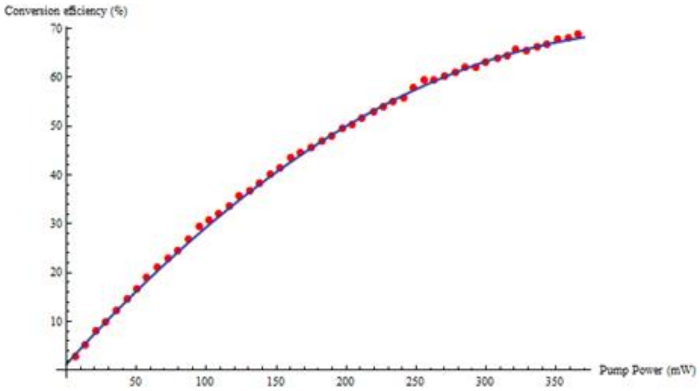

Fig. 4. Eficiencia de conversión con potencia de señal constante a 0.111Mw.

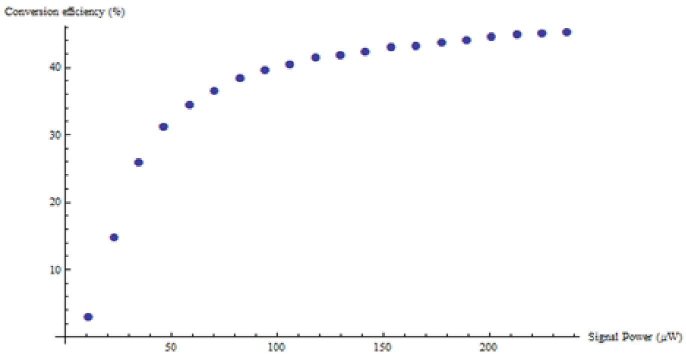

Fig. 5. Eficiencia de conversión con potencia de bombeo constante a 170mW.

3.3. Ancho de banda espectral

En la siguiente figura se muestran los datos experimentales de las mediciones utilizadas para obtener el ancho de banda espectral del dispositivo. Los procesos no lineales de segundo orden poseen cierto ancho de banda de acoplamiento de fase que sigue un comportamiento de la función Sinc2. Dentro de este ancho de banda, la conversión de longitud de onda ocurre y porciones significativas de la potencia de entrada se distribuyen a campos de luz con otras frecuencias. A partir del ajuste a la función Sinc2 se obtuvo un ancho de banda espectral de 0.38nm de la anchura a media altura (FWHM).

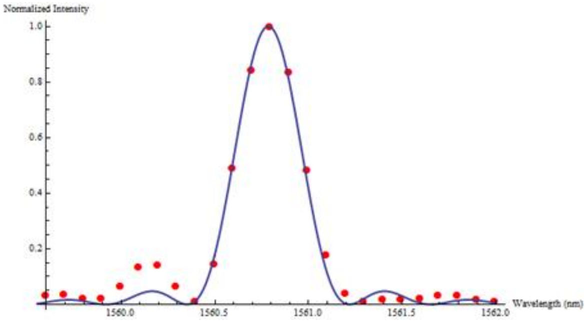

Fig, 6. Ancho de banda espectral de SFG para la PPLN-WG.

3.4. Ancho de banda de temperatura

En la siguiente figura se muestran los datos experimentales de las mediciones utilizadas para obtener el ancho de banda de temperatura del dispositivo. La condición de QFM es altamente sensible a la temperatura del dispositivo, por lo que es necesario conocer su ancho de banda de temperatura para lograr un buen control de esta y evitar tener variaciones importantes en la eficiencia de conversión.

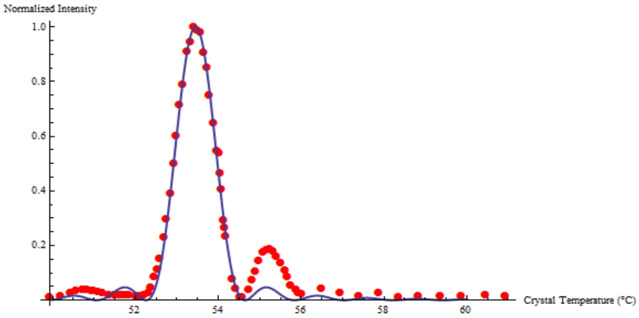

Fig. 7. Ancho de banda de temperatura de la PPLN-WG. Los datos están normalizados con respecto al máximo central.

Esta medición se llevó a cabo fijando los dos láseres de entrada (bombeo a 1560.775nm y 170mW y el de señal a 1174.9nm y 0.111mW) y variando la temperatura del dispositivo. Se obtuvo un ancho de banda de temperatura de 1.06°C (FWHM) del ajuste a la función Sinc^2.

4. Discusión

La caracterización del rendimiento del dispositivo no lineal PPLN-WG es una etapa muy importante para el desarrollo de la conversión cuántica de frecuencia ya que esta nos dará los parámetros básicos para trabajar posteriormente de manera óptima con fotones individuales.

Con los resultados obtenidos en la Figura 4 se observa claramente que a medida que el aumento de la potencia de la luz convertida es directamente proporcional al aumento de las potencias de entrada. Al aumentar la potencia de bombeo se llega eventualmente a un punto en que no se puede obtener más potencia a la salida del dispositivo. El aumento de la potencia de la señal de entrada tiene un efecto lineal en el aumento de la potencia de la luz convertida como se puede ver en la gráfica del lado derecho.

Partiendo de los resultados descritos en el párrafo anterior, se obtuvieron los valores de la eficiencia de conversión del dispositivo. Se intenta obtener la mayor eficiencia posible y esto depende de muchas variables como lo son la temperatura, la potencia de bombeo, la potencia de la señal, el acoplamiento de la luz dentro de la guía de onda, las imperfecciones de la guía de onda, el ancho de banda espectral, entre otras. La mayor eficiencia de conversión lograda con este arreglo experimental fue casi del 70%. Hay bastante campo para mejorar esta eficiencia, sobretodo poniendo atención a las pérdidas provocadas por los elementos ópticos, especialmente en la etapa de filtrado de la señal.

El ancho de banda espectral obtenido a partir del ajuste de la gráfica en la figura 6 es un parámetro sumamente importante ya que el ancho de banda de las señales de entrada debe ser menor a este para que se cumpla eficientemente la condición de QPM. Hay que tomarlo en cuenta a la hora de elegir las fuentes de entrada de nuestro dispositivo.

El ancho de banda de temperatura obtenido nos da bastante flexibilidad ya que la precisión de control de temperatura de nuestro controlador es de 0.01◦C.

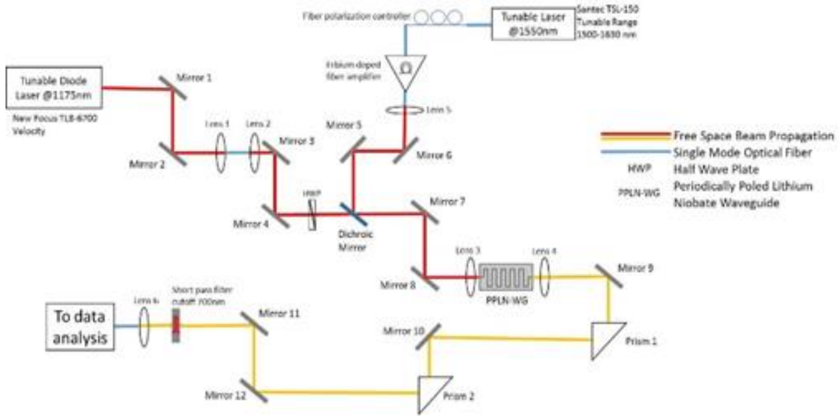

Fig. 8. Arreglo experimental.

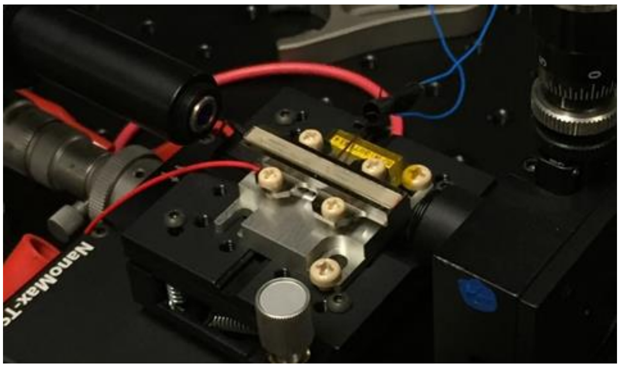

Fig. 9. Fotografía de la PPLN-WG.

5. Conclusiones

Esta primera etapa del proyecto de QFC permite establecer los parámetros de operación del dispositivo PPLN-WG para posteriormente lograr una conversión de frecuencia cuántica altamente eficiente. El siguiente paso es conocer el comportamiento del dispositivo con una señal de entrada de un láser atenuado simulando una fuente de fotones individuales para finalmente usar una verdadera fuente de fotones individuales provenientes de un punto cuántico localizado en la cavidad de un cristal fotónico y demostrar una interfaz cuántica capaz de convertir fotones con longitudes de onda en el infrarrojo a longitudes de onda en el visible conservando sus propiedades cuánticas.

Agradecimientos. Oscar Jiménez agradece especialmente a su asesor en el INAOE y a la beca mixta CONACYT asignada para poder realizar este trabajo de investigación en la Universidad de Rochester.

Referencias

1. Albota, M. A., Wong, F. N. C.: Efficient single-photon counting at 1.55 µm by means of frequency upconversion. Opt. Lett., 29, pp. 1449–1451 (2004)
2. Ates, S., Agha, I., Gulinatti, A., Rech, I., Rakher, M.T., Badolato, A., Srinivasan, K.: Two-Photon Interference Using Background-Free Quantum Frequency Conversion of Single Photons Emitted by an InAs Quantum Dot. Phys. Rev. Lett., 109, 147405.8 (2012)
3. Boyd, G. D., Kleinman, D. A.: Parametric interaction of focused Gaussian light beams. J. Appl. Phys., 39, pp. 3597–3639 (1968)
4. Fejer, M. M., Magel, G. A., Jundt, D. H., Byer, R. L.: Quasi-phase-matched second harmonic generation – tuning and tolerances. IEEE J. Quantum Electron, 28, pp. 2631–2654 (1992)
5. Huang, J., Kumar, P.: Observation of Quantum Frequency Conversion. Phys. Rev. Lett., 68, pp. 2153–2156 (1992)
6. Kumar, P.: Quantum frequency conversion. Opt. Lett., 15, pp. 1476–1478 (1990)
7. Roussev, R. V., Langrock, C., Kurz, J. R., Fejer, M. M.: Periodically poled lithium niobate waveguide sum-frequency generator for efficient single-photon detection at communication wavelengths. Opt. Lett., 29, pp. 1518–1520 (2004)

8. Tanzilli, S., Tittel, W., Halder, M., Alibart, O., Baldi, P., Gisin, N., Zbinden, H.: A photonic quantum information interface. Nature, 437, pp. 116–120 (2005)
9. VanDevender, A. P., Kwiat, P. G.: High efficiency single photon detection via frequency up-conversion. J. Mod. Opt., 51, pp. 1433–1445 (2004)
10. Zaske, S., Lenhard, A., Becher, C.: Efficient frequency downconversion at the single photon level from the red spectral range to the telecommunications C-band. Opt. Express, 19, pp. 12825–12836 (2011)

ISSN 1870-4069

Polarimetry of Light Using Analysis of the Nonlinear Voltage-Retardance Relationship for Liquid-Crystal Variable Retarders

Juan Manuel Lopez-Tellez, Neil C. Bruce

Centro de Ciencias Aplicadas y Desarrollo Tecnológico,
Universidad Nacional Autónoma de Mexico, Ciudad de Mexico, Mexico

jmlopez@comunidad.unam.mx

Abstract. We present a method for using liquid-crystal variable retarders (LCVR's) with continually varying voltage to measure, both, the Stokes vector of a light beam and the complete Mueller matrix of a general sample.

Keywords: nonlinear voltage-retardance relationship, polarimetry of light.

1 Introduction

The measurement of the polarization of light is well established [1-3]. Recently, more use has been made of variable retarders, for example, liquid crystal retarders or electro-optic cells which have changes of the retardance depending on the voltage applied to the system. The LCVR's are usually employed with fixed retardance values due to the nonlinear voltage-retardance behavior that they show. For the measurement method presented here, the nonlinear voltage-retardance relationship is first measured and then a linear fit of the known retardance terms to the detected signal is performed. We use known waveplates (half-wave and quarter-wave) as devices to provide controlled polarization states to the Stokes polarimeter, and we use the measured Stokes parameters as functions of the orientation of the axes of the waveplates as an indication of the quality of the polarimeter. In addition, we present results of simulations for comparison. Also, we have used this technique to measure the complete Mueller matrix of a general sample. For a gap of air, the measurement error in the Mueller-matrix polarimeter is estimated at 1–10%, depending on the Mueller-matrix element. For this case, we present experimental results for a Glan–Thompson prism polarizer as a test sample, and we use the measured Mueller parameters as functions of the orientation of the optical axes of the polarizer as an indication of the quality of the polarimeter.

2 Stokes Polarimeter

Figure 1 shows the set-up used for the Stokes polarimeter. The light to be analyzed passes through two liquid crystal variable retarders with their axes at 45 degrees to each other and finally through a linear polarizer with its transmission axis parallel to the axis

pp. 37–42; rec. 2017-05-17; acc. 2017-11-18

of the first retarder. The idea of this method is to adjust the detected intensity, I, to a linear combination

$$I = A + B\cos(\delta_2) + C\sin(\delta_1)\sin(\delta_2) + D\cos(\delta_1)\sin(\delta_2). \qquad (1)$$

So, we have

$$A = \frac{1}{2}S_0^{in}, \qquad B = \frac{1}{2}S_1^{in}, \qquad C = \frac{1}{2}S_2^{in}, \qquad D = \frac{1}{2}S_3^{in}, \qquad (2)$$

where S_0^{in} $S_1^{in}S_2^{in}$and S_3^{in}; are the components of the Stokes vector of the incident light beam, S^{in}. The development of the above equations and, also, details on the experimental set-up for the Stokes polarimeter are shown in [4].

Fig. 1. The set-up for a Stokes polarimeter. The angles associated with each component refer to the relative angle of the optical axis of that component. ω1 and ω2 are the frequencies of the variations of the retardances.

In this case, we have applied a voltage signal which has the form of a linear ramp (saw tooth), this is

$$V = V_{\min} + (V_{\max} - V_{\min})\,\mathrm{mod}\left(\frac{t}{t_i}\right), \qquad (3)$$

and the retardance, δ, is given by the nonlinear relationship of figure 2.

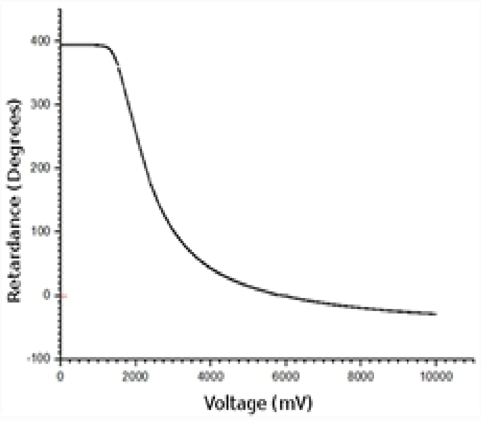

Fig. 2. Retardance vs. voltage for a typical liquid crystal retarder for a wavelength of 633nm [5, 6].

From a characterization previously performed on our LCVR's, figure 2 [5, 6], we know all the retardance (δ) values employed during the measurements. We have measured the Stokes vector of light passing through a linear polarizer and a half-wave retarder, as the retarder is rotated, and also for a linear polarizer and a quarter-wave retarder as the retarder is rotated. In the first case the polarization measured should shift between S1 (horizontal/vertical linear polarization) and S2 (+45 degrees/-45 degrees linear polarization), and in the second case the polarization should shift between linear and circular S3 polarization. Results of calculation for these cases give the curves shown in figure 3. The experimental results are shown in figure 4 for these two cases. It can be seen that the behavior of the results is, in general, as expected, although there are some small asymmetries in the curves, and noise. The measurement time for each Stokes vector was 1.8 seconds.

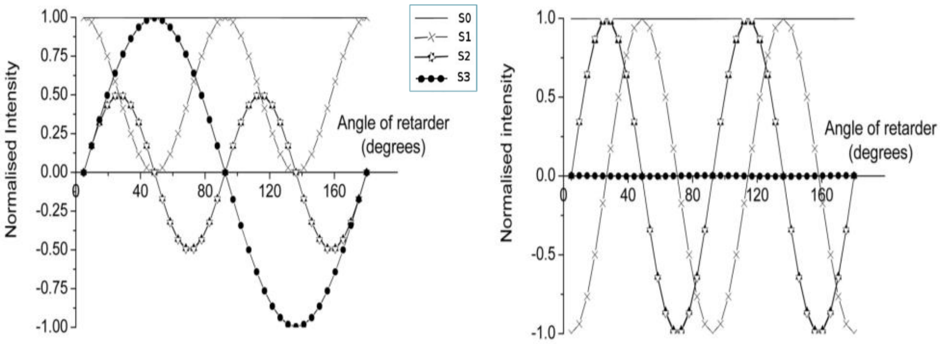

Fig. 3. Simulation of the Stokes vector of light passing through a linear polarizer and a quarter-wave plate (left) and also for a linear polarizer and a half-wave plate (right).

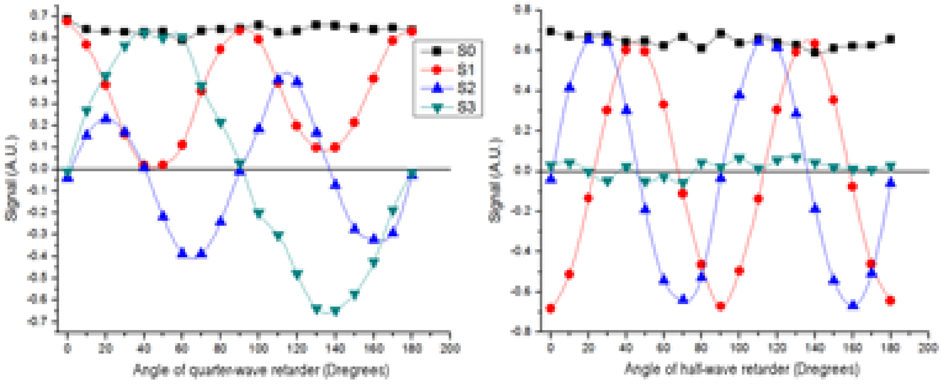

Fig. 4. Experimental measurements of the Stokes vector of light using a fitting procedure. The light is passing through a linear polarizer and a quarter-wave plate (left) and also for a linear polarizer and a half-wave plate (right).

3 Mueller Polarimeter

A Mueller matrix polarimeter is an instrument designed and built to measure the 16 elements of the Mueller matrix. Figure 5 shows the set-up for the Mueller matrix polarimeter using LCVR's. This device consists of two modules: a polarization state generator (PSG) and a polarization state analyzer (PSA). The sample under test is analyzed between those two modules.

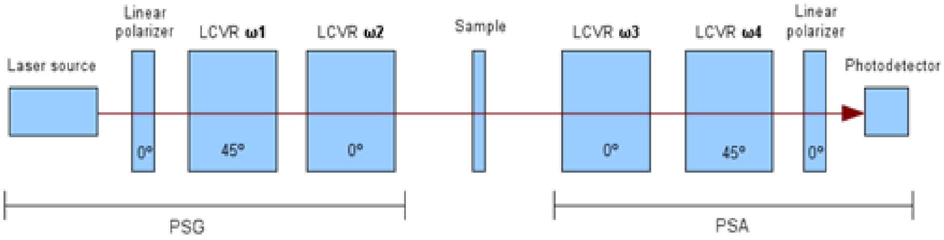

Fig. 5. The set-up for a Mueller matrix polarimeter. The angles associated with each component refer to the relative angle of the optical axis of that component. ω1, ω2, ω3 and ω4 are the frequencies of the variations of the retardances.

The PSG determines the polarization state of the incident light whereas the PSA measures the change in this state after interaction with the sample. In a similar way as the previous case, we can found all the components of the Mueller matrix, M, by fitting the detected signal to a linear combination. Details of this measurement method are described in a previous paper [6]. The 4 × 4 identity matrix is the Mueller matrix of the air. An example of experimental values obtained for this Mueller matrix is:

$$M_{Air} = \begin{pmatrix} 1 & -0.054 & 0.052 & 0.021 \\ -0.029 & 0.986 & -0.031 & 0.083 \\ -0.014 & -0.037 & 0.955 & -0.046 \\ -0.039 & -0.001 & -0.051 & 0.897 \end{pmatrix}. \quad (4)$$

The Mueller elements are all normalized by the first entry, M11. In the example shown in Eq. (4), the Mueller matrix was obtained with an accuracy error estimated at 1–10%, depending on the Mueller-matrix element. The measurement error of each matrix element is ±0.005. This instrument was tested on samples with known Mueller matrices such as polarizers, quarter-wave retarders, and half-wave retarders; in transmission mode, always obtaining good results.

Experimental results for a rotating linear polarizer are shown in Figure 5; measurements were made in steps of 10 degrees, from 0 to 180 degrees. It can be seen that the behavior of the results is, in general, as expected. Measurements and calculations were performed in LabVIEW®. The measurement time for each complete Mueller matrix was 1.8 seconds.

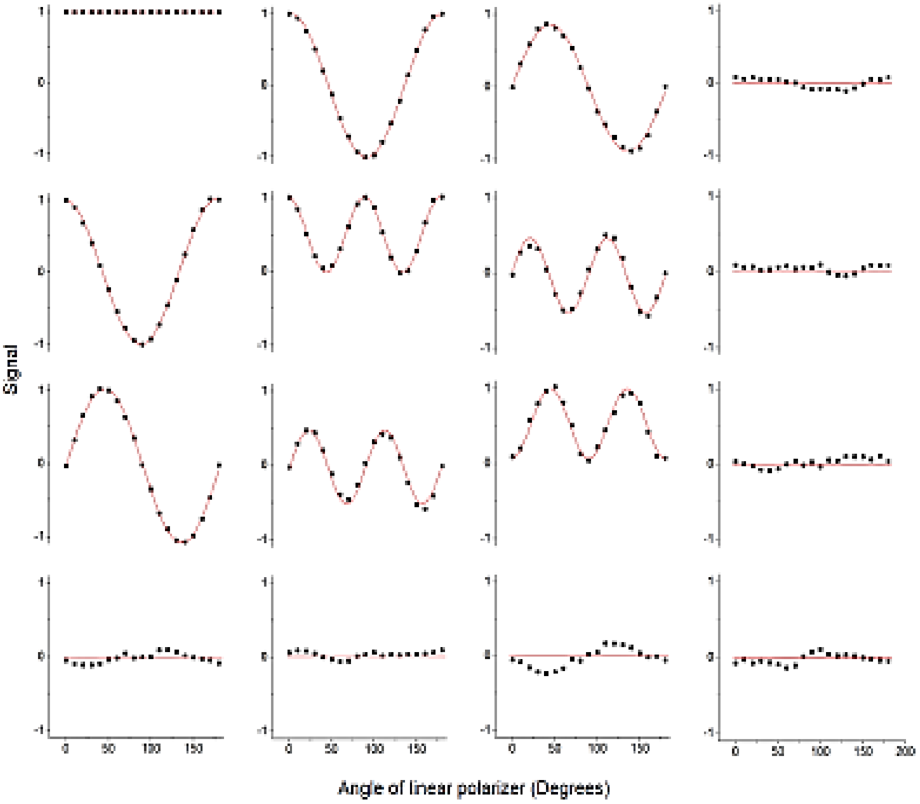

Fig. 6. Sixteen Mueller-matrix elements (classified as they appear in the matrix) of a Glan–Thompson prism polarizer drawn as a function of its optical angle (in degrees), obtained using a continually varying voltage method of measurement. The dots are the experimental results including device and sample imperfections; the solid curves are the fitted theoretical curves of an ideal polarizer. The Mueller elements are all normalized by the first entry, M11.

Acknowledgments. This work was supported by CONACyT of México through project No. 79814, and DGAPA, UNAM, through projects PAPIIT Nos. IN-115209 and IT-100114. J.M. López-Téllez acknowledges a postgraduate grant from CONACyT, and the support from Coordinación del Posgrado en Ingeniería, UNAM.

References

1. Goldstein, D.: Polarized Light. 2nd ed, Marcel Dekker, Inc. (2003)
2. Azzam, R. M. A.: Photopolarimetric measurement of the Mueller matrix by Fourier analysis of a single detected signal. Opt. Lett., 2, pp. 148–150 (1978)
3. Terrier, P., Charbois, J. M., Devlaminck, V.: Fast-axis orientation dependence on driving voltage for a Stokes polarimeter based on concrete liquid-crystal variable retarders. Appl. Opt., 49(22), pp. 4278–4283 (2010)

4. López-Téllez, J. M., Bruce, N. C.: Stokes polarimetry using analysis of the nonlinear voltage-retardance relationship for liquid-crystal variable retarders. Rev. Sci. Instrum., 85(3), 033104 (2014)
5. López-Téllez, J. M., Neil, C., Delgado-Aguillón, B. J., Garduño-Mejía, J., Avendaño-Alejo, M.: Experimental method to characterize the retardance function of optical variable retarders. Am. J. Phys., In press (2014)
6. López-Téllez, J. M., Bruce, N. C.: Mueller-matrix polarimeter using analysis of the nonlinear voltage-retardance relationship for liquid-crystal variable retarders. Appl. Opt., 53(24), pp. 5359-5366 (2014)

ISSN 1870-4069

Nonlinear Transmission of a NOLM with a Variable Wave Retarder inside the Loop

Yazmin E. Bracamontes-Rodríguez[1], Ivan Armas Rivera[1], Georgina Beltrán-Pérez[1],
J.Castillo-Mixcoátl[1], S.Muñoz-Aguirre[1], Olivier Pottiez[2], Baldemar Ibarra-Escamilla[3],
Evgeny A. Kuzin[3]

[1] BUAP, Facultad de Ciencias Físico Matemáticas, Puebla, Mexico

[2] Centro de Investigaciones en Óptica, León, Gto, Mexico

[3] Instituto Nacional de Astrofísica, Óptica y Electrónica, Puebla, Mexico

yazmin_1985@yahoo.com.mx

Abstract. We research experimentally the configuration of a nonlinear optical loop mirror, with an imbalanced coupler, highly twisted low birefringence fiber and a variable wave retarder (VWR) inserted into the loop. The use of the variable wave retarder allows the easy adjustment of the nonlinear dependence of the NOLM transmission. The mechanism of VWR consists of applying an adjustable pressure on the optical fiber inside the loop to have different values of VWR through simple way. The nonlinear transmission of NOLM for different values of Δ and different amplitude of the input pulse were presented. The experimental results showed that VWR is a device that allows a simple adjustment of the nonlinear characteristic of the NOLM.

Keywords: nonlinear transmission, NOLM, variable wave retarder.

1 Introduction

Nonlinear Sagnac interferometer in optical fiber or nonlinear optical loop mirror (NOLM) device which was first introduced by N.J. Doran and David Wood (Doran N.J. y Wood D., 1998), is commonly used in nowadays in many applications, such as, optical switching (Moores J.D., et al., 1991; Cao W. et al., 2005; Agarwal, et al., 2005; Pottiez O. et al., 2004),wavelength the multiplexing (Sotobayashi H., et al., 2002), all-optical active mode locking (Tang W.W., et al., 2001), passive mode locking (Duling I.N., et al., 1991), pedestal suppression on pulses and pulse compression (Pelusi M.D., et al., 1999), and regeneration of ultrafast data streams (Sakamoto T. and Kikuchi K., 2005).

The setup of this device consist in a coupler whose output ports are fused by highly twisted fiber, which offer a versatile way to get nonlinear transmission or characteristic switching through Kerr effect, when a phase difference is present between two counter-propagating beams which interfere in the coupler.

Most of the designs of these devices advantage the Self-Phase Modulation (SPM) effect, which cause a nonlinear phase difference, that is accumulated only, if appear asymmetry in the power between two counter-propagating beams in the loop, generally imposed by coupling ratio (α), which offers a very poor possibility to adjust the contrast or critical power and cannot have simultaneously high contrast and low critical power.

Other works report the use of a symmetrical coupler and a quarter-wave plate (QWP) retarder inside the loop near the coupler output port to generate a polarization asymmetry to obtain a high contrast and low critical power (Ibarra-Escamilla B., et al., 2004; Ibarra-Escamilla B., et al., 2005; Pottiez O., et al., 2005). The evolution of the nonlinear polarization (including Self-Phase Modulation (SPM) and Cross-phase modulation (XPM)), of the optical beam along the fiber it can be easily described using the coupling equations which was development by Kuzin (Kuzin E. A., et al., 2001). Many authors that work with optical fiber Sagnac interferometer obtain the characteristic transmission adapted to their particular applications, but usually give very few information about accurate manipulations required to achieve this result, therefore we decided to investigate an experimental study of the effect of a variable wave retarder (VWR) inside of the loop to obtain the easy adjustment of the nonlinear dependence of the NOLM transmission. For this case, the mechanism of VWR consists of applying an adjustable pressure on the optical fiber inside the loop to have different values of VWR through simple way. This mechanism is placed asymmetrically inside the loop with an imbalanced coupler (α=0.52 and α=0.48). To close the loop a low birefringence optical fiber, highly twisted was used. A mode-locked fiber ring laser emitting pulses of 0.7 ps duration with 1545 nm central wavelength was implemented as a source of signal.

The present work discusses the possibility of adjusting the nonlinear dependence of the NOLM by means of the polarization imbalance provoked by a VWR in the loop, which has not been reported up to date.

2 Experimental Setup

The experimental setup used to characterization of the NOLM is shown in fig. 1. We use a mode-locked fiber ring laser emitting pulses of 0.7 ps duration with 1545 nm central wavelength as a source of signal. The pulses were amplified by an EDFA with maximum amplification up to 20 times. The pulses from the amplifier output pass through a polarization controller PC, a polarizer, and a QWP. Rotation of the QWP allows generating a stable polarization state with desired ellipticity, in this particular case a circular polarization was used. After this, the pulses were splitted by a 90/10 coupler where the 10 % is used to monitor the polarization and power of pulses in the input of NOLM.

The NOLM is formed by a slightly imbalanced 52/48 coupler, whose output ports were fusion-spliced with a 200-m loop of low-birefringence, highly twisted (6 turns/m) Corning SMF-28 standard fiber. A VWR retarder was created by applying an adjustable pressure on the optical fiber. Pressure produces a linear birefringence in this portion of the fiber with the slow axis in the direction that pressure is applied.

The VWR can be rotated to change the axes orientation. The retardation between the slow and fast axes can be varied between 0 and 2π through pressure adjustment. The VWR was inserted near one of the output ports of the coupler. We performed measurement with the VWR inserted near both, the 0.52 port and the 0.48 port to compare the results. And finally the output pulses were detected by ultrafast photodetector with 8 GHz and monitored by the oscilloscope with 2 GHz of bandwidth. The transmission was calculated as a ratio between amplitudes of the output and input pulses.

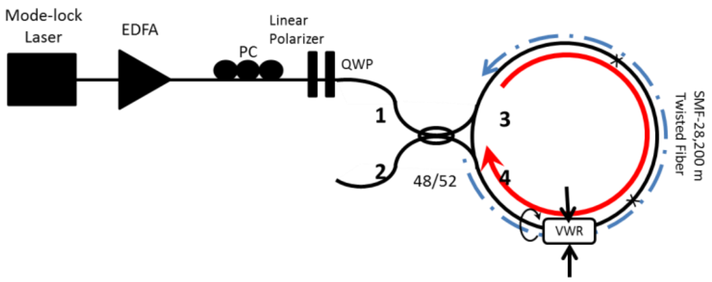

Fig. 1. Experimental setup.

3 Results and Discussion

Fig. 2, shows the result of measurements of NOLM transmission as a function of the amplitude of the input pulse for input ports, 0.52 and 0.48, respectively. We can see the NOLM nonlinear transmission at Δ=0 due to the power imbalance of the coupler. When the VWR is inserted to the 0.52 port the effect of the power imbalance adds to the effect of the polarization imbalance therefore the transmission grows with the increment of the retardation of the VWR. In contrast to the results shown in figure 2 (b), the polarization imbalance and power imbalance made opposite nonlinear phase shifts.

As a result at small retardations the transmission is less than for retardation equal to 0. The transmission is 0 at any power at the retardation equal to 0.375*π/4. For retardation higher than 0.375 the transmission starts to grow with the increment of the retardation. In the same figure we can note that occur a small increment of the low power transmission, less than 5 %. We attribute this to small misalignment of the VWR angle when the retardation is changed.

The complexity of the measurements of the transmission dependence on the pulse power arises from the fact that increasing of pulse power results in the same time the change of the other characteristics of the pulse such as pulse duration and chirp. These parameters also affect the NOLM transmission. To see clearly the effect of the VWR we measured the transmission against the retardation at the constant pulse power. Fig. 3, shows the nonlinear transmission of the NOLM as a function of the VWR for different input pulse amplitudes when the VWP is inserted to the 0.52 port.

When the pulse amplitude has a value of 1.43, the dependence data at pulse power of 70 W, except that the minimum value occurs when Δ=0.8. This shift may be due to not very exact calibration of the VWR or because the input polarization was not exactly circular.

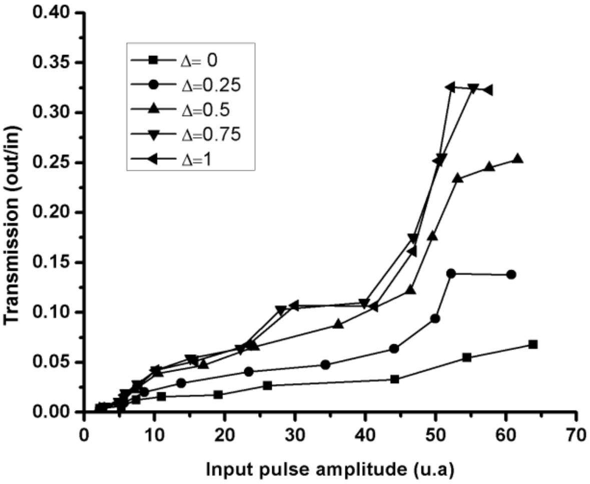

a)

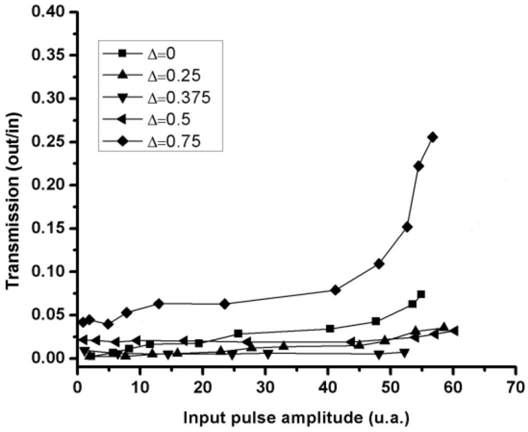

b)

Fig. 2. Transmission of NOLM versus input pulse amplitude, (a) input port of 52% and (b) input port of 48%.

Fig. 4 Show that the transmission reaches to a maximum when Δ=1.2. Another important feature is that when Δ<0.5 there is a minimum of transmission since it is considered that the nonlinear effects are subtracted because the difference powers between the counter propagating beams in the NOLM.

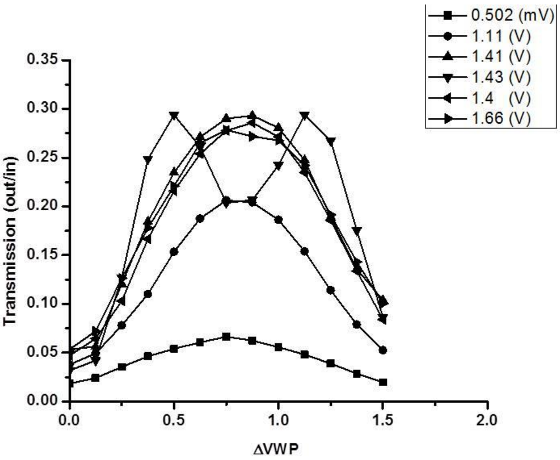

Fig. 3. Transmission of NOLM versus different values of ΔVWP, experimental results input port of α=0.52.

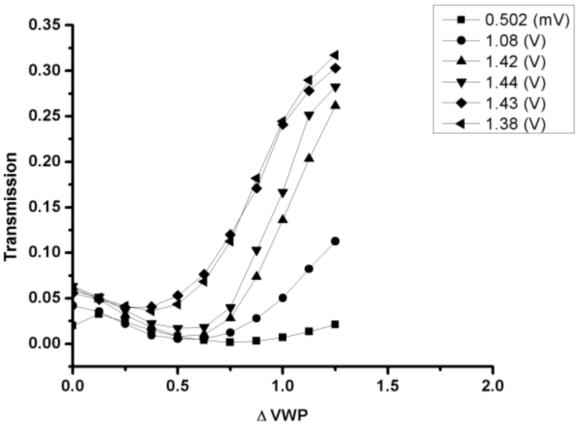

Fig. 4. Transmission of NOLM versus different values of □VWP, experimental results of input port of α=0.48.

4 Conclusions

In this work an experimental study of nonlinear transmission of NOLM for different values of Δ and different amplitude of the input pulse were presented. A simple and new device as a variable wave retarder was used inside of the loop. That the experimental results showed that VWR is a device that allows a simple adjustment of the nonlinear characteristic of the NOLM.

References

1. Agarwal, A., Wang, L., Su, Y., Kumar, P.: All optical loadable and erasable storage buffer based on parametric nonlinearity in fiber. J. Lightwave Technol., 23, pp. 2229–2238 (2005)
2. Cao, W., Wai, P. K. A.: Comparison of fiber-based Sagnac interferometers for self for-Switching of optical pulses. Opt. Commun., 245, pp. 177–186 (2005)
3. Doran, N. J., Wood, D.: Nonlinear optical loop mirror. Opt. Lett., 13, pp. 56–58 (1998)
4. Duling, I. N.: All- fiber ring soliton laser mode locked with a nonlinear mirror. Opt. Lett., 16, pp. 539–541 (1991)
5. Ibarra-Escamilla, B., Kuzin, E., Pottiez, O., Haus, J., Gutierrez-Zainos, F., Grajales-Coutiño, R., Zaca-Moran, P.: Fiber optical loop mirror with a symetrical coupler and quarter-wave retarder plate in the loop. Opt. Commun, 242, pp. 191–197 (2004)
6. Ibarra-Escamilla, B., Kuzin, E., Zaca-Moran, P., Grajales-Coutiño, R., Mendez-Martinez, F., Pottiez, O., Roja-Laguna, R., Haus, J. W.: Experimental investigation of the nonlinear optical loop mirror with twisted fiber and birefrigence bias. Optics Express., Vol 13, 26, pp. 10760–10767 (2005)
7. Kuzin, E. A., Korneev, N., Haus, J. W., Ibarra-Escamilla, B.: Theory of nonlinear loop mirrors with twisted low-birefringence fiber. J. Opt. Soc. Am. B, 18, pp. 919–925 (2001)
8. Moores, J. D., Bergman, K., Haus, H. A., Ippen, E. P.: Optical switching using fiber ring reflectors. J. Opt. Soc. Am. B, 8, pp. 594–601(1991)
9. Pelusi, M. D., Matsui, Y., Suzuki, A.: Pedestal suppression from compressed femtosecond pulses using a nonlinear fiber loop mirror. IEEE J. Quantum Electron, 35, pp. 867–874 (1999)
10. Pottiez, O., Kuzin, E. A., Ibarra-Escamilla, B., Camas-Anzueto, J. L., Gutierrez-Zainos, F.: Experimental demostration of NOLM Switching bassed on nonlinear polarization rotation. Electron. Lett., 40, pp. 892–894 (2004)
11. Pottiez, O., Kuzin, E. A., Ibarra, B., Mendez-Martinez, F.: Theorical investigation of the NOLM with highly twisted fibre and a λ/4 birrefringence bias. Opt. Commun., 254, pp. 152–167 (2005)
12. Sakamoto, T., Kikuchi, K.: 160 GHz operation of nonlinear optical loop-mirror with an optical bias controller. IEEE Photonics Technol. Lett., pp. 543–545 (2005)
13. Sotobayashi, H., Sawaguchi, C., Koyamada, Y., Chujo, W.: Ultrafast walk-off-free nolineal optical loop mirror by a simplified configuration for 320 Gbit/s time-division multiplexing signal demultiplexing. Opt. Lett., 27, pp. 1555–1557 (2002)
14. Tang, W. W., Shu, C., Lee, K. L.: Rational harmonic mode locking of an optically triggered fiber laser incorporating a nonlinear optical loop modulator. IEEE Photon Technol. Lett., 13, pp. 16–18 (2001)

ISSN 1870-4069

Understanding Non-Invasive Glucose Level Sensing Using Raman Scattering to Propose Novel Schemes

Aldo Di Costanzo Mata, Luis Cortez González, Daniel Ceballos Herrera,
Arturo Castillo Guzmán, Romeo Selvas Aguilar

Universidad Autónoma de Nuevo León (UANL), Facultad de Ciencias Físico Matemáticas,
Nuevo León, Mexico

Aldo.DiCostanzo@gmail.com

Abstract. For Healthcare professionals is important to measure the glucose level in diabetes patients in order to prevent any systematical failure. For this manner it is important to understand the social and economic advantages of developing non-invasive sensing methods. The main objective is to use the Raman Scattering to develop schemes that predicts the value of glucose level on patients using the Source and Stokes wavelengths energies signals.

Keywords: non-invasive glucose level sensing, Raman scattering.

1 Introduction

Public healthcare is a medullar objective in every nation and society. An impact on public healthcare generates low statistics on Labor Force and in consequence it generates low economic rates. Increasing constantly, diabetes has become a very common condition in world's population, over 347 million people globally present diabetes [9]. 80% of diabetes deaths occur on the low and middle income countries [10].

In 2010, global healthcare expense for prevention and treatment of diabetes was valued around $376 Billion US Dollars. By 2030 the expected expense would be $490 Billion US Dollars [4]. In regards of the Biosensors market, by 2004 the glucose biosensors represented the 85% of the world's market valued in $5 Billion US Dollars [6]. This factors open opportunities to develop devices that decreases the diabetes healthcare cost increasing biosensors market for good.

Non-invasive diagnostic methods provide advantages that improve the healthcare procedures and minimize the need of interventions. In the imaging area it's possible to explore patient internal structures to develop prosthesis that perfect fit, plan surgeries or detect the exact position of a tumor. In our case, sensing blood glucose level with optical devices opens the possibility of constant sensing, maintains biological system intact and prevents tissue exposure, frequent nerve damage, pain and recurrent purchase of disposables [2].

pp. 49–53; rec. 2017-05-15; acc. 2017-11-17

2 Fundamentals

2.1 Diabetes

Diabetes mellitus is defined as the group of metabolic diseases that present high levels of glucose in the blood. It is caused by a lack of production or high resistance from the tissues to insulin. Glucose levels are managed by the insulin-glucose feedback system via pancreatic hormones insulin and glucagon. During the interprandial period (time between meals) almost all glucose is used by the brain and the insulin-glucose feedback system prevents the Pancreas to produce insulin [3].

Glucose is mainly presented on its α-D-glucose form and doesn't require any protein or other component to travel trough the bloodstream [8]. Regular glucose levels oscillates around 75-95 mg⁄dl during a normal day. A high glucose level causes cell dehydration. A prolonged exposure to high glucose concentrations causes tissue damage in peripheral nerves and vascular cells which promotes heart attacks, stroke, renal failure, blindness, etc [3].

2.2 Raman Scattering

Used to study and identify a sample (like glucose) in the electromagnetic spectrum, illustrated on figure 1, the Raman Scattering is a non-linear inelastic process where a molecular medium is pumped with a ωpump frequency and then another lower frequency emerges; this new frequency is known as Stokes or ωStokes. The Stokes frequency is presented when the molecule absorbs the ωpump, that increases the energy level of a particle in ground state to a virtual state, then the particle decreases to a vibrational state emitting the ωStokes, the rest of the energy is dissipated by the molecule vibration [1]. If the particle decreases to the ground state, the emitted frequency is equal to the ωpump, this elastic effect it's known as Rayleigh scattering. If a particle is in vibrational state, then increases to a virtual state to decrease to a ground state, the new scattered frequency is known as Anti-Stokes or8 ωAnti-Stokes [5].

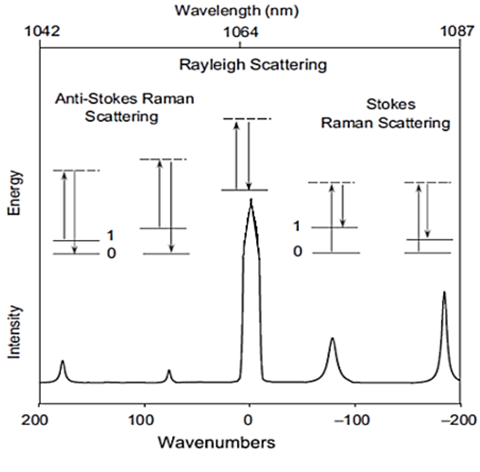

Fig. 1. Raman Scattering and Spectrum example.

3 Experimental Principles & Proposal

Our proposal is based on pulsioximeter principle, observed on Figure 2, as a preliminary model to obtain the desired interface. Finger vascular bed is pumped with two wavelengths (660nm and 940 nm) and the logarithmic relationship between them delivers measurements that predict the oxygen saturation level on blood [2]. Our approach lies on the capability to implement photodetectors for the Rayleigh and Stokes wavelengths for the α-D-glucose and to use the proper laser wavelength and intensity to provoke desired stokes emission. Collected and filtered data will be processed to implement a statistical method to predict the Blood Glucose Level.

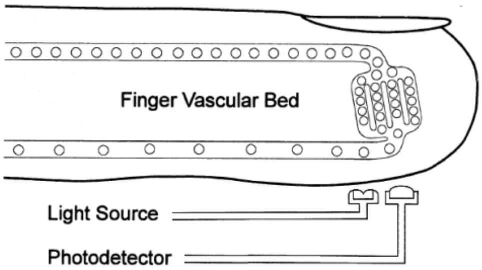

Fig. 2. Pulsioximeter Scheme.

A promising recent Raman spectroscopy applied on skin, spectrum shown on Figure 3, used a 785nm continuous laser radiation at 400mW and a Shamrock SR-163 spectrograph coupled to a -90°C cooled (for a better curve response) iDus DU-401 Detector. The results presented a 0.83 accuracy using a R2 coefficient of determination (Raman vs. Capillary Glucose), showing a mean relative deviation of 13.9±11.4% [7].

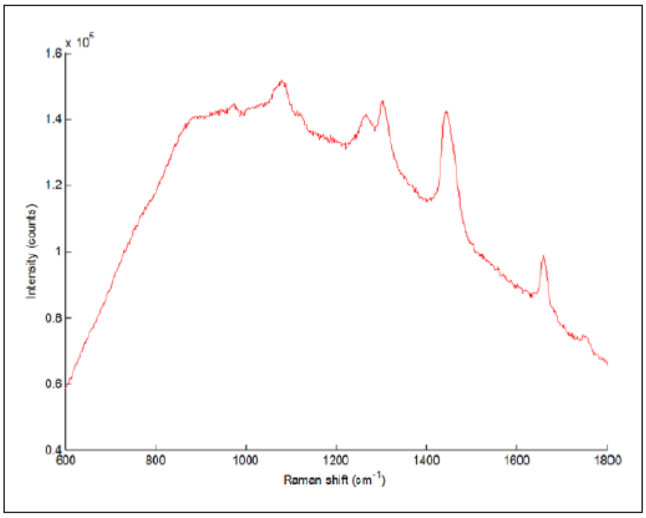

Fig. 3. Raman Spectrum of Human Skin Tissue.

The main proposal, on Figure 4, is a circuit that consists on a Pump Laser and two detectors, one to detect the Pump wavelength or Rayleigh scattered light and the other to detect the Stoke's wavelength.

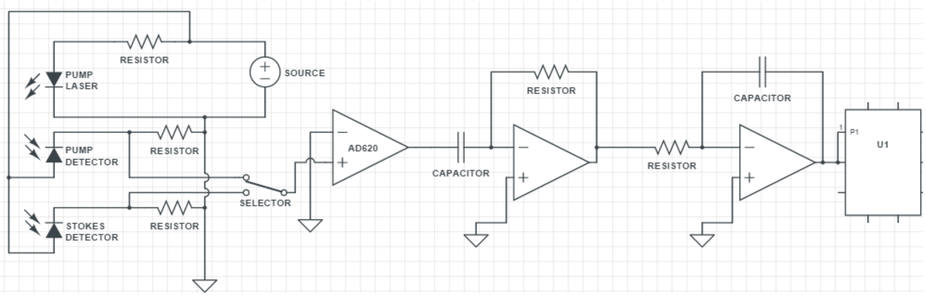

Fig. 4. Proposed circuit model.

An expected weak signal from each detector will be amplified by an instrumentation amplifier (Op. Amp. AD620). Then a Band-pass filter will be needed to remove the DC components and the non-desired electrical noise (50/60 Hz). After this step our signals can be converted and analyzed by a computer or microcontroller.

4 Conclusions

The proposal is based on the ideal scenario that we know the specific wavelengths (Pump, Rayleigh & Stokes) energies (For α-D-glucose) needed to detect, in order to apply the specific optical and electronical instrumentation to measure the signals without analyzing a considerable portion of the spectrum. Obvious investigation and experimentation processes are pending to develop. A device with these characteristics will occupy little space so it could be portable, cheaper if compared with a spectrum analyzer and easy to repair because the components can be replaced if the physical design allows it.

On regards Diabetes, a device with these characteristics would provide a diverse number of applications for healthcare treatment for example: Distance continuous monitoring, an alert system for patients and healthcare professionals, Smartphone applications for a better response in case of glucemic incident (GPS position + alert system), etc. This may lead to a lower diabetes healthcare cost and an increase on the economic activities related to biosensors, development, network applications, software, etc.

Acknowledgments. Authors want to thank to all collaborators and persons who supported this project with their knowledge and time. Special thanks to CONACYT via scholarship CVU/Becario: 627802/332756.

References

1. Agrawal, G. P.: Nonlinear fiber optics. Academic press (2007)

2. Carvajal, R. A. E.: Propuesta de Tesis para la Maestría en Ciencias de la Ingeniería Electrónica con Especialidad en Electrónica. Biosensores, Monterrey Institute of Technology and Higher Education (2008)
3. Hall, J. E., Guyton, A. C.: Textbook of medical physiology. Elsevier Spain (2011)
4. International Diabetes Federation.: The Economic Impacts of Diabetes. Available at: http://www.idf.org/diabetesatlas/economic-impacts-diabetes (2009)
5. Larkin, P.: Infrared and Raman spectroscopy; principles and spectral interpretation. Elsevier (2011)
6. Newman, J. D., Turner, A. P.: Home blood glucose biosensors: a commercial perspective. Biosensors and Bioelectronics, DOI: 10.1016/j.bios.2004.11.012, 20(12), pp. 2435–2453 (2005)
7. Scholtes-Timmerman, M. J., Bijlsma, S., Fokkert, M. J., Slingerland, R., van Veen, S. J.: Raman Spectroscopy as a Promising Tool for Noninvasive Point-of-Care Glucose Monitoring. Journal of diabetes science and technology, DOI: 10.1177/1932296814543104 (2014)
8. Voet, D., Voet, J. G., Pratt, C. W.: Fundamentals of biochemistry: life at the molecular level. Editorial Médica Panamericana (2006)
9. World Health Organization.: Diabetes. Media Centre. Fact sheet N° 312. Available at: http://www.who.int/mediacentre/factsheets/fs312/en/ (2010)
10. World Health Organization.: 10 Facts about Diabetes. Diabetes. Available at: http://www.who.int/features/factfiles/diabetes/facts/en/index7.html

ISSN 1870-4069

Performance Study of Quaternion and Matrix Based Orientation for Camera Calibration

Rigoberto Juarez-Salazar[1], Carlos Robledo-Sánchez[2], Fermín Guerrero-Sánchez[2],
J. Jacobo Oliveros-Oliveros[2], C. Meneses-Fabian[2]

[1] División de Ingeniería Informática, Instituto Tecnológico Superior de Zacapoaxtla,
Zacapoaxtla, Puebla Mexico

[2] Facultad de Ciencias Físico Matemáticas, Benemérita Universidad Autónoma de Puebla,
Puebla, Puebla, Mexico

{Rigoberto Juarez-Salazar, rjuarezsalazar}@gmail.com

Abstract. The feasibility of quaternion and rotation matrix approaches to describe orientation of a camera device is presented. The usefulness of both methods is tested emphasizing its implementation for calibration of extrinsic camera parameters. Preliminary simulation results are given.

Keywords: quaternion based orientation, matrix based orientation, camera calibration.

1 Introduction

Camera calibration is an important task in any vision-based measurement application such as photogrammetry and optical profilometry for three-dimensional (3D) reconstruction [4]. The camera calibration procedure consists on to find the parameters of the mapping from the 3D coordinates and its corresponding two-dimensional images [5]. The calibration parameters are usually classified into intrinsic and extrinsic ones [2]. Intrinsic parameters describe internal parameters of the camera (mainly focal length, imaging distortion, and distortion center) while extrinsic parameters give information about the spatial position (x_0, y_0, z_0) and the orientation (γ,θ,φ) of the camera with respect to a reference frame as shows Fig. 1.

3D matrix rotation are usually employed to describe the orientation of camera devices in most of the camera calibration methods [3]. However, unitary quaternions are very efficients to represent orientation of objects [1]. Therefore, a performance study of both quaternion- and matrix-based orientation approaches for camera calibration is addressed in this work.

In the following section, the mathematical background of both rotation matrices and unitary quaternions for rotation in three-dimensional spaces is given. Then, both approaches are evaluated by a computer simulation. The computational efficiency as well as the simplicity of implementation are emphasized. In the last section a conclusion is given.

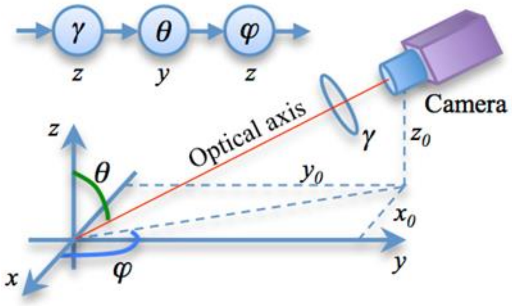

Fig. 1. Actual configuration and camera extrinsic parameters.

2 Mathematical Background

In the camera calibration context, the orientation (also known as angular position or attitude) consists on a set of parameters (axis and angles) which describe how a rigid body is placed in the space. In many applications, it is necessary to known or to control such parameters. Particularly, it is necessary to know or controlling the spatial and angular positions of one or more cameras for three-dimensional object reconstruction by optical methods.

For angular position, there are several mathematical tools to describe the involved parameters. For this, the most widely used are the rotation matrices and the unitary quaternions. These approaches are described below.

2.1 Rotation Matrices

For a given reference frame, the orientation of a rigid body can be described by setting a rotation sequence by appropriate rotation axes and the respective angles. When the rotation axes are matched with the coordinate ones, the description is known as Euler Angle-axis Sequence or simply as Euler Angles.

With this approach, it is possible to propose many angle-axis sequence and its usefulness is determined by the physical meaning or the application. In this study, we employ the following rotation sequence [see Fig. 1)]:

1. A rotation of an angle γ about the z-axis,
2. A rotation of an angle θ about the y-axis, and
3. A rotation of an angle φ about the z-axis.

Each of the above mentioned angle-axis operation is defined by the matrices:

$$R_1(\gamma) = \begin{bmatrix} \cos\gamma & -\sin\gamma & 0 \\ \sin\gamma & \cos\gamma & 0 \\ 0 & 0 & 1 \end{bmatrix}, \tag{1}$$

$$R_2(\theta) = \begin{bmatrix} \cos\theta & 0 & \sin\theta \\ 0 & 1 & 0 \\ -\sin\theta & 0 & \cos\theta \end{bmatrix}, \tag{2}$$

$$R_3(\varphi) = \begin{bmatrix} \cos\varphi & -\sin\varphi & 0 \\ \sin\varphi & \cos\varphi & 0 \\ 0 & 0 & 1 \end{bmatrix}. \tag{3}$$

Thus, we have the three-dimensional rotation matrix

$$R = R_3(\varphi)R_2(\theta)R_1(\gamma). \tag{4}$$

2.2 Unitary Quaternions

Another mathematical tool to describe orientation of a rigid body is the use of unitary quaternions. Quaternions are hyper-complex numbers of the form

$$q = q_0 + q_1 i + q_2 j + q_3 k = \begin{bmatrix} q_0 \\ \bar{q} \end{bmatrix}, \tag{5}$$

where $i,\ j,\ k$ are imaginary units, q_n $(n = 1,2,3,4)$ are real numbers, q_0 and $\bar{q} = [q_1 \quad q_2 \quad q_3]^T$ are the so-called scalar and complex parts of the quaternion, respectively. Crucial for quaternions is the product rule of its imaginary units:

$$i^2 = j^2 = k^2 = ijk = -1. \tag{6}$$

By using the above product rule, the product of two quaternions $p = [p_0 \quad \bar{p}^T]^T$ and $q = [q_0 \quad \bar{q}^T]^T$ is given by

$$pq = p_0 q_0 - \bar{p}\cdot\bar{q} + p_0\bar{q} + q_0\bar{p} + \bar{p}\times\bar{q}, \tag{7}$$

where the symbols $[\cdot]$ and $[\times]$ denote the usual vectorial inner and cross products, respectively.

For angle-axis rotation purposes in a three-dimensional space, it is convenient the notation:

$$q = \cos\frac{\theta}{2} + u\sin\frac{\theta}{2} = \begin{bmatrix} \cos\frac{\theta}{2} \\ u\sin\frac{\theta}{2} \end{bmatrix}, \tag{8}$$

where $u = [u_1 \quad u_2 \quad u_3]^T$ is an unitary vector which defines the rotation axis while θ is the rotation angle about u. By using the quaternion in Eq. (8), the rotation of a three-dimensional vector $\bar{v} = [v_1 \quad v_2 \quad v_3]^T$ is carried out by the quaternion product

$$w = qvq^*, \tag{9}$$

where $v = [0 \quad \bar{v}^T]^T$ is a pure quaternion (without scalar part) and $w = [0 \quad \bar{w}^T]^T$ is the resulting pure quaternion where its complex vectorial part $\bar{w}$ is the rotated version of $\bar{v}$.

To obtain the involved parameters of a rotation, instead of the quaternion product in Eq. (9), a linear form is desirable. For this regard, in the following subsection is presented an alternative matrix representation for the Eq. (9).

2.3 Matrix Description of Unitary Quaternion

From the unitary quaternion q in Eq. (8) (defining the angle and axis of the rotation), and the pure quaternion v (defining the three-dimensional point to be rotated), we have for the product qv:

$$qv = \begin{bmatrix} -u \cdot \bar{v} \sin\frac{\theta}{2} \\ \bar{v}\cos\frac{\theta}{2} + u \times \bar{v} \sin\frac{\theta}{2} \end{bmatrix}. \tag{10}$$

Now, the rotated vector $\bar{w}$ is computed as the complex part of the resulting quaternion:

$$w = qvq^* = \begin{bmatrix} -u \cdot \bar{v} \sin\frac{\theta}{2} \\ \bar{v}\cos\frac{\theta}{2} + u \times \bar{v} \sin\frac{\theta}{2} \end{bmatrix} \begin{bmatrix} \cos\frac{\theta}{2} \\ -u \sin\frac{\theta}{2} \end{bmatrix} = \begin{bmatrix} 0 \\ \bar{w} \end{bmatrix}, \tag{11}$$

where

$$\bar{w} = u(u \cdot \bar{v}) \sin^2\frac{\theta}{2} + \bar{v}\cos^2\frac{\theta}{2} + 2u \times \bar{v} \sin\frac{\theta}{2}\cos\frac{\theta}{2} + u \times (u \times \bar{v}) \sin^2\frac{\theta}{2}. \tag{12}$$

By using the “vector triple product” identity, the above equation is simplified to

$$\bar{w} = 2u(u \cdot \bar{v}) \sin^2\frac{\theta}{2} + \bar{v}\cos^2\frac{\theta}{2} + 2u \times \bar{v} \sin\frac{\theta}{2}\cos\frac{\theta}{2} - \bar{v} \sin^2\frac{\theta}{2}. \tag{13}$$

For convenience, the vector inner and cross products are denoted as

$$u \cdot \bar{v} = u^T \bar{v}, \tag{14}$$

$$u \times \bar{v} = u^{\times} \bar{v}, \tag{15}$$

where $u^{\times}$ is the skew-symmetric matrix

$$u^{\times} = \begin{bmatrix} 0 & -u_3 & u_2 \\ u_3 & 0 & -u_1 \\ -u_2 & u_1 & 0 \end{bmatrix}. \tag{16}$$

Thus, the equation (13) can be restated as

$$\bar{w} = Q\bar{v}, \tag{17}$$

with Q being the matrix

$$Q = \cos^2\frac{\theta}{2} I - \sin^2\frac{\theta}{2} H + 2\sin\frac{\theta}{2}\cos\frac{\theta}{2} u^{\times}, \tag{18}$$

where I is the identity matrix and H is the Householder matrix:

$$H = I - 2uu^T. \tag{19}$$

From the equation (17), we can see that the rotation defined by the quaternion product qvq^* is equivalent to the linear combination of the vector to be rotated $\bar{v}$, its Householder reflection, and the perpendicular vector between $\bar{v}$ and the rotation axis u.

In the following, the description of camera extrinsic parameters in an experimental configuration is given. Then, both rotation matrices and unitary quaternions to representation of the angular position are evaluated.

3 Experimental Configuration

The extrinsic parameters of a camera device provide a description about the physical setup as shown in Fig. 1. Particularly, by assuming a pinhole camera model, the spatial $(\bar{x}_0, \bar{y}_0, \bar{z}_0)$ and angular $(\bar{\gamma}, \bar{\theta}, \bar{\varphi})$ positions of the camera device, as well as the length f between the pinhole and camera sensor planes, are considered.

In this work, the spatial position is not considered but rather the angular one. Accordingly, the actual configuration shown in Fig. 1 is equivalent to the case where the coordinate system is located at the camera's pinhole as shown in Fig. 2(a).

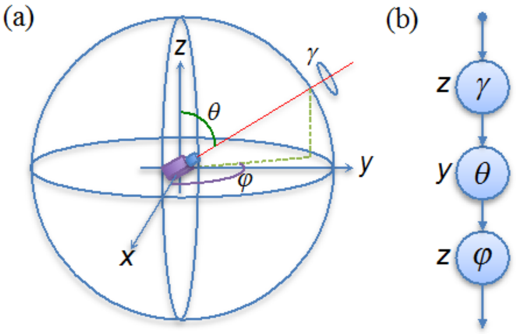

Fig. 2. (a) Angular position of a camera device. (b) Euler Angle sequence used for the matrix rotation approach.

4 Results

In order to test the performance of both matrix rotation and unitary quaternion approaches, a simple computer routine was designed. This consists on perform the rotation of the camera device from an initial position. Then, such movement is simulated by computer routines.

The simplicity of implementation and the computer resources required in executing time from both approaches are compared.

The rotation considered for this study is as follows:

1. The initial position of the camera is the vertical one [$\gamma = \theta = \varphi = 0$ in Fig. 2(a)] with the camera local frame aligned with the world frame.

2. A rotation is performed to align the camera's optical axis [red line in Fig. 2(a)] with the x axis. Simultaneously, a rotation about the optical axis is applied from zero to $\pi/2$ rad.

The described rotation was implemented in MATLAB software. The transformation obtained from both approaches is shown in Fig. 3.

The computing time required to execute the described rotation is slightly greater for quaternion approach than matrix one. Since the computer implementation was performed on MATLAB software, a matrix-based platform, the implementation of the matrix rotation approach was direct. On the other hand, for the quaternion approach, it was necessary to define the quaternion product given by Eq. (7) and other auxiliary functions. We believe that for this reason the computing time is different.

With respect to the mathematical analysis, for camera calibration it is necessary to obtain linear forms because of the parameter estimation procedure is simpler. In this context, rotation matrix is in an appropriate format. In contrast quaternion approach requires considering an alternative matrix representation.

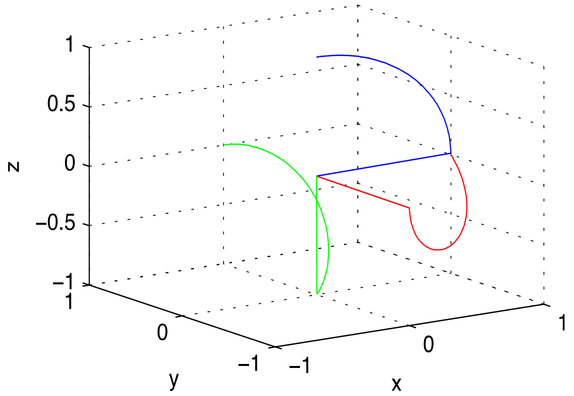

Fig. 3. Coordinates axis transformation by changing the angular position. Straigth lines denotes the unitary orthogonal vectors. Curves are the path followed by the vectors. Red, green and blue corresponds to x, y, and z, respectively.

5 Conclusion

The use of rotation matrices and unitary quaternions to describe angular position of a camera device was analyzed. For the particular case of to estimate the camera angular position, it is direct the use of rotation matrix approach while quaternion one requires additional algebraic manipulations to get an appropriate matrix format (instead of quaternion product).

Additional studies will be performed in future works to consider singularities such as gimbal lock and representation of angular position paths. This last could provide preliminary results about constrains in the solution space to make more stable the procedure of angular position with quaternions.

Acknowledgments. Authors thank the support from VIEP-BUAP, PROMEP-SEP, and CONACyT-México. R. Juarez-Salazar is grateful for the facilities provided from Instituto Tecnológico Superior de Zacapoaxtla.

References

1. Rahman, T., Krouglicof, N.: An efficient camera calibration technique offering robustness and accuracy over a wide range of lens distortion. Image Processing, IEEE Transactions on, 21(2), pp. 626–637 (2012)
2. Shah, S., Aggarwal, J.: Intrinsic parameter calibration procedure for a (high-distortion) fish-eye lens camera with distortion model and accuracy estimation. Pattern Recognition, 29(11), pp. 1775–1788 (1996)
3. Song, L. M., Wang, M. P., Lu, L., Huan, H. J.: High precision camera calibration in vision measurement. Optics & Laser Technology, 39(7), pp. 1413–1420 (2007)
4. Xu, J., Douet, J., Zhao, J., Song, L., Chen, K.: A simple calibration method for structured light-based 3d profile measurement. Optics & Laser Technology, 48(0), pp. 187–193 (2013)
5. Zhou, F., Cui, Y., Gao, H., Wang, Y.: Line-based camera calibration with lens distortion correction from a single image. Optics and Lasers in Engineering, 51(12), pp. 1332–1343 (2013)

ISSN 1870-4069

Comparison of an Optical-Digital Restoration Technique with Digital Methods for Microscopy Defocused Images

R. Ortiz-Sosa, L.R. Berriel-Valdos, J. F. Aguilar

Instituto Nacional de Astrofísica Óptica y Electrónica, Puebla, Mexico

rosalinda@inaoep.mx

Abstract. An optical-digital technique for restoring defocused images, and based on the quasi-point source concept, is introduced and compared with two conventional digital methods. The comparison is performed on the restoration of defocused microscopy images obtained with a conventional microscope but with three different numerical apertures. The effects of these techniques on the aberrated images are shown. We discuss and conclude about the advantages of our proposed technique.

Keywords: Optical-digital restoration technique, digital methods, microscopy defocused images.

1 Introduction

Every imaging optical system (*OS*) has a characteristic intensity point spread function (*ipsf)* associated, this function depends on the illumination wavelength (λ), the pupil function of *OS* and the numerical aperture (*NA*). In presence of aberrations of the *OS*, or with defocus, the ipsf detected out of focus will contain all this information, that is why the knowledge of the *ipsf* allows us to evaluate the quality of the *OS*, and its use is widely applied in image formation theory.

Since, the concept of point source is a mathematical abstraction, very useful for developing theoretical results, but the experimental realizations it is necessary to use a real point source. We propose to use an object with enough small dimensions that the *OS* cannot resolve, this kind of object is commonly known as a quasi-point source (*qps*) [1-3].

The detected image of a *qps* is then an estimated of the *ipsf*, and can also be used for generating of out-of-focus *ipsf's.* This corresponds with image of a *qps* when is located at different distances of the object plane.

Once these images have been detected it is possible to obtain the corresponding optical transfer functions (*OTF's*) associated with every defocused position. Then, a Wiener [4] filter can be constructed with those images. This is in order to realize a typical deconvolution technique, and that is why we call this an optical-digital technique.

In this work, a comparison of three different methods of restoration is presented. That which uses the *qps* and other two techniques using the digital (*OTF's*) [5-7].

pp. 63–70; rec. 2017-05-15; acc. 2017-11-19

2 Theoretical Background

In an aberration-free *OS*, the intensity distribution $(g(x,y))$ in the image plane is related with the intensity transmittance $(o(x,y))$ of the object and with the *ipsf* $(h(x,y))$ my means of the so called image formation equation in intensity

$$g(x,y) = h(x,y) \otimes o(x,y), \tag{1}$$

where (x,y) are the spatial rectangular coordinates and $\otimes$ indicates the convolution operation.

In the Fourier domain the equation takes the form

$$G(u,v) = H(u,v)O(u,v), \tag{2}$$

where G is image spectrum, O represents the spectrum of the transmittance of the object, and H is the OTF; (u,v) are the coordinates in the frequency domain.

When the image of a defocused object is detected, an aberration is introduced this known as defocus and is denoted by the term $\omega_{2,0}$ of the aberrations polynomial [8]. This aberration can be represented in the pupil function of the *OS* as

$$P_d(\rho) = \begin{cases} exp\left[ik\omega_{2,0}(\rho^2)\right] & if\ \rho \leq R, \\ 0 & if\ \rho > R, \end{cases} \tag{3}$$

where $k = 2\pi/\lambda$, $\rho = \sqrt{u^2 + v^2}$ and R is the radius of the pupil. The relation of $\omega_{2,0}$ with the displacement along the z axis of the object from the object plane $(\Delta z = 0)$ is of the form [9]:

$$\omega_{2,0} = \frac{1}{2} NA^2 \Delta z, \tag{4}$$

being *NA* the numerical aperture of the *OS*.

The *ipsf* for an object located out-of-focus which is denoted by h_d, is the square modulus of the inverse Fourier transform $(\Im^{-1})$ of the aberrated pupil function [10]:

$$h_d(x,y) = |\Im^{-1}\{P_d(u,v)\}|^2. \tag{5}$$

Then, equation (1) containing the effects of defocus and including the noise (n), which is introduced in the detection process, is expressed in the form

$$g_d(x,y) = h_d(x,y) \otimes o(x,y) + n(x,y) \tag{6}$$

This noise can be reduced by mean of an average over a sequence of images captured for the same defocus position Δz. The image formation equation in terms of this average image is

$$\bar{g}_d(x,y) \approx h_d(x,y) \otimes o(x,y) \tag{7}$$

and its spectrum is rewritten as

$$\bar{G}_d(u,v) \approx H_d(u,v)O(u,v). \tag{8}$$

In the other hand, the average image $(\bar{q}_d)$ of a *qps* is expressed in the form

$$\bar{q}_d(x,y) = h_d(x,y) \otimes circ\left(\frac{\sqrt{x^2+y^2}}{R}\right). \tag{9}$$

Since R is of very small dimensions, this means that the circ function can be approximated with a Delta function $circ\left(\sqrt{x^2+y^2}/R\right) \approx \delta(x,y),$ i.e the image of the a *qps* is approximated to the *ipsf*$_d$:

$$\bar{q}_d(x,y) \approx h_d(x,y) \tag{10}$$

and, in the Fourier domain equation (10) is expressed as

$$\bar{Q}_d(u,v) \approx H_d(u,v). \tag{11}$$

When the Wiener filter is used, the mean square error in the comparison between the focused image and the restored one is minimum. For this reason we have decided to use this filter for obtaining the spectrum of the restored image [5, 7]:

$$\hat{G}(u,v) = \frac{\bar{G}_d(u,v)H_d^*(u,v)}{|H_d(u,v)|^2 + S_n(u,v)/S_f(u,v)}, \tag{12}$$

where S_n corresponds to the power spectrum of the noise and S_f is the power spectrum of the focused image; symbol $*$ indicates conjugated complex.

Usually, in image restoration, when the values of the quotient in denominator of equation (12) this value is adjusted in an heuristically way for obtaining a good quality restoration we denote this factor with an ε, and selected the value of $\varepsilon = 3\times10^{-3}$.

Replacing equation (11) in equation (12) for the Wiener filter we have:

$$\hat{G}(u,v) = \frac{\bar{G}_d(u,v)\bar{Q}_d^*(u,v)}{|\bar{Q}_d(u,v)|^2 + \varepsilon} \tag{13}$$

and, finally, the inverse Fourier transform of equation (13) is an estimated of the image of the focused object.

3 Digital Methods

In the method proposed here, approximated of the defocused *ipsf's* of the *OS* are obtained. However, other authors have used *ipsf's* numerically simulated [5, 6] and to obtain them, the equation (3) is used, where the defocus term $\omega_{2,0}$ of the aberration polynomial is introduced. The defocus amount is calculated according with the equation (4), from the *a priori* knowledge of the distance from the object plane $\Delta z = 0$ at the moment in which the image is captured.

Another method with our technique is compared is the so called Blind Deconvolution Algorithm. This algorithm is used when the amount of defocus in the captured image is unknown; in this case the *ipsf* is estimated by means of an iterative process. This algorithm uses the standard of Maximum Likelihood [7].

4 Experiment

The OS is a bright field Olympus microscope model BX51, used with three objectives, 4X(0.1), 10x(0.3) y 20x(0.5). The image sequences used in the experiment were captured with a monochromatic *CCD* with a dynamic range of 0-255. The *CCD* has a 2448H X 2050V pixels, and a pixel pitch of 3.45µm. This Sony model XCL-5000. For digitizing the detected images a frame-grabber PCI-142924 from National Instruments.

The images introduced in our computing code were a segment of the originally captured of 512X512 pixels.

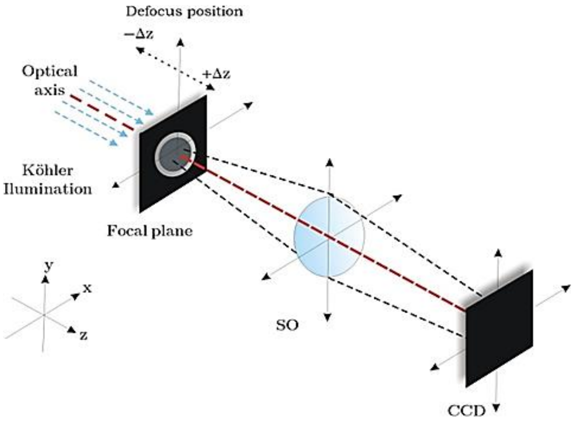

Fig. 1. Schematic diagram or the optical system.

For reducing the noise and other unwanted effects generated during the detection process, a series of images were averaged for each defocused position.

Considering that we wanted to keep a minimum capturing time, and after several proofs for determining the minimum variance in which the noise is reduced, a number of 20 images was selected for each defocus position.

For the generation of the $\bar{q}_d$ a pinhole of $1 \pm 0.5\mu\text{m}$ was used. This was previously verified that fulfills the requirements to be considered as a *qps* for the *OS* used in this work.

As the object we used a typical resolution test target. A region of the object containing high frequencies was analyzed.

5 Results

We show the results obtained with our optical-digital technique, and also those obtained with the other two digital methods.

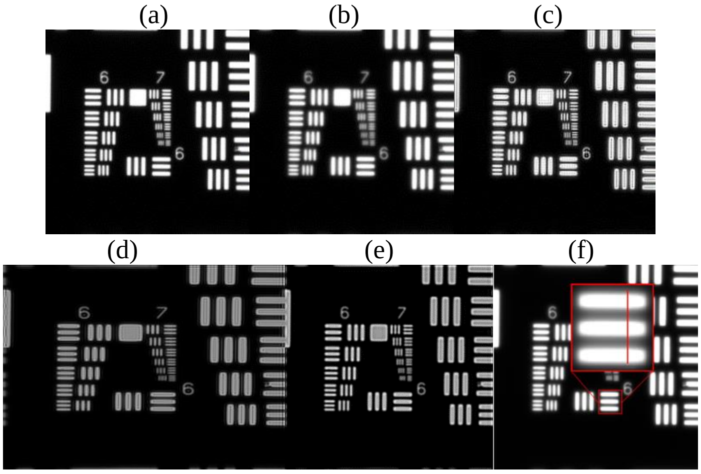

Fig. 2. a) in-focus image of the resolution test target detected with a microscopy objective 4X(0.1); b) defocused image of the object which amount of defocus is $\omega_{2,0} = 0.65$; c) restoration of the defocused using a simulated *ipsf*; d) restoration with the Blind deconvolution algorithm, with 100 iterations; e) restoration with our proposed optical-digital technique; f) this image is showing the transverse section that is used for the profiles plotted in the figure 3.

The results are presented in three groups, one for each objective lens used in the experiment. The first group is shown in Figure 2, it corresponds to the objective 4X(0.1) this includes the restoration obtained with our proposed method and also the restorations obtained with the other two methods. In the same way, the group in Figure 4 is for the images obtained with the objective 10X(0.3) and the group in Figure 6 is for the objective 20X(0.5).

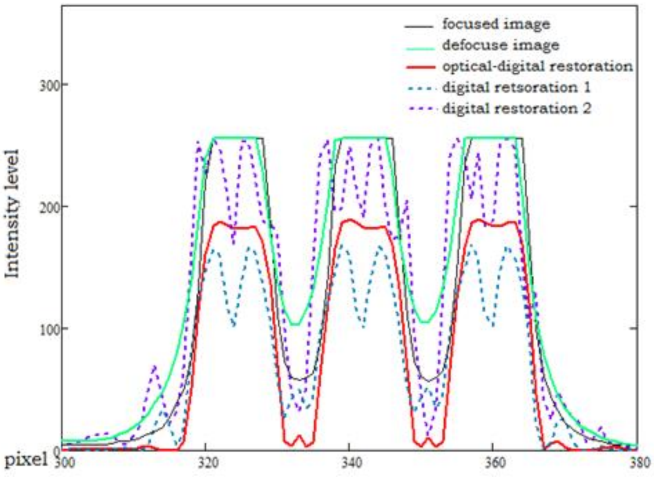

Fig. 3. Intensity profiles in the indicated region in Figure 2(f). Optical-digital technique (continuous red line), using a simulated *ipsf* (dotted blue line), the Blind deconvolution algorithm (dotted purple line), also both the profile of the in-focus image (continuous black line), and out-of-focus image (continuous green line).

Also we present profiles of the restored images of a selected region in the image (marked in red), they appear in Figure 3 for the objective 4X(4.1); in Figure 5 are the profiles for the objective 10X(0.3), and in Figure 7 the profiles for the objective 20X(0.5) are shown.

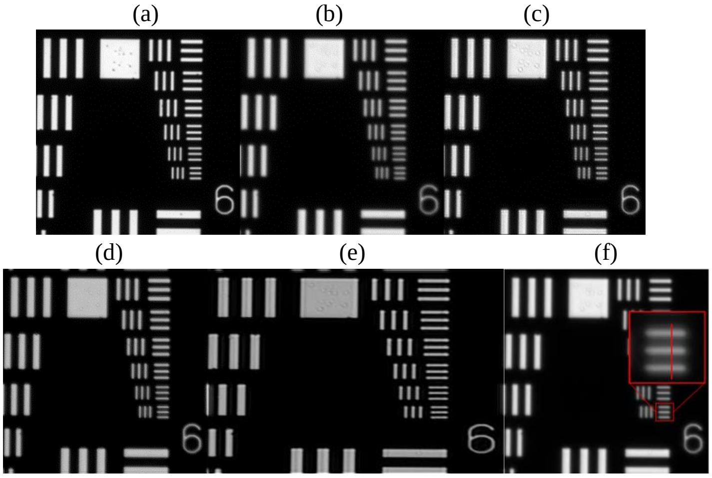

Fig. 4. a) in-focus image of the resolution test target detected with a microscopy objective 10X(0.3); b) defocused image of the object which amount of defocus is $\omega_{2,0} = 0.585$; c) restoration of the defocused using a simulated *ipsf*; d) restoration with the Blind deconvolution algorithm, with 100 iterations; e) restoration with our proposed optical-digital technique; f) this image is showing the transverse section that is used for the profiles plotted in the figure 5.

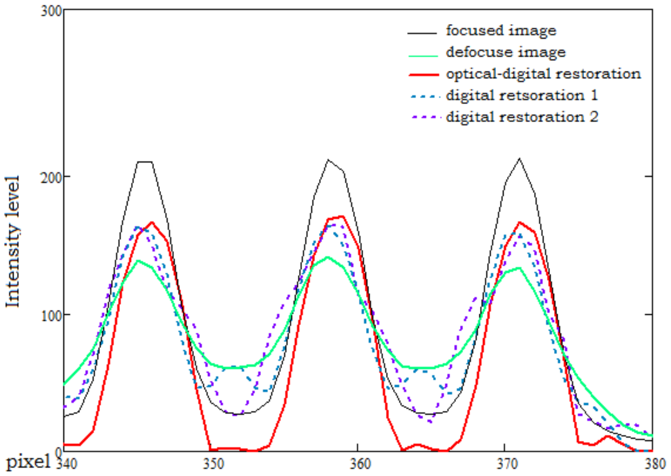

Fig. 5. Intensity profiles in the indicated region in Figure 4(f). Optical-digital technique (continuous red line), using a simulated *ipsf* (dotted blue line), the Blind deconvolution algorithm (dotted purple line), also both the profile of the in-focus image (continuous black line), and out-of-focus image (continuous green line).

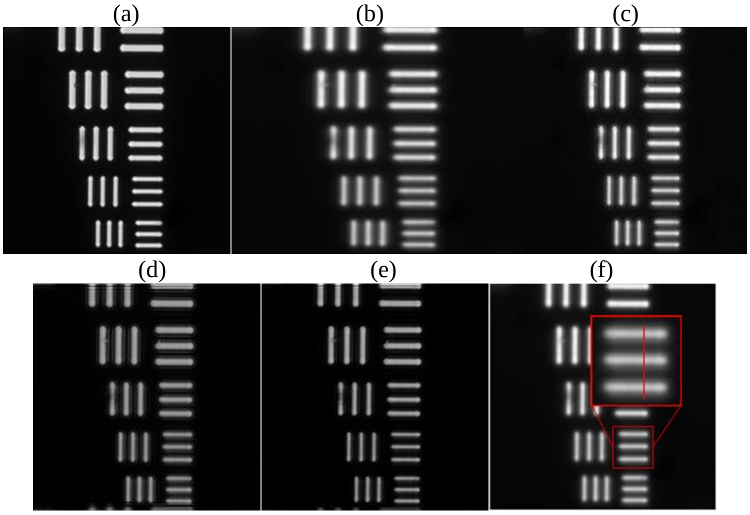

Fig. 6. a) in-focus image of the resolution test target detected with a microscopy objective 20X(0.5); b) defocused image of the object which amount of defocus is $\omega_{2,0} = 0.813$; c) restoration of the defocused using a simulated *ipsf*; d) restoration with the Blind deconvolution algorithm, with 100 iterations; e) restoration with our proposed optical-digital technique; f) this image is showing the transverse section that is used for the profiles plotted in the figure 7.

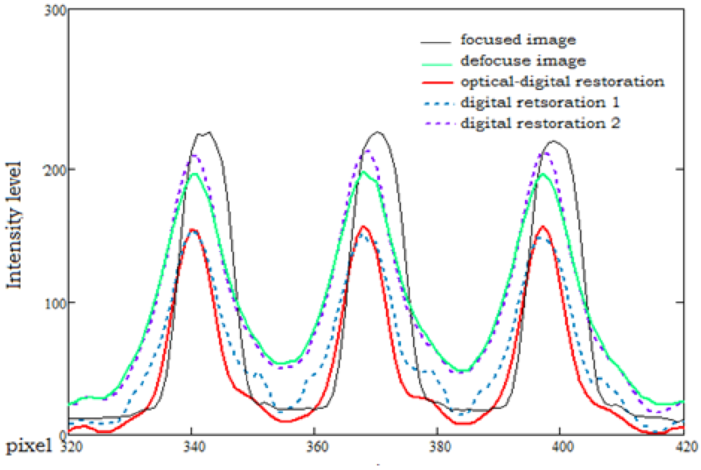

Fig. 7. Intensity profiles in the indicated region in Figure 6(f). Optical-digital technique (continuous red line), using a simulated *ipsf* (dotted blue line), the Blind deconvolution algorithm (dotted purple line), also both the profile of the in-focus image (continuous black line), and out-of-focus image (continuous green line).

6 Conclusions

Although, for a rigorous comparison is necessary a quantitative evaluation of the restoration techniques, for the moment we have made only a visual evaluation.

However with a simple visual inspection of the restoration, is easily appreciated the differences between our optical-digital method with the only digital. The advantages of the optical-digital method over the other two are evident in the three groups of images. Particularly, in the region of the image containing high frequencies, where the edges are restored in a fair way. However the contrast in the restoration resulted better for the digital simulated method instead of the other two.

After observing and comparing all the restored images, we can conclude that the method presented here works for restoring images detected out-of focus for the three different numerical apertures used in the experiment, and provides some advantages over the other two methods. Nevertheless a more exhaustive study is necessary for a complete characterization of our technique.

References

1. Weinstein. W.: Image of incoherent illuminated bright and opaque disks. J. Opt. Soc. Am., 45(12), pp. 1006–1007 (1955)
2. Mejía-Romero, S., Berriel-Valdos, L. R., Aguilar, J. F., Orlando, I. J., Landgrave, J. E. A.: Discrete Wigner distribution function applied on images of quasi-point source objects in coherent illumination. In: SPIE Proceedings 8011, 22nd Congress of the International Commission for Optics: Light for the Development of the World, Puebla Mexico (2011)
3. Ortiz-Sosa, R., Berriel-Valdos, L. R., Aguilar, J. F., Carranza-Gallardo, J., Orlando-Guerrero, I. J., Mejía-Romero, S.: Optical-digital restoration of out-of-focus color images detected in microscopy. In: SPIE Proceedings 8011, 22nd Congress of the International Commission for Optics: Light for the Development of the World, Puebla Mexico. (November 2011),
4. Gonzales, R. C., Goods, R. E.: Digital image processing. 3rd. Ed., New Jersey, Pearson Prentice Hall (2008)
5. Raveh, I., Mendlovic, D., Zalevsky, Z., Lohmann, A. W.: Digital method for defocus corrections: experimental results. Optical Engineering, 38(10), pp. 1620–1626 (1999)
6. Berriel, L. R., Bescós, J., Santisteban, A.: Image restoration for a defocused optical system. Applied Optics, 22(18), pp. 2772–2780 (1983)
7. Fish, D. A., Brinicombe, A. M., Pike, E. R.: Blind deconvolution by means of the Richardson-Lucy algorithm. J. Opt. Soc. Am., 12(1), pp. 58–65 (1995)
8. Hopkins, H. H.: Wave theory of aberrations. New York: Oxford Univ. Press (1950)
9. Hopkins, H. H.: The Frequency Response of a Defocused Optical System. Proceedings of the Royal Society of London, Series A, Mathematical and Physical Sciences, 231(1184), pp. 91–103 (1955)
10. Goodman, J. W.: Introduction to Fourier Optics. 2nd. Ed., New York, McGraw-Hill (1968)

ISSN 1870-4069

Design of Hartmann Null Screens for Testing Plane-convex Aspheric Lens

Gabriel Castillo-Santiago, Diana Castán-Ricaño, Maximino Avendaño-Alejo

Universidad Nacional Autónoma de México,
Centro de Ciencias Aplicadas y Desarrollo Tecnológico,
México

{Gabriel Castillo-Santiago, Diana Castán-Ricaño, maximino.avendano}@ccadet.unam.mx

Abstract. A new method to design Hartmann null screens for testing aspheric lenses is presented. It is based on the exact ray tracing equation, consider a plane wavefront impinging on the lens.

Keywords: Hartmann null screens, aspheric lens, testing.

1 Introduction

A spot diagram are points representing the intersections of rays from a point object given within a focal plane of a lens, on the other hand an experimental procedure similar to spot diagram is the Hartmann test in order to evaluate lenses.

For us, the null test involve simplicity, because it is straightforward to recognize a predefined pattern of spots. Some examples for Null test were described by reflection in [1] or refraction [2], but in the case of lenses with arbitrary aspheric terms as far as we know, there is no analysis by using null tests by refraction in both plane-convex and convex-plane configuration.

2 Designing Hartmann Null Screen

We define that the **Z** axis is parallel to the optical axis and we assume that the **Y-Z** plane is the plane of incidence, there is rotational symmetry about the **Z** axis. We consider ideally a bundle of rays propagating parallel to the optical axis, crossing the aspheric surface of the lens having two refractions, the first is represented by ($PaPi$), and the second refraction it is produced at the plane surface, it is represented by ($PiP0$) as is shown in Fig. 1(a).

Let h be the height of every incident ray, t is the thickness of the lens, ni the index of refraction of the lens for a predefined wavelength which is immersed in a medium with index of refraction *na, (ni > na)*, and where we have assumed that S_{h_N} represents the aspheric equation in a meridional plane which is given by

$$S_{h_N} = \frac{ch^2}{1+\sqrt{1-(k+1)c^2h^2}} + \sum_{i=1}^{N} A_{2i}h^{2i}, \qquad \textbf{(1)}$$

where c = 1/R is the paraxial curvature, k is the conic constant, A_{2i}, are the aspheric order terms with N the number of aspheric terms included in the polynomial. According to reference [3] the equation for (P_iP_0) refracted outside of the aspheric lens be expressed by

$$y = h - \frac{(n_i^2 - n_a^2)(t - S_{h_N})S'_{h_N}}{n_i^2 + n_a\Lambda} - \frac{(n_i^2 - n_a^2)(z - t)S'_{h_N}}{\sqrt{n_a^2(n_a+\Lambda)^2 - (n_i^2 - n_a^2)^2 S'^2_{h_N}}}, \qquad \textbf{(2)}$$

where:
S'_{h_N} is the first derivate of Eq. (1) with respect to h, and we have redefined $\Lambda = \left[n_i^2 + (n_i^2 - n_a^2)S'^2_{h_N}\right]^{1/2}$

To calculate the positions of the points on the Hartmann null screens, we follow all the steps well explained in [1], starting at the detection plane which has a predefined size of a CCD sensor, then the coordinates of the point pi in the aspheric surface are not selected a priori but must be calculated giving an arbitrary point $p_0 = (z_0, y_0)$ at the detection plane, and using the exact ray tracing equation as is shown in Fig.1(b).

In this work we design Null screens for both, plane-convex and convex-plane configurations, the complete equations are well explained in reference [3], the detection plane has been located in the paraxial plane in order to evaluate the spherical aberration in aspheric lenses which theory is described in [4]. In others words, by substituting y→ y0 and z→z0 in to Eq. (2) and solving for h we obtain the values for h_i which will form the null screens to test the lens

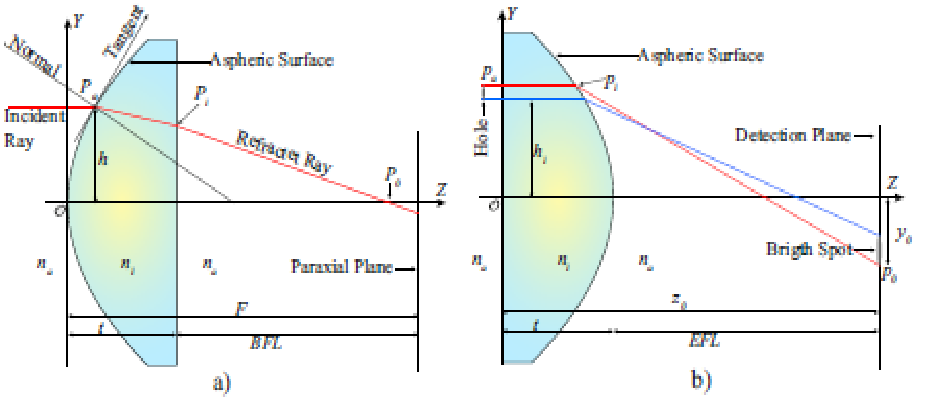

Fig. 1. a) Process of refraction produced by an aspheric lens, and their associated parameters in the convex-plane configuration. b) Process to design null screens in a plane-convex configuration aspheric lens.

3 Qualitative Evaluation

In this work we have evaluated qualitatively a lens with F/#=0.86, by using the following parameters: $n_a = 1$, $n_i = 1.523$ *for* $\lambda = 780nm$, $R = 13.8595mm$, $k = -1$, $t = 11.04mm$, *diameter* $D = 30mm$, and entrance aperture $H = \pm D/2$, these values correspond to item *ACL3026* from Thorlabs. The diagram of the experimental setup is show in Fig. 2, where two polarizers can be seen, which have been used to reduce the intensity of the laser beam on the CCD sensor, the screens have been printed on acetate foils using a photographic printer specified at 150 lines. The CCD sensor has an active area of A = 6.6mm×8.8mm and 480×640pixels respectively. The light source is a He-Ne laser with spatial filtering and a collimated beam, where a collimator lens with F/# = 6 has been implemented to reduce the central hot spot by increasing the distance between the collimator lens and the pinhole.

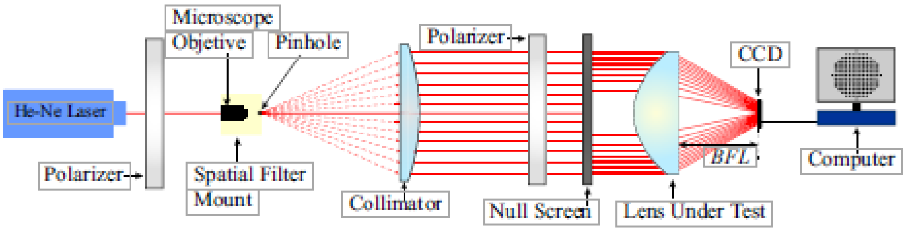

Fig. 2. Diagram of the experimental setup to test a plane-convex aspherical lens using null screens.

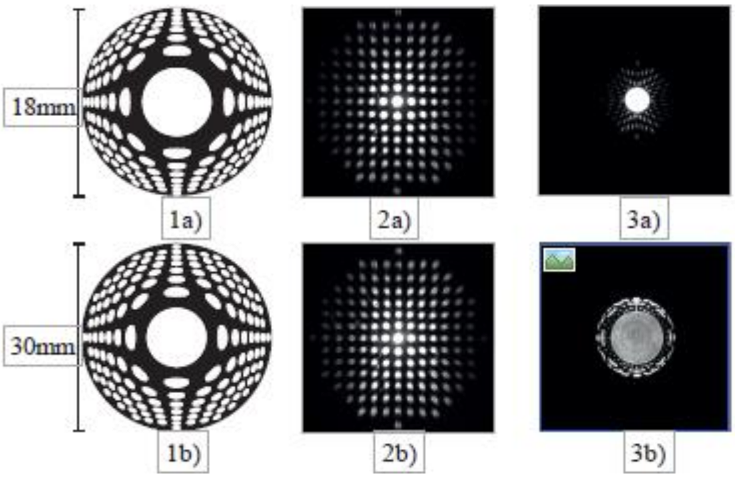

Fig. 3. 1a) Null screen with 15 drops in the central line for plane-convex configuration, 2a) Image recorded on the CCD at the focal length, 3a) Image recorded out of the plane of design. 1b) Null screen for convex-plane configuration 2b) Uniform array recorded at the CCD in the back focal length, 3. Image recorded inside the caustic region.

It is important to state that if visual observations are made in real time, the computed spots used as null screen can be calculated to produce an observable pattern of adequate size for the lens under test at a predefined detection plane as are show in Fig. 3, the non-uniformity of intensity recorded on the CCD sensor such as are shown in Fig. 3 (2) could be produced by several factors, but a graduated filter at the collimator, or even as part of the null screen, can be used as a possible solution to obtain a uniform intensity distribution of the incident beam on the CCD sensor.

In plane-convex configuration we can observe that the null screen has a smaller coverage in the entrance aperture than convex-plane configuration, it is due to that the marginal rays undergo total internal reflection as is show in Fig. 3 (1a and 1b), diffraction effects can be seen in some drops due to small size of the holes of the null screens. In Fig. 3 (2b) the images for convex-plane configuration show less diffraction effects than plane-convex configuration, but a high mechanical accuracy is required.

4 Conclusions

A simple method to design null screens in order to test by refraction either plane-convex or convex-plane configuration aspheric lenses has been presented by using drops arrays which were printed on acetate foil by using a photographic printed specified at 150 lines. The null screens in convex-plane configuration coverage more area than plane-convex configuration. This method can be used to evaluate quantitatively the spherical aberration, furthermore to reconstruction of the shape of the surface.

Acknowledgments. This work has been partially supported by CONACYT (#168570) and PAPIIT-UNAM (#IN114414).

References

1. Rufino Díaz-Uribe and Manuel Campos-García, “Null-screen testing of a fast convex aspheric surfaces,” Appl. Opt., 39, 2670-2677 (2000).
2. M. Avendaño-Alejo, Dulce González-Utrera, Naser Qureshi, Luis Castañeda, “Null Ronchi-Hartmann test for a lens,” Opt. Exp., 18, 21131-21137 (2010).
3. G. Castillo-Santiago, “Design and evaluation of physical properties for fast plane-convex aspheric lenses,” M. Eng. dissertation in process (UNAM, 2014).
4. Castillo-Santiago G., Avendaño-Alejo M., Díaz-Uribe R., Castañeda L.“Analytic aspheric coefficients to reduce the spherical aberration of lens elements used in collimated light,” Appl. Opt., 53, pp.4939-4946 (2014).

ISSN 1870-4069

Plasmonic Cloaking at a Conducting Sphere

I. Guadarrama-Lezama, P. Rosendo-Francisco

Universidad Autonoma del Estado de México, Facultad de Ciencias, Toluca,
Estado de México, Mexico

Abstract. Based on full wave Mie scattering theory for the case of an impenetrable/conducting sphere, we propose a technique which employs metamaterials and plasmonic structures to design cloaks. After showing how the total scattering cross section of a given dielectric or conducting object may be drastically reduced by surrounding with a suitable designed plasmonic material or metamaterial, we underline the main inherent limitations of this technique, compared with other metamaterial cloaking methods. The concepts that we present remain valid also when multiple particles are considered and they may be extended to multi-frequency operation, presence of ground planes or reflectors, larger objects and realistic loss and dispersion.

Keywords: invisibility cloaks, plasmonics.

1 Introduction

Recent technological advancements have encouraged many researchers to concentrate their works on theoretical and experimental aspects of artificial materials and metamaterials composed of molecular-like electrically small inclusions that may interact with the electromagnetic wave at different frequencies in an anomalous fashion. The attention of the media and of the general public for these materials has been mainly attracted by some potentially breakthrough applications, like the possibility of making a given object “invisible” (A. Alu and N. Engheta, 2005, 2007).

The interest of the electromagnetic and physics community in invisibility and cloaking indeed dates back several decades. Already at the beginning of last century, specific and properly designed distributions of oscillating sources with no radiation were predicted, and the concepts of “invisible” particles, sources and antennas have been investigated for several decades in a variety of scientific fields. Our proposal to apply metamaterials and plasmonic materials to cloaking (A. Alu et al., 2005) is based on the local negative polarizability of materials with a low or negative effective permittivity. When these materials surround a dielectric or conducting object, the overall scattering from the system may, under proper conditions, be designed to become extremely low, orders of magnitude lower than that of the uncloaked object by itself.

This effect relies on a scattering cancellation for which the wave scattered from the cloak may cancel the one from the object to be cloaked, leaving an external observer with a very low residual scattering that makes the system practically invisible around the design frequency. This cancellation is very distinct from, and in many ways potentially advantageous to, other cloaking techniques, being independent of the form

pp. 75–78; rec. 2017-05-14; acc. 2017-11-18

and polarization of the illuminating source. Moreover, we have shown how this technique is inherently non-resonant, and consequently it is fairly robust to variations in the shape, geometry and frequency of operation of the cloak and/or of the object to be covered. This effect may be achieved with naturally available plasmonic materials at THz, infrared and optical frequencies, since it may be based on simple isotropic and homogeneous covers, or it may be realized, at different frequencies, with metamaterials.

Other interesting solutions have recently been proposed in the framework of metamaterial cloaking (J.B. Pendry, D. Schuring, and D. R: Smith, 2006). Of particular interest, two alternative general ways of cloaking may be underlined: the possibility of applying conformal transformations and space distortions in order to tailor and design a metamaterial cloak capable of isolating a given region of space from the surrounding, and the possibility of applying anomalous localized resonant elements, and consequently exhibit strong sensitivity on frequency and on the geometrical and electromagnetic parameters of cloak. Moreover, at present stage they have mainly envisioned for 2D geometries and for complex anisotropies and inhomogeneity profile for the involved material.

In the following, we provide some numerical results on our solution from plasmonic cloaking, underlining the potentials of this solution in terms of cloaking effectiveness reduction, with particular attention to the inherent limitations that the use of metamaterials in these setups may imply. These results may have important potential applications requiring reduction in scattering, and also for low-noise measurements and non-invasive probing in medicine, biology and optics.

2 Numerical Results

Figure 1 reports a numerical simulation based on full wave Mie scattering theory for the case of an impenetrable/conducting sphere of radius $a = \lambda 0 /10$ illuminated by a plane wave travelling from bottom to top of the figure.

We may select different covers to cancel or drastically suppress the scattering from the sphere. One design corresponding to Fig. 1a, has permittivity $\varepsilon\ 0 /10$ and thickness, whereas the second design, corresponding to Fig. 1b, has permittivity e_0 / 20 and ac = 1.05a. The figure reports the total magnetic field distribution (amplitude) on the E plane, but similar results are obtained also on the other plane of polarization. This clearly shows the drastic scattering reduction that the plasmonic cloaks may provide, as compared with the case of a bare sphere (Fig. 1c) or of a conducting sphere occupying also the cloak region (Fig. 1d).

Quantitatively, the scattering cross section is reduced by over 95% with this simple design.

Compared to other available techniques that employ metamaterials for the same purposes (J.B. Pendry et al., 2006; D. Schuring et al., 2006; S.A. Cummer et al., 2006; D.Schurig et al., 2006), this solution does not involve the use of particularly complex material profiles, and its effective in 3D and for an arbitrary polarization and wave front of the impinging wave. Moreover, we have recently extended these concepts to the case of multiple neighboring objects to be cloaked, possible presence of a ground plane and larger systems, as well as to multiple frequency operations. It is noticed that the present simulations involve an impenetrable perfectly conducting object, which may also model a conducting spherical hollow cavity. Since the wave cannot penetrate into the cavity, and its total scattering cross section may be made very small using this cloak, it may be possible to fill the cavity with any object without perturbing the present result. In this way, we may envision the modeling of a cloaking system, composed of the combination of the designed cloak and a spherical hollow cavity, which is totally independent of the specific object to be cloaked.

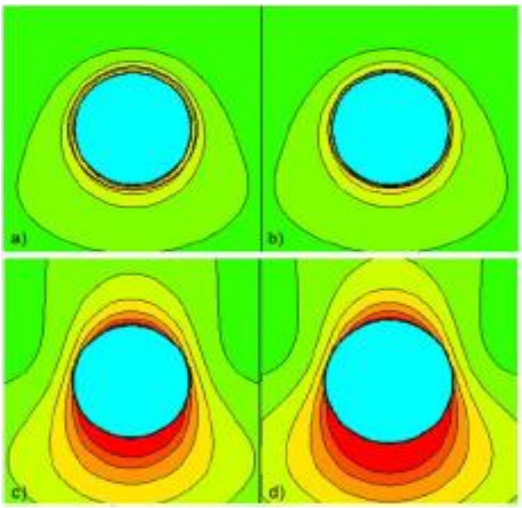

Fig. 1. Magnetic field distribution (amplitude) in the E-plane for the four cases of: (a) $\varepsilon_c = \varepsilon_0 10$ and $a_c = 1.1a$; b) $\varepsilon_c = \varepsilon_0 / 20$ and $a_c = 1.05a$; (c) $\varepsilon_c = \varepsilon_0$, (d) $\varepsilon_c = -i\infty$ and $a_c = 1.08a$. Brighter colors correspond to larger values of the field. For better comparison, the color scale is the same in the four plots. The geometry of the four spheres is depicted in black in the figures.

It is interesting to underline that, despite the outstanding reduction of scattering produced by the cloak in Fig. 1a and Fig. 1b, and in particular of the shadow on the back of the object caused by the presence of an impenetrable obstacle, the geometry under analysis requires some inherent limitations on its overall bandwidth of operation. From a general point of view, requiring that an impinging signal is indeed rerouted around an impenetrable obstacle through the (passive) cloak region implies an inherent delay in the cloak response. We directly associated this with a limitation in the bandwidth of operation which becomes more stringent for larger systems.

As we have noticed in Ref. [2], the technique that we have discussed here is quite robust in this sense, allowing getting closer to the inherent limitations required by causality, which are also projected in the required frequency dispersion of metamaterials. Compared with other techniques (Pendry et al. Schuring-7), the plasmonic cloaks presented here may have a relatively larger bandwidth of operation, in particular when dielectric and penetrable objects are considered, for which in the so design the electromagnetics wave may also penetrate the object, without being necessarily rerouted around it.

3 Conclusions

The sample numerical results presented here fully conform our previous works on the possibility of cloaking impenetrable and dielectric objects with plasmonics materials with low permittivity. The discussion on the inherent limitations of this phenomenon forecasts promising applications of this cloaking technique which may be relatively more robust than other metamaterial cloaking techniques. These results may pave the way to novel exciting application for cloaking and low-noise sensing.

References

1. A. Alu, and N. Engheta (2005), Achieving Transparency with Plasmonic and Metamaterial Coatings, Phys. Rev. E, 72, 016623
2. A. Alu, and N. Engheta (2007), Plasmonic Materials in Transparency and Cloaking Problems: Mechanism, Robustness, and Physical Insights, Optics Express, 15, 3318-3331.
3. M. G. Silveirinha, A. Alu, and N. Engheta (2007), Parallel-Plate Metamaterials for Cloaking Structures, Phys. Rev. E 75, 036603.
4. A. Alu, and N. Engheta (2007), Cloaking and Transparency for Colllections of Particles with Metamaterial and Plasmonic Covers, Optics Express, 15, 7578-7590.
5. J.B. Pendry, D. Schuring, and D. R: Smith (2006), Controlling Electromagnetic Fields, Science, 312, 1780-1782.
6. D. Schuring, J.J. Mock, B.J. Justice, S.A. Cummer, J.B. Pendry, A.F. Starr, and D.R. Smith (2006), Metamaterial Electromagnetic Cloak at Microwave Frequencies, Science, 314, 977-980.
7. S.A. Cummer, B.I. Popa, d. Schuring, D.R. Smith and J.B. Pendry (2006), Full-Wave Simulations of Electromagnetic Cloaking structures, Phys. Rev. E, 74, 036621.
8. D.Schurig, J. B. Pendry, and D.R. Smith (2006), "Calculation of Material Properties and Ray Tracing in Transformation Media," Optics Express, 14, 9794-9804.

ISSN 1870-4069

Liquid Fuel Identification Using a Fiber Optic Sensor Based in Multimode Interference Effects (MMI)

Adolfo J. Rodríguez-Rodríguez, René F. Domínguez-Cruz, Daniel A. May-Arrioja

Centro de Investigaciones en Óptica (CIO), campus Aguascalientes, Aguascalientes,
Mexico

darrioja@cio.mx

Abstract. In this work, we show the fabrication of a fiber optic sensor for the liquid fuel identification which is based on multimodal interference effects (MMI). The sensor structure is formed by a no-core multimode fiber (NC-MMF) splicing between two SMF. When the NC-MMF is immersed in a liquid combustible, the conditions of effective refractive index and the effective diameter of the NC-MMF are modified. Thus and the spectral shift of an optical signal output is used as refractometer to identify every kind of fuel. This MMI sensor exhibits a sensitivity of 258.06 nm/RIU for substances with a refraction index (RIU) from 1.318 to 1.4203 range. To test of the sensor, we use four of the most employed industrial and commercial combustibles like: methanol (M100), ethanol anhydrous (E100), gasohol (E50 to E10) and gasoline 87 octanes (G87). The sensor also provides high repeatability, reversibility and exhibit a fast and simple fabrication process. In addition, we show that the sensor response is enhancing by reducing the diameter of the NC-MMF.

Keywords: fiber optical sensor; multimodal interference effect; refractometer; liquid fuels.

1 Introduction

At the present, some alternatives of renewable fuel sources have been proposed as consequence of the growing demand of petroleum and green combustible. In this sense, methanol and ethanol are also used as fuel, especially when mixed with gasoline. Also the calorific value of gasoline is approximately twice the calorific value of methanol, thus making it more rentable. Some advantages of methanol as diesel combustible to vehicles are: it can be produced from renewable sources and waste of grass, bagasse sugar, litter, among others; generates less environmental pollution than fossil fuels and ordinary vehicles can use this combustible only replacing the plastic parts of fuel system (Reed et at, 1973; Olah et al, 2009).

Pure ethanol (E100) has become a very popular choice as fuel in markets such as Brazil, USA, Sweden, Thailand and others, with the advantage that combustion is less polluting and highly oxygenated. This combustible comes from sugar cane and corn as well cellulosic biomass and trees and grasses. It should be noted that the maximum permissible exposure in United States of America in air (40 h/ week) is

1,900 mg/m3 for ethanol, 900 mg/m3 for gasoline and 260 mg/m3 for methanol. Ethanol is also employed as additive in gasoline to replace the Methyl Tert-Butyl Ether (MTBE), responsible for significant contamination of soil and groundwater. The resulting fuel mixture of ethanol and gasoline is called gasohol (West et al, 2007; Goldemberg, J. 2008).

As example, in USA there are two common blends of ethanol with gasoline named E10 and E85, which means an ethanol presence of 10% and 85% in the mixture, respectively. Since alcohol has corrosive properties, special adaptations to conventional engine vehicles that employ ordinary gasoline are required; otherwise the engine is at risk of degradation in some component materials as well in the fuel system (Ethanol fuel and cars, 2008). Therefore, the design of novel techniques and sensors that allow the accurate the detection and identification of combustible with real time monitoring is quite important to avoid any potential damage in the automotive system.

Some techniques to detect combustible and hydrocarbons are based in the use of chemiresistors (Clifford et al 2002), piezoresonance sensors systems (Kalach et al 2007), photoacoustic sensors (Freborn et al 1998), electronic fuel analyzers (Testing Kits-PetroFLAG, 2014) and infrared fuel concentration analyzers (Control Instruments Corporation 2014, Zeltex®, 2014). Although these electronic sensors have efficient results for the measurement of liquid combustibles, oils and hydrocarbons, they may be sensitive to electromagnetic interference, exhibit a low selective drift for a particular hydrocarbon, relative high power consumption, some are expensive and unsuitable for remote operation. Optical fibers sensors are an attractive option due to their inherent characteristics such as good sensitivity, immunity to electromagnetic interference, small size, portability, low cost, high resolution, simple light coupling and the possibility for multiplexed operation (Lee, 2003, Marazuela et al, 2002). Some approaches have been investigated using Long Period Gratings (Felate et al, 2003), Fiber Bragg Gratings (Spirin et al, 1999) and incorporating sensitive polymer around the fiber (López et al, 2002; MacLean et al, 2003; Treviño et al, 2005; Sensfelder et al, 1998). However, the main inconvenient in these systems is the need for a special preparation of the fiber or the deposition of a sensitive material. A fiber sensor that can be suited for the detection and identification is the one based on multimode interference effects (MMI). MMI sensors can be high sensitive to RI changes of liquids

(Wang et al, 2006; Antonio-López et al, 2009; Wu et al, 2011; Walbaum et al, 2011; Socorro et al, 2013). In this work we demonstrate the application of a MMI optical fiber sensor as a tool to distinguish different kind of liquid combustibles. The advantages of the proposed sensor are it shown a simple fabrication, exhibits great reproducibility, reversibility and no temperature interference.

2 Materials and Methods

As is showed in Figure 1, the MMI structure is constructed by splicing a segment of No Core-MMF between two SMF segments. When an optical signal from the SMF segment propagates within the NC-MMF segment are excited all modes allowed within it, interfering with each other giving rise to an interference that is highly dependent on the phase relationship between modes. For a certain length L, where the phase difference is a multiple of 2π, we have the formation of self-images which are an exact reproduction of the input field. Therefore, by carefully selecting the length of the NC-MMF segment, light coupled through the first SMF segment, will be reproduced to the second SMF segment.

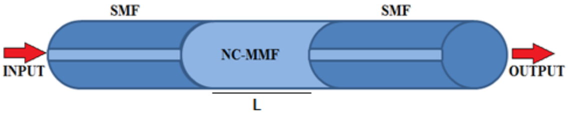

Fig. 1. Structure of the MMI element based in fiber optic.

The length of the MMF segment to which the effect of self-image is presented, for a specific wavelength can be calculated employing the following Equation 1 (Walbaum et al, 2011; Socorro et al, 2013):

$$L = p\frac{n_{MMF}D_{MMF}^2}{\lambda_0} \qquad \text{with} \quad p = 0,1,2\ldots \tag{1}$$

where n_{MMF} and D_{MMF} are respectively the effective refractive index and the diameter of the fundamental mode of the NC-MMF segment, and λ_0 is the wavelength in free space. As shown in Eq. (1), the self-images are formed periodically along the NC-MMF segment, however, we want to work in every fourth image since they have minimum losses as compared to other images and the response of the MMI refractometer under a wide spectrum source will be similar to a band-pass filter as shown in Figure 2.

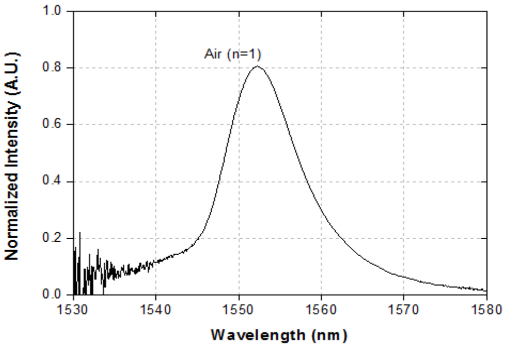

Fig. 2. Wavelength spectral response of MMI when is surrounded by air.

2.1 Sensor Fabrication

The NC- MMF used in our experiments is provided by Prime Optical Fiber Corporation (Japan), which is a MMF with a core diameter of 125 μm without cladding and a refractive index of 1.444. Before to fabricate the MMI structures we need to obtain the exact length of the NC-MMF that will provide the desired MMI peak wavelength. According to Eq. (1), we employ a NC-MMF segment of 58.98 mm spliced between two segments of SMF-28 (core diameter of 125 μm) at a wavelength of 1530 nm for the case of the fourth self-image p=4 using a Fujikura® splicer FSM-

50S. The NC-MMF cladding was removed with acetone to clean any remaining residue. The final MMI sensor has a structure similar that showed in Figure 1.

2.2 Experimental Array

The experimental set-up for testing the MMI sensor is shown in Figure 3. A Superluminiscent Diode (SLD) centered at 1550 nm was connected to the input SMF of the MMI sensor, and the output SMF is then connected an optical spectrum analyzer (OSA) Agilent® 86142A to capture the transmitted spectrum. We use a chamber to fix the MMI sensor. This chamber included input and output tubes to insertion and removal of the substances. Since both MMI sensor and substances are sensitive to temperature, the measurements were performed at controlled temperature of 20° C.

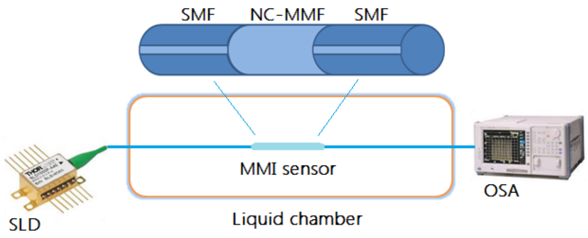

Fig. 3. Experimental set-up to identify different liquid fuels.

In order to test the utility of MMI structure designed as a refractometer, mixtures of water and glycerin

were prepared at different concentration to obtain a range of RI from 1.318 (100% water) to 1.4204 (30% water/70% glycerin). Later, we cover the sensor MMI using each one of the mixtures and monitoring the wavelength shift of the peak transmitted on the structure (Figure 4) and we observe a clear resolution of MMI for each blend of water with glycerin. The next step to probe the MMI sensor was testing with different liquid fuels.

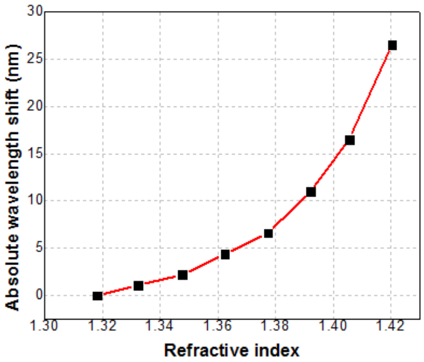

Fig. 4. MMI peak wavelength shift as a function of the RI (water and glycerin).

3 Results and Discussion

In Figure 5, we present the spectrum response of the MMI device for different kinds of liquid combustibles as methanol (M100), ethanol (E100), gasohol (E50…E10) and 87 octanes gasoline (G87). In order to visualizing these results, we graph the RI estimated for each fuel with the wavelength shift peak observed considering wavelength peak in air as reference (Figure 6- black line). From this curve, the sensitivity is estimated as 258.06 nm/RIU in 1530.2-1558.1 nm range using a NC-MMF core diameter @ 125 µm.

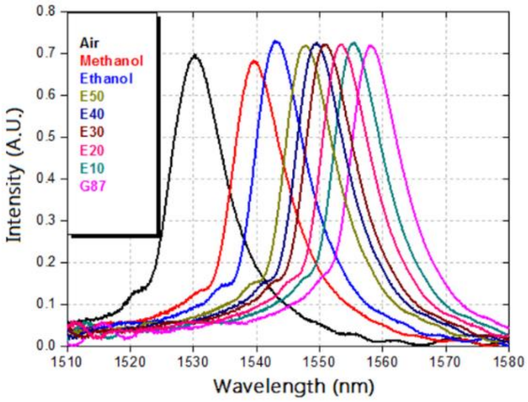

Fig. 5. Spectral response of the MMI sensor for different liquid fuels.

As shown in Figure 5 (black line) the peak wavelength in air is at 1530.2 nm which is very close to the design wavelength of 1530 nm. When a sample of methanol (n~1.318, λ=1530 nm, T=20°C) provided by Sigma-Aldrich® is inserted in the chamber we can observe a wavelength shift of 9.3 nm, with the peak wavelength at 1539.5 nm. When the sensor is exposed to anhydrous ethanol (n~1.3465, λ=1530 nm, T=20°C) provided by Sigma-Aldrich®, the MMI peak wavelength

is shifted to 1542.9 nm. Although the shift is relatively small respect to Methanol (~3.4 nm) it can be easily resolved by the OSA. It is important remark that we used anhydrous ethanol rather than standard ethanol, because ethanol tends to absorb water and it could modify the RI value. We prepared solutions of commercial G87 with different proportions of anhydrous ethanol. When the sensor is exposed to E50 (Gasohol prepared by EtOH 50% / G87 50%) (n~1.3852, λ=1530 nm, T=20°C), the MMI peak wavelength is shifted to 1547.7 nm and we can see a considerable wavelength shift (~4.8 nm) respect to ethanol.

As shown in Figure 5, the volume of anhydrous ethanol is decreased in 1 ml and volume of G87 is increased in 1 ml in each sample for E50 to E10. That carries to a spectral response shift to longer wavelengths. Although the wavelength shift in this blends is ~1.7 nm, (E50 to E10) the MMI sensor can identify each one of gasohol combustibles. Finally, when commercial G87 (n~1.424, λ=1530 nm, T=20°C) is covering the sensor, the MMI peak wavelength is shifted to 1558.1 nm. Although the shift is small (~2.6 nm respect to E10) it can be easily resolved by the OSA. Based on these results we should be able to identify each one of the most useful liquids combustibles, by comparing the measured peak of each one.

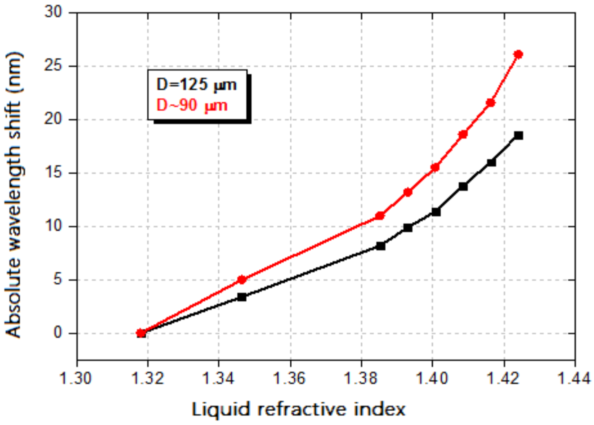

Fig. 6. Absolute wavelength shift (nm) as a function of the liquid RI for two different NC-MMF diameters.

It is well known that the sensitivity of MMI sensors can be increased by reducing the diameter of the NC-MMF (Antonio-López et al, 2009). According to Eq. (1), if the diameter of the NC-MMF is reduced then its length has to be reduced to obtain the same MMI peak wavelength. Therefore, using Eq. (1) we can calculate the required NC-MMF length for a diameter of 90 µm and a peak wavelength of 1530.3 nm, which result in a NC-MMF length of 30.57 mm. The reduction of the NC-MMF diameter was performed by immersing the fiber in buffered oxide etching (BOE) solution, which is a mixture of hydrofluoric acid and ammonium fluoride as the buffer agent. Since the etching rate is relatively slow (~130 nm/min), we can monitor the transmitted spectrum in real time. After a total time to 135 min we can observe that the MMI peak wavelength is at λ=1530.3 nm. The new MMI sensor with reduced diameter was tested again for the methanol, ethanol anhydrous, gasohol (E50…E10) and G87. As shown in Figure 6, the peak wavelength shift is increased for all the liquids combustibles, but is more significant when the NC-MMF diameter is reduced.

4 Conclusions

We demonstrated the application of a MMI optical fiber sensor as a tool for the detection and identification of different liquid fuels. We tested MMI sensor employing four industrial and commercial combustibles like: methanol (M100), ethanol anhydrous (E100), gasohol (E50 to E10) and gasoline 87 octanes (G87). This MMI sensor exhibits a sensitivity of 258.06 nm/RIU for substances with RI ranging from 1.318 to 1.4203, therefore we can accurately determinate the identification of different liquids combustibles over a broad wavelength range. The advantages of the sensor are that its fabrication is straightforward, and exhibits great reproducibility and reversibility, with no significant interference against temperature or humidity.

We also explored the feasibility of enhancing the sensor response by reducing the diameter of the NC-MMF.

Acknowledgements. We appreciate the support from the Consejo Nacional de Ciencia y Tecnología (CONACyT) under grant CB-2010/157866.

References

1. Antonio-López, J. E., López-Cortes, D., Basurto-Pensado, M. A., May-Arrioja, D. A., Sánchez-Mondragón, J. J.: All-fiber multimode interference refractometer sensor. Proc. SPIE, 7316 (2009)
2. Clifford, K., Hughes, H., Hughes, R. C.: In Situ Chemiresistor Sensor Package For Real Time Detection of Volatile Organic Compounds in Soil and Groundwater. Sensors, 2002, Vol. 2, pp. 23–24 (2009)
3. Control Instruments Corporation. Infrared Analyzers. Available at: http://www.controlinstruments.com/technologies/infrared-analyzers (2014)
4. Ethanol fuel and cars. Available at: http://interestingenergyfacts.blogspot.mx /2008/09/ethanol-fuel-and-cars.html (2015)
5. Felate, R, Müller, M., Fabris, J. L., Kalinowski, H. J.: Long Period Gratings in Standard Telecommunication Optical Fibers for Fuel Quality Control. In: Procc. XXVI ENFMC. Annals of Optics, Vol. 5 (2003)
6. Freborn, S. S., Hannigan, J., Greig, F.: A pulsed Photoacustic Instrument for the Detection of Crude Oil Concentrations in Produced Water. American Institute of Physics, Review of Scientific Instruments, Vol. 69, pp. 3948–3952 (1998)
7. Goldemberg, J.: The Brazilian biofuels industry. Biotechnology for Biofuels 2008, Available at: http://www.biotechnologyforbiofuels.com/content/1/1/6 (2014)
8. Kalach, A. V., Selemenev, V. F.: A piezoresonance sensor system for rapid evaluation of the quality of gasolines. Chem Tech Fuels Oil, Vol. 43, pp. 60–61 (2007)
9. Lee, B.: Review of the present status of optical fiber sensors. Opt. Fiber Technol, Vol. 9, pp. 57–59 (2003)
10. López, R. M., Spirin, V. V., Miridonov, S. V., Shlyagin, M. G., Beltrán, G., Kuzin, E. A.: Sensor de fibra óptica distribuido para la localización de fugas de hidrocarburo basado en mediciones de transmisión/reflexión. Revista Mexicana de Física, Vol. 48, No. 5, pp. 457–462 (2002)
11. MacLean, A., Moran, C., Johnstone, W., Culshaw, B., Marsh, D., Walker, P.: Detection of hydrocarbon fuel spills using a distributed fibre optic sensor. Sens. Act. A., Vol. 109, pp. 60–67 (2003)
12. Marazuela, M. D., Moreno-Bondi, M. C.: Fiber-optic biosensors-an overview. Anal. Bioanal. Chem, 87, pp. 289–295 (2002)
13. Olah, G., Goeppert, A., Surya-Prakas, G. K.: Beyond Oil and Gas: The Metanol Economy. Second edition, Willey Vch Verlag Gmbh (2009)
14. Reed, T. B., Lerner, R. M.: Methanol: A Versatile Fuel for Immediate Use. Science, Vol. 182, pp. 4119 (1973)
15. Sensfelder, E., Bürck. J., Ache, H. J.: Characterization of a Fiber Optic System for the Distributed Measurement of Leakages in Tanks and Pipelines. Applied Spectroscopy, Vol. 52, pp. 1283–1298 (1998)
16. Socorro, A. B., Del Villar, I., Corres, J., Arregui, F. J., Matias, I. R.: Mode transition in complex refractive index coated single-mode-multimode-single-mode structure. Opt. Exp., Vol. 21, No. 10 (2013)
17. Spirin, V. V., Shlyagin, M. G., Miridonov, S. V., Mendieta-Jiménez, F. J., López-

Gutiérrez, R. M.: Fiber Bragg grating sensor for petroleum hydrocarbon leak detection. Opt. Lass. Eng. Vol. 32, No. 5, pp. 497–503 (1999)

18. Testing Kits-PetroFLAG-Analizador cuantificación de hidrocarburos en el suelo. Available at: http://www.ambicare.com/es/productos/testes-rapidos/petroflag-analizador-cuantificacion-de-hidrocarburos-en-el-suelo (2015)
19. Treviño-Santoyo, A., Shlyagin, M. G., Mendieta, F. J., Spirin, V. V., Niño de Rivera, L.: Variación del espectro de transmitancia de una fibra óptica con recubrimiento de polímero por influencia de hidrocarburos y cambios de temperatura. Revista Mexicana de Física, Vol. 51, No. 6, pp. 600–604 (2005)
20. Wang, Q., Farrell, G.: All-fiber multimode-interference-based refractometer sensor: proposal and design. Opt. Lett., Vol. 31, pp. 317–319 (2006)
21. Walbaum, T., Fallnich, C.: Multimode interference filter tuning of a mode-locked all-fiber erbium laser. Opt. Lett., Vol. 36, pp. 2459–2461 (2011)
22. West, B. H., López, A. J., Theiss, T. J., Graves, R. L., Storey, J. M., Lewis, S. A.: Fuel Economy and Emissions of the Ethanol Optimized Saab 9-5 Biopower. Available at: https://www1.eere.energy.gov/bioenergy/pdfs/analysis_saab2007. pdf (2015)
23. Wu, Q., Semenova, Y., Wang, P., Farrel, G.: High sensitivity SMS fiber structure based refractometer-Analysis and experiment. Opt. Express, Vol. 19, pp. 7937–7944 (2011)
24. Zeltex® ZX-440-XL Near Infrared Gasoline/Diesel Fuel Analyzer. Available at: http://www.zeltex.com/desktop/zx-440xl.pdf (2015)

ISSN 1870-4069

Experimental Setup to Measure Dispersion in Optical Fiber Devices

Luis Alberto Rodríguez Morales, Iván Armas Rivera, Georgina Beltrán Pérez

Benemérita Universidad Autónoma de Puebla, Puebla,
Mexico

Abstract. Some of the different factors that lower performance of the optical fiber and experimental components are attenuation and dispersion. Some are intrinsic to the material and cannot be deleted, but can be compensated, so it is therefore necessary to quantify the chromatic dispersion. This paper presents a method for measuring the coefficient of dispersion in a WDM and an optical isolator, caused by the temporal broadening of a pulse due to the different speeds that are in the optical frequencies of said pulse. The Mach-Zehnder interferometer has many applications, in this paper it´s one, in which a WDM and Optical insolator are analyzed, the data obtained by the method were channeled by a measured optical spectrum (OSA for its acronym) and then analyzed on the computer with a program previously done in Matlab. The results clearly show that the dispersion can be measured with high accuracy not only optical fibers but also in other optical devices.

Keywords: optics fiber, dispersion, WDM, optical isolator.

1 Introduction

Dispersion is a quite important parameter in systems based on optical fiber since it affects the original temporal profile with which the data have been sent. It also reduces the number of channels that can be transmitted simultaneously. Therefore, it is necessary to consider the dispersion provoked by each optical component of the system.

The chromatic dispersion in an optical fiber is originated by the effective refractive index variation as a wavelength function. This parameter can affect the bandwidth of a high speed optical transmission system, broadening the pulse and causing errors in the received information. Among the most important methods used to measure chromatic dispersion in long length optical fibers there can be mentioned the following: the pulse-delay method which measures the difference between modes in optical pulses with various wavelengths. Even though this is a very simple and inexpensive technique, pulse broadening due to chromatic dispersion degrades its accuracy, since this makes difficult to accurately determine the arrival time of a pulse [*L. G. Cohen,* et al.]. Another technique is the modulation phase-shift techniques that use the time-of-flight method to measure chromatic dispersion. This method is accurate and repeatable. Phase-modulated optical signals are transmitted through a long sample of an optical fiber, and their phase delays are measured as a function of the wavelength.

However, this technique has several drawbacks. First, the accuracy of this method is restricted when the selected wavelength is far from the reference wavelength, with large phase differences between the reference and test-sample arms generating ambiguities in phase-shift measurement. Second, it requires a complicated experimental setup and expensive equipment such as a high-speed optical modulator and an optical tunable filter. Finally, it cannot measure the chromatic dispersion of a short fiber sample [L. G. Cohen, et al], [J. Brendel, et al]. In the present work an experimental arrangement to measure chromatic dispersion in optical fibers of short length using a configuration based on a Mach-Zehnder interferometer is proposed. The device under test (DUT) is located in one arm while an air arm reference is used to obtain the spectral interferogram. This technique is capable of performing a sweep of several wavelengths in milliseconds, besides it is quite simple to implement. The versatility of this experimental setup allows the easy replacement of the fiber under test for its characterization. With this, we might measure the chromatic dispersion in non-conventional fibers which do not have datasheet available about their dispersion coefficient.

The obtained results with the present technique can be used to optimize communication systems based in optical elements composed by fiber, increasing the transmission data capacity and decreasing the error rate in the reception.

2 Experimental Setup

Our experimental setup for the measurement of material dispersion is a Mach-Zehnder interferometer, this arrangement consists in two arms, where one arm is formed by the DUT, the other one is made up of air. This interferometer is powered by a broadband source (1550 nm laser-diode, Polarizers plates, two 50/50 couplers, and two lenses to collimate the beam arm through which the beam travels in air. The Fig 1 shows the experimental setup.

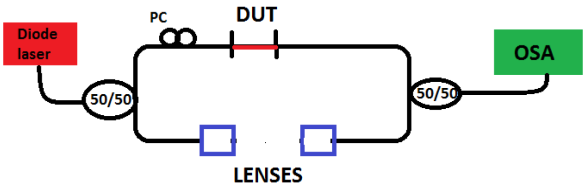

Fig. 1. Experimental arrangement to measure chromatic dispersion in single mode optical fiber based on a Mach-Zehder interferometer.

3 Theoretical Considerations

The intensity is related to the field as follows: “$I=|E|^2$", if the explicit dependencies are omitted to simplify the expression intensity as interferometer this is expressed like:

$$I = I_0\{1 + 2\alpha(\alpha - 1)[1 + \cos(\beta(\lambda)L - \beta_0 L_0). \tag{1}$$

Then only remains us to obtain the phase of the cosine term to obtain an estimate of "β(λ)", if we assume that this process of phase extraction has already been done, we can do a change of variable "λ" by "f" expressing the relative phase as:

$$\phi(f) = \beta(f)L - \beta_0 L_0, \tag{2}$$

where $\beta(f)$ is the propagation constant of the transmitted light on the test device. The delay time associated with the reference arm in the interferometer is defined as $\tau_{0=\frac{L_0}{C_0}}$,so the relative phase is expressed as:

$$\phi(f) = \beta(f)L - 2\pi\tau_0 f. \tag{3}$$

Differentiating the phase with respect to the optical frequency are:

$$\frac{1}{2\pi}\frac{d\phi(f)}{df} = \tau_g(f) - \tau_0, \tag{4}$$

where

$$\tau_g(f) = \frac{L}{v_g(f)} = \frac{L}{2\pi}\frac{d\beta(f)}{df}. \tag{5}$$

Then the derivative of delay group respect to the wavelength provides the coefficient of dispersion value. So we made a variable change from "f" to "λ", then calculate the phase's second derivate to have it.

$$D = \frac{1}{L}\frac{d\tau_g}{d\lambda_0}. \tag{6}$$

4 Results

To obtain the dispersion value, various interferograms were measured changing the optical path difference in order to determine the optimum optical path. The dispersion coefficient is calculated using just the interferogram obtained with such optical path. To obtain more precise and reliable values is necessary to take various measurements with the same parameters and to calculate an average.

The cross correlation interferogram obtained directly from the OSA within a range of 200 nm is shown in Figure 2 and Figure 3. It can be noted that the plot shape resembles that for the diode laser, however it is modulated depending on the optical path, which can be changed with the translation stages.

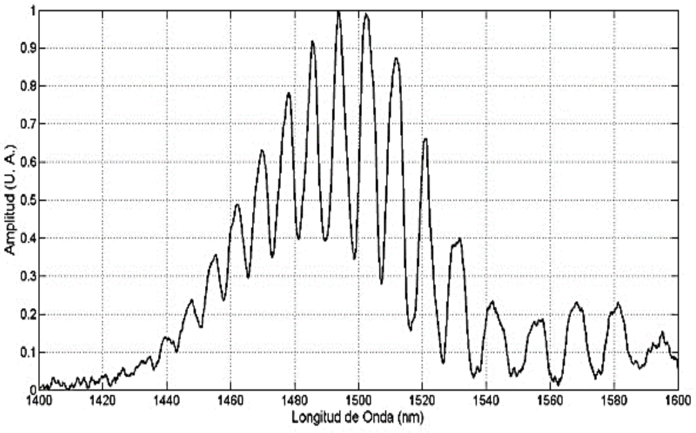

Fig. 2. WDM interferogram.

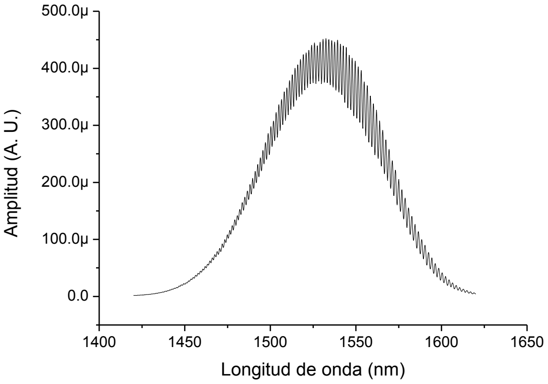

Fig. 3. Optical isolator interferogram.

Unlike the results obtained in previously reported works [*J. Y. Lee, et al.*], where the phase is calculated by measuring the separation between positive fringe peaks from the spectral interferogram, in this work we measure the phase behavior in function of wavelength using Fourier transformation [*Mitsuo Takeda, et al.*]. We use a Fast-Fourier-Transformed algorithm (FFT) to filter unwanted information such as slow spatial variation, compared with the carrier frequency, and amplitude variations. Again, using the FFT algorithm, we apply the inverse Fourier transform to the filtered signal to obtain the phase simply dividing the imaginary part by the real part. This phase is wrapped, therefore is necessary to apply an algorithm to unwrap it. This dependence is in terms of the wavelength, however it is necessary to perform a variable change since equation 2 is in terms of frequency.

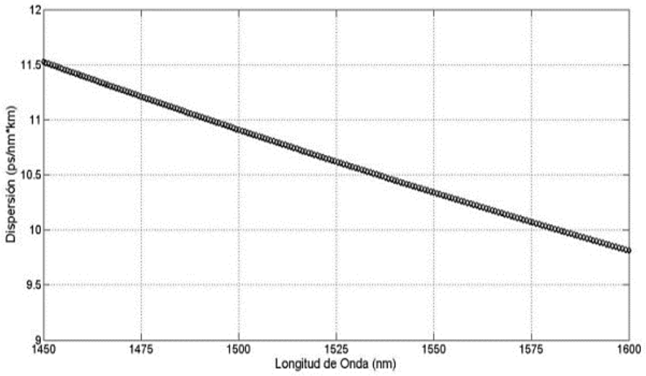

Fig. 4. WDM dispersion curve.

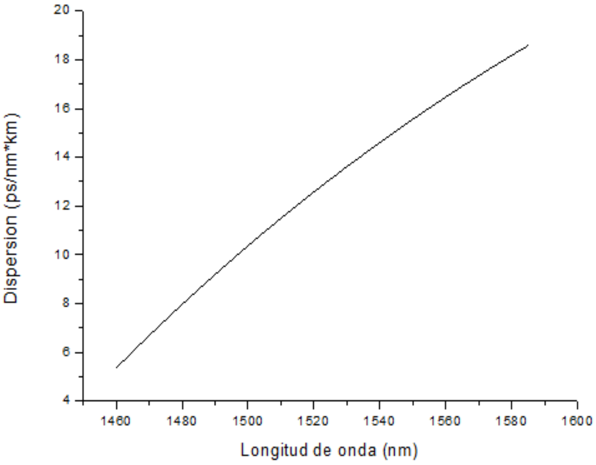

Fig. 5. Optical isolator dispersion curve.

Once the phase behavior was obtained it was performed a fitting using a third order polynomial.

Based on equations 3 and 5, the first derivative respect to the frequency of this expression was calculated to obtain the group delay, and the second derivative respect to the wavelength was calculated to obtain the dispersion coefficient. With this procedure the results shown in Fig. 4 and Fig. 5 were obtained. The shown dispersion values were experimentally obtained using two different wavelength resolutions (0.5 and 1 nm, dotted line and dashed line, respectively).

5 Discussion and Conclusions

Nowadays in the Laboratory of Electronics and Optoelectronics, LEyO, we have an interferometric system to measure of the coefficient of dispersion in optical fibers in a wavelength range of 1520-1570 nm. This system is based on a Mach-Zehnder interferometer, where the reference arm light travels through the air.

The biggest advantage of this system is that it only measures for a fiber length of several tens of centimeters is required in addition to the great simplicity to change the fiber under test as temporary connectors are used for connection to the system.

In this work an experimental arrangement to evaluate dispersion in WDM and optical isolator were developed. At the umbral of 1550 nm, which is the umbral of the communication, the WDM has a dispersion about 10 ps/nm*Km and the optical isolator about 14 ps/nm*Km.

The contribution to the dispersion value due to the optical elements that compose the experimental arrangement has been neglected owing to the fact that their physical dimensions are much shorter that the DUT. On the other hand it is thought that the same effects of each element are present in both arms of the interferometer and that their contribution is quite small.

Acknowledgments. This word was supported by project VIEP-BUAP BEPGEXC14-I and PRODEP 2014.

References

1. Armas-Rivera, I.: Método para la medición de la dispersión en fibras ópticas por medio de un interferómetro de Mach-Zehnder. Tesis de licenciatura, México, BUAP (2011)
2. Saleh, B. E. A., Teich, M. C.: Fundamentals of Photonics. Wiley, Second Edition, (2007)
3. Brendel, J., Zbinden, H., Gision, N.: Measurement of chromatic dispersion in optical fibers using pairs of correlated photons. Opt. Commun., 151, pp. 35–39 (1998)
4. Lee, J. Y., Kim, D. Y.: Versatile chromatic dispersion measurement of a single mode fiber using spectral white light interferometry. Republic of Korea (2006)
5. Cohen, L. G.: Comparison of single-mode fiber dispersion measurement techniques. J. Lightwave Technol., 3, pp. 958–966 (1985)
6. Cohen, L. G., Chinlon, L.: Pulse delay measurements in the zero material dispersion wavelength region for optical fibers. Appl. Opt., 16, pp. 3136–3139 (1977)
7. Takeda, M., Ina, H., Kobayashi, S.: Fourier-transform method of fringe-pattern analysis for computer-based topography and interferometry. Tokyo, Japan (1981)
8. Hui, R., O'Sullivan, M.: Fiber Optic Measurement Techniques. Elsevier Academic Press (2009)

ISSN 1870-4069

Sudden Death of Entanglement of Two Quantum Dots Embedded in Its Own Cavity

S. Sánchez-Sánchez[1], J. J. Sánchez Mondragón[3], F. R. Castillo Soria[2],
V. I. Moreno Oliva[1], E. Román Hernández[1]

[1] Instituto de estudios de la Energía, Universidad del Istmo, Carrera de Matemáticas Aplicadas,
Oaxaca, Mexico

[2] Universidad del Istmo, Carrera de Ingeniería en Computación,
Oaxaca Mexico

[3] Instituto Nacional de Astrofísica Óptica y Electrónica, Departamento de Óptica,
Puebla, Mexico

ssanys1@hotmail.com, ssanchez@bianni.unistmo.edu.mx, jjsanchez@inaoep.mx

Abstract. Entanglement of quantum systems is a key aspect to understanding the dynamics and behavior of mixed systems (density matrix) as bipartite quantum bits (qubits). Thus we need to have a reliable and accurate way to measure the entanglement degree of the system, i.e., how it evolves, so that raises several approaches to meet these demands. A quantifiable measure widely used is the "entanglement of formation" of a mixed state, defined as the minimum number required of "singlets" to create a set of pure states that represents the density matrix of the system. In this paper we consider a system of two semiconductor quantum dots embedded in its own cavity and coupled to the internal mode field of cavity type Jaynes-Cummings. The entanglement between the two quantum dots is investigated, and we show analytically that entanglement has very interesting, effects such as time evolution including the effect called sudden death.

Keywords: entanglement, quantum dots, semiconductors, sudden death.

1 Introduction

By several years, many authors have studied entanglement because their enormous importance at a fundamental level and because its applications to quantum information and quantum computing (Nielsen and Chuang, 2000). Entanglement has marked a new way to reinterpret the quantum nature of computer technology due to the incorporation of quantum processing units with so-called quantum bits (q-bits), represented as dual units that open up infinite possibilities of parallel processing, at least theoretically, much faster than any classical computational process.

However this has been the case at the theoretical level, therefore it is essential to implement physical models that allow the incorporation of this development into feasible systems or where the technological inertia may lead to, and one of the most visible are Quantum Dots (QDs). In spite that we usually refer to QDs as Atom like structures, there are substantial differences such as the exchange interaction (Förster interaction), (Sanchez-Mondragon, Alejo-Molina, S. Sanchez-Sanchez, 2005 & 2009) which has been used as the basis for proposals of quantum computation, and therefore deserve a careful analysis.

Quantum entanglement has played very important roles in quantum information processing such as quantum teleportation (Nielsen and Chuang, 2000) quantum cryptographic, quantum dense coding (Bennett, Wiesner, 1992) and parallel computing (DiVincenzo, 1995). Therefore a precise measurement is needed to quantify the degree of entanglement for those qubits system in collaboration or competition with such exchange interaction. This is more interesting because the physical character and mathematical structure of entangled states have not been well understood and the Förster interaction tuning opens new possibilities to deal with its fundamental questions. There are two important problems for entanglement. One is to find a method to determine whether a given state is separable (or not entangled), and the other one, it is to define the best measurement quantifying an amount of entanglement of a given state. In order to solve the first problem, much effort has been made, [6-8]. The quest for proper measurement of entanglement has received also a great deal of attention. The entanglement of formation, distillation, and relative entropy, (Bennett, DiVincenzo, Smolin, Wootters, 1996) negativity, concurrence (Hill, Wootters, 1997; Wootters, 1998) concurrence related measures, or positive operator are used to investigate entanglement.

Although the entanglement of formation is defined for arbitrary-dimensional bipartite systems, so far no explicit analytic formulates for entanglement of formation have been found for systems larger than a pair of qubits, except for some special symmetric states (Terhal, Gerd, Vollbrecht, 2000).

Another serious problem that must be considered in entanglement, as mentioned earlier, in a quantum system is it may deteriorate due to interaction with background noise or with other systems usually called environments. Interest was originally concerned with the consequences for quantum measurement and the quantum-classical transition (Joos, Zeh, et. al. 2003). More recently, entanglement decoherence has been studied in connection with obstacles to realize various quantum information processing schemes. T. Yu and Eberly have shown that entanglement can decay to zero abruptly, in a finite time, a phenomenon termed *entanglement sudden death* (Yu and Eberly, 2004; Yu and Eberly, 2006).

Such quantum correlations are responsible for much of the challenge in understanding interacting many-body quantum systems, and it is therefore of fundamental importance to have quantitative knowledge of these correlations. Progress in quantum information theory has led to the development of new measures of the inseparability of a quantum state, and in the last few years these measures have been used to assess the quantum correlations in diverse physical systems. Concurrence is an especially useful metric for such studies because it can be applied to mixed as well as pure states. It therefore can be used to quantify the thermal entanglement in a system at nonzero temperature. It can also be applied to evaluate the inseparabililty of an equal incoherent mixture of degenerate energy eigenstates. However as we mentioned above, concurrence is defined only for a pair of qubits. Since a qubit is formally equivalent to a spin-1/2 particle when only the spin degree of freedom of the latter is considered, this has led to several analyses of the thermal entanglement between a pair of interacting spin-1/2 particles. Entanglement of formation, is another important entanglement measure, which can be calculated directly from the concurrence and is monotonically related to it. The method of calculating the concurrence for more general density matrices can be found in Wootters.

The importance of this issue is to find necessary and sufficient conditions for the development of quantum computer systems in their physical implementation (hardware) and the new rules of quantum processing (software). In our case we focus on studying the physical implementation on a fundamental level, seeking the most appropriate quantum physical system of many systems studied in quantum physics for many decades to more sophisticated atomic systems with cooperative and collective effects. Up until now, such quantum-mechanical computers have been proposed in terms of trapped ions and atoms, cavity quantum electrodynamics (QED), nuclear magnetic resonance, Josephson junctions, and semiconductor nanostructures schemes. However all of the above proposals have decoherence and operational errors as the main obstacles for their experimental realization, which pose much stronger problems here than in classical computers. There is much current excitement about the possibility of using solid-state-based devices for the reliable rendering of quantum computation tasks.

In particular, semiconductor nanostructure fabrication technology is well developed and hence offers us a wide and promising arena for the challenging project of building quantum information processors. Because of their quantum-mechanical nature and their potential scalability properties, semiconductor quantum dots (QDs) are very promising candidates for the implementation of quantum computing processes. Several solid-state design schemes for quantum computation have been proposed to date: Kane (B.E. Kane, 1998) has proposed a scheme that encodes information onto the nuclear spins of donor atoms in doped silicon electronic devices where externally applied electric fields are used to perform logical operations on individual spins. Loss and Di-Vincenzo have presented a scheme based on electron spin effects, in which coupled quantum dots are used as a quantum gate. This scheme is based on the fact that the electron spins on the dots have an exchange interaction (Forster interaction) which changes sign with increasing external magnetic field.

In this paper we consider a double quantum dot system coupled to the mode Jaynes-Cummings cavity type, thus we investigate the entanglement between two quantum dots, each embedded in his own cavity, and we show analytically that entanglement has interesting effects such as temporal evolution, as well as the so-called sudden death effect. The system composed of two quantum dots were previously entangled before that these were immersed into the cavity. We study this system in the context of cavity quantum electrodynamics (C-QED). However we must to clarify that this is not a paper on QDs systems for quantum computing applications. It's just a proposal about semiconductors QDs in quantum optics and C-QED fundamentals, which we used to do the theoretical study, also supported by the entanglement of formation procedure as a quantitative measure for the entanglement between our qubits: i.e. the two quantum dots system more the cavities.

2 Concurrence and Entanglement of Formation

Entanglement is a fundamental insight of quantum mechanics, which corresponds to the presence of nonlocal correlations between different parts of a system that cannot be explained classically. That is, a pure state of a pair of quantum systems (bipartite) is called entangled if it is not factorizable (i.e., if the state total cannot be written as a product of states of the particle) and a mixed state is entangled if it can be represented as the mixed state pure factorizable. For both pure and mixed quantum states, there are good measures of the degree of entanglement. In the case of pure states of a bipartite system there is a single widely accepted measure of entanglement, whereas for mixed states of such systems there are three measures that have been extensively studied. One of these, *entanglement of formation*, is a subject of this paper. We use the concurrence of Woosters as a measure in this work, mainly for its importance for mixed states and the convenience of its definition and normalization.

2.2 Entanglement of Formation for a System of Two QDs

The key element in the quantum information processing is the so-called quantum bit. For this reason, understanding their behavior in quantum computing environments is essential to carry out external operations that perform specific calculations in locations on qubits by logic operations with new algorithms adapted to these qubits. So we should form networks of qubits at different intervals making full operations. In our case we have a small network of two QDs at the nodes of network under this study we will provide the means to insight the transfer at a distance of entanglement in the lattice network.

Our qubits are a system of two quantum dots which are located in their respective single-mode ($a,\ a^{\dagger}$ and $b,\ b^{\dagger}$), lossless cavities so that a cavity includes only one such dots. Thus, each node of our network consists of a cavity in which there is a QD. We will restrict our attention to the dynamics of entanglement between two such nodes. We will denote the dot at the first node by *A*, cavity at the first node by *a*, dot at the second node by *B* and cavity at the second node by *b*, as sketched in Fig. 1. We are going to be using the QDs Hamiltonian model (Sánchez-Sánchez, 2011).

Quiroga-Jhonson 1999; Reina-Quiroga-Jhonson) to specify the interactions in our system, this include the Förster interaction. The QDs Hamiltonians (defined the constant $\hbar = 1$) as we will use in next sections, i.e. equations (1), (2) and (3). We consider *L* identical semiconductor quantum dots that are equally coupled to each other via coulombic interaction. The QDs interact with a quantized field (dipole interaction) in a high-Q cavity. Then the coupled QD-field system is described by the Hamiltonian (Sanchez-Mondragon, Alejo-Molina, S. Sanchez-Sanchez, 2005 & 2009. Quiroga and Johnson 1999).

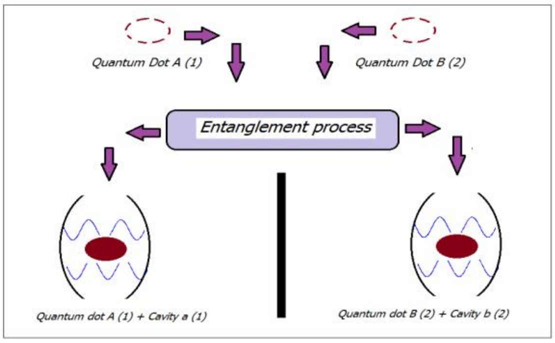

Fig. 1. This diagram show our system of two QDs previously entangled. The QDs are placed in their respective cavity, which there are not interaction between them.

With respect to two subsystems A and B

$$\begin{aligned} H^{(A)} &= \omega a^{\dagger} a + \varepsilon J_z^a + g_a\left(J_+^a a + a^{\dagger} J_-^a\right) + W_a\left(J_a^2 - \left(J_z^a\right)^2\right), \\ H^{(B)} &= \omega b^{\dagger} b + \varepsilon J_z^b + g_b\left(J_+^b b + b^{\dagger} J_-^b\right) + W_b\left(J_b^2 - \left(J_z^b\right)^2\right), \end{aligned} \qquad (1)$$

where ε is the QD band gap, $g_a = g_b = g$ is the coupling strength between the field and the QDs, ω is the field frequency, and W_a=W_b=W, represents the interdot coulomb interaction.

The coulomb interaction process known as Forster process exchanges energy, but does not require the physical transfer of the electrons and holes. For equal coupling these QDs are equidistant from each other so that the dots lie on a line for cases L = 2, at the vertices of an equilateral triangle for L = 3, and at the vertices of a regular pyramid for L = 4. The Hamiltonian (1) can be rewritten in a much more suitable in the representation of angular momentum, with the changes point out into references: (Sanchez-Sanchez S. 2011; Sanchez-Mondragon, Alejo-Molina, Sanchez-Sanchez S., 2005 & 2009. Quiroga and Johnson 1999), we obtained that may consist of two parts, first one with the Dicke H_{Dk} Hamiltonian itself and the other one is the interaction Hamiltonian Förster H_F, defined as $H_{Dk_{A.B}} = \Delta J_z^{a,b} + g\left(J_+^{a,b} a + a^{\dagger} J_-^{a,b}\right)$ and $H_F = W(J_{a,b}^2 - (J_z^{a,b})^2) = W J_+^{a,b} J_-^{a,b}$ where the constant Δ=$\varepsilon - \omega$ is the detuning between the electromagnetic field and the band-gap.

The Hamiltonian of L QDs can be rewritten in the form: $H = \omega N + Q_L$, with $N = a^{\dagger} a + J_z + L/2$ is the number of atoms and photons and $Q_L = H_{Dk} + H_F$ are constants of motion. It should be noted that the term of Förster $W J_+^{a,b} J_-^{a,b}$ is non-linear. Furthermore we introduced a new constants ε', defined as $\varepsilon' = \varepsilon - W$. However there is another way to rewrite the Hamiltonian (1), using the relations of the algebra of angular momentum, thus we rewrite the Hamiltonian to include explicitly the detuning Δ which now call *Förster Detuning* Δ', so we obtain:

$$\begin{aligned} H^{(A)} &= \omega\left(a^\dagger a + J_z^a\right) + g\left(J_+^a a + a^\dagger J_-^a\right) - \Delta' J_z^a + W J_+^a J_-^a, \\ H^{(B)} &= \omega\left(b^\dagger b + J_z^b\right) + g\left(J_+^b b + b^\dagger J_-^b\right) - \Delta' J_z^b + W J_+^b J_-^b, \end{aligned} \tag{2}$$

while the parameters are defined as: $\Delta'=\Delta+W=\omega-\varepsilon+W=\omega-\varepsilon'$. In a frame rotating with the field frequency ω, Eq. (2) takes the form:

$$\begin{aligned} H_F^{(A)} &= \Delta' J_z^a + g\left(J_+^a a + a^\dagger J_-^a\right) + W J_+^a J_-^a, \\ H_F^{(B)} &= \Delta' J_z^b + g\left(J_+^b b + b^\dagger J_-^b\right) + W J_+^b J_-^b. \end{aligned} \tag{3}$$

3 Two QDs Interacting with their Own Quantized Cavity Field: Hamiltonian Diagonalization

From now on we will use this Hamiltonian (3), for each of the subsystems in order to diagonalizar the Hamiltonian, i.e. splits into two subsystems which are represented as $H_T = H^{(A)} + H^{(B)}$. This will simplify the task of studying the time evolution of the QD-field system. Starting with the initial condition representing the vacuum of excitons (S. Sánchez-Sánchez, 2011) (Sanchez-Mondragon, Alejo-Molina, S. Sanchez-Sanchez, 2005 & 2009. Quiroga and Johnson 1999. And Mitra, Vyas, Erenso, 2007), $|j=1/2, m=-1/2\rangle = |\downarrow\rangle\sqrt{a^2+b^2}$, only the $j=1/2$ subspace is optically active while the $j=0$ subspace remains dark.

We choose the basis of eigenstates of J^2 and J_z, $|\downarrow\rangle = |j=1/2, m=-1/2\rangle$, $|\uparrow\rangle = |j=1/2, m=1/2\rangle$,as an appropriate representation for this problem $|\downarrow\rangle$ represents the vacuum for excitons, $|\uparrow\rangle$ denotes a symmetric delocalized single-exciton state. If we represent the field state intro each cavity by the Fock state $|n_a, n_b\rangle$ and consider the QDs in the entangled state involving the vacuum and exciton states $\left[|\uparrow\downarrow\rangle \pm |\downarrow\uparrow\rangle\right]$, then we will have an invariant subspace spanned by the tensor product $\left\{|\uparrow\downarrow\rangle\otimes|00\rangle; |\downarrow\uparrow\rangle\otimes|00\rangle; |\downarrow\downarrow\rangle\otimes|10\rangle; |\downarrow\downarrow\rangle\otimes|01\rangle\right\}$.

With these basis vectors we determine the matrix elements of the Hamiltonian in Eq. (3) and obtain the eigenvalues, and the eigenvectors by mean of diagonalization. The explicit matrix is

$$H_T = H^{(A)} + H^{(B)} = \begin{pmatrix} W & 0 & g & 0 \\ 0 & W & 0 & g \\ g & 0 & \Delta' & 0 \\ 0 & g & 0 & \Delta' \end{pmatrix}, \tag{4}$$

where $\Delta' = \omega - \varepsilon' = \Delta + W$. An interesting case is for $\Delta' = \omega - \varepsilon' = \Delta + W = 0 + W = W$, that is, when we have *resonance*. In next subsection we will use this case in order to calculate the Concurrence function and thus the Entanglement of Formation, for now we calculate the general case for the Hamiltonian diagonalization. The characteristic polynomial for matrix (4) is given by $P(\lambda) = \left[g^2 + (W-\lambda)\lambda - (W-\lambda)\Delta'\right]^2$.

At both cavities with the same field frequency ω, and we define the constants for simplicity as $\delta = \left[4g^2 + W^2 - 2W\Delta' + (\Delta')^2\right]^{1/2} = \left[W(W-2\Delta') + (4g^2 + (\Delta')^2)\right]^{1/2}$ the eigenvalues take the form: $\lambda_{E1,E2} = (1/2)(W + \Delta' - \delta)$, $\lambda_{E3,E4} = (1/2)(W + \Delta' + \delta)$; Due to the tensor product of the quantum states $|j,k\rangle = |j\rangle \otimes |k\rangle$ form a four-dimensional basis in the Hilbert space $\mathrm{SU(2)} \otimes \mathrm{SU(2)}$. And the corresponding normalized eigenvectors are:

$$\begin{aligned}
|\lambda_1\rangle &= \left(4g^2 + \Omega_1{}^2\right)^{-1/2}\left[(\Omega_1 |\uparrow\downarrow, 00\rangle + 2g|\downarrow\downarrow, 10\rangle\right], \\
|\lambda_2\rangle &= \left(4g^2 + \Omega_1{}^2\right)^{-1/2}\left[(\Omega_1 |\uparrow\uparrow, 00\rangle + 2g|\downarrow\uparrow, 01\rangle\right], . \\
|\lambda_3\rangle &= \left(4g^2 + \Omega_2{}^2\right)^{-1/2}\left[\Omega_2 |\uparrow\downarrow, 00\rangle + 2g|\downarrow\downarrow, 00\rangle\right], \\
|\lambda_4\rangle &= \left(4g^2 + \Omega_2{}^2\right)^{-1/2}\left[\Omega_2 |\uparrow\uparrow, 00\rangle + 2g|\downarrow\uparrow, 00\rangle\right].
\end{aligned} \tag{5}$$

Also we defined the frequencies and parameters by $\Omega_1 = W - \delta - \Delta'$, $\Omega_2 = W + \delta - \Delta'$. Then using the foregoing eigenvectors we get the wavefunction for any time. For this reason we need to consider the initial state of the quantum dots system. A suitable choice of initial state is a state of Bell. For the sake of generality; we use the initial state of the QDs to be $|\psi_{qd}(0)\rangle = \left[c_1|\uparrow\downarrow\rangle + c_2 e^{i\phi}|\downarrow\uparrow\rangle\right]$, where a_1 and a_2 are real constants satisfying the condition $c_1^2 + c_2^2 = 1$.We will consider the initial state of the field to be coherent, or thermal. Then, the initial state for the coupled QD-field system can then be written as

$$|\Psi(0)\rangle = |\psi_{qd}(0)\rangle \otimes |00\rangle = \left[c_1|\uparrow\downarrow\rangle + c_2 e^{i\phi}|\downarrow\uparrow\rangle\right] \otimes |00\rangle. \tag{6}$$

We are now able to find the wavefunction of the system, because the energy eigenstates form a complete set. Using the eigenvalues and eigenvectors (5), together with the initial state (6), (Mitra, Vyas, Erenso, 2007) we obtain the following state vector at the time *t*:

$$\begin{aligned}
&|\Psi(t)\rangle = \sum_{k=1}^{N=4} \exp(-i\lambda_{Ek}t)\langle\lambda_{Ek}|\Psi(0)\rangle|\lambda_{Ek}\rangle = \\
&e^{-i\lambda_1 t}\langle\lambda_1|\Psi(0)\rangle|\lambda_1\rangle + e^{-i\lambda_2 t}\langle\lambda_2|\Psi(0)\rangle|\lambda_2\rangle + e^{-i\lambda_3 t}\langle\lambda_3|\Psi(0)\rangle|\lambda_3\rangle + e^{-i\lambda_4 t}\langle\lambda_4|\Psi(0)\rangle|\lambda_4\rangle.
\end{aligned} \tag{7}$$

Due to the orthonormality of the basis vectors we get the coefficients as $x_i(\Omega_i,t)=x_i(t)=\langle jm,n|\Psi(t)\rangle$, and

$$\begin{aligned} x_1(t) &= c_1\frac{\left(\Omega_1^2+\Omega_2^2\right)e^{-i(\lambda_1+\lambda_3)t}}{\left[(4g^2+\Omega_1{}^2)(4g^2+\Omega_2{}^2)\right]}, \\ x_2(t) &= e^{i\phi_0}\left[\frac{c_1 4g^2 e^{-i\lambda_2 t}}{(4g^2+\Omega_1{}^2)}+\frac{c_2 4g^2 e^{-i\lambda_4 t}}{(4g^2+\Omega_2{}^2)}\right],. \\ x_3(t) &= c_1\frac{2g\Omega_1}{(4g^2+\Omega_1{}^2)}e^{-i\lambda_1 t}, \\ x_4(t) &= c_1\frac{2g\Omega_2}{(4g^2+\Omega_2{}^2)}e^{-i\lambda_3 t}. \end{aligned} \tag{8}$$

Then the solution of the system in terms of the standard basis can be written as a simple linear combination, i.e.

$$|\Psi(t)\rangle = x_1(t)|\uparrow\downarrow\rangle + x_2(t)|\downarrow\uparrow\rangle + x_3(t)|\downarrow\downarrow\rangle + x_4(t)|\downarrow\downarrow\rangle\,. \tag{9}$$

The coefficients $x_i(t)$ are given by equations (8). Based on these results that were obtained, in the following section we find the density matrix, as well as reduced density matrix in order to calculate the concurrence and entanglement of formation.

4 Entanglement of Formation for Two QDs as Qubits Implementation

For sake of simplicity, let us assume that both cavities are prepared initially in the vacuum state $|0_a\rangle\otimes|0_b\rangle$ and the two QDs are in a pure entangled state specified below as a Bell state. Under these assumptions, there is never more than one photon in each cavity, so the cavity mode is essentially equivalent to a two-level system. This allows a uniform measure of quantum entanglement together to concurrence, for both dots and the cavity modes.

According to the above we must note that there are, in principle, six different concurrences that provide information about the overall entanglements that may arise. We can denote simple form as follows: (Yönac, Yu and Eberly 2006 & 2007) C^{AB}, C^{Ab} , C^{Aa}, C^{Bb}, C^{Ab}, C^{Ba}. Symmetry considerations can provide natural relations among them. Here we confine our attention to C^{AB} .

So, it should note that we in reality have six *individual* systems and four qubits: i.e. the two QDs (*A* and *B*, see figure 1) represent two qubits and two cavities (*a* and *b*) represent other two qubits itself, plus the combinations in interaction between these system as we showed in concurrences. However, we focus only in the *AB* combination in order to measure the entanglement. For calculate the Entanglement of formation we need find the density matrix in general form of the coefficients $x_i(t)$, (Yönac, Yu and Eberly 2006 & 2007) That is, we must to compute the matrix elements, for density reduced matrix, whom work for us in order to find out *Spin-flipped matrix* which is an ingredient essential in *Concurrence function* for entanglement of formation. Here we show the resulting matrix:

$$\hat{\rho}=\begin{pmatrix} 0 & 0 & 0 & 0 \\ 0 & |x_1|^2 & x_1x_2^* & x_1\left(x_3^*+x_4^*\right) \\ 0 & x_1^*x_2 & |x_2|^2 & x_2\left(x_3^*+x_4^*\right) \\ 0 & x_1^*\left(x_3+x_4\right) & x_2^*\left(x_3+x_4\right) & |x_3|^2+|x_4|^2 \end{pmatrix}, \tag{10}$$

$$\hat{\rho}=\begin{pmatrix} a & 0 & 0 & w \\ 0 & b & z & 0 \\ 0 & z^* & c & 0 \\ w^* & 0 & 0 & d \end{pmatrix}.$$

In the combination of the four qubits that we use as system, appear most the features of character universal. But the simplest is first, all reduced to a two-qubit form, obtained by tracing over the two qubits, will yield a two-qubits mixed state always will have the standard X-form (Yönac M, Yu T and Eberly 2006 and 2007). Where $a+b+c+d=1$. Second, since the concurrence of this mixed state is easily found to be: $C=2\max\left\{0,|z|-\sqrt{ad},|w|-\sqrt{bc}\right\}\equiv 2\max\{0,Q\}$.

Also, we will encounter the case $w=0$, and this equation turns into: $C=2\max\left\{0,|z|-\sqrt{ad}\right\}\equiv 2\max\{0,Q\}$. So it is clear that *Q*, defined as

$$Q=|z|-\sqrt{ad}\,. \tag{11}$$

This will be an important quantity. Because this have certain *conservation* properties that derive from *Q* in some cases because it can be negative, whereas *C* cannot. The information about the entanglement of two QDs is contained in the reduced density matrix ρ^{AB} for the two dots which can be obtained from expressions (9) and (10) by tracing out the photonic parts of the total pure state. The explicit 4 × 4 matrix written in the basis $\left\{|\uparrow\uparrow\rangle;|\uparrow\downarrow\rangle;|\downarrow\uparrow\rangle;|\downarrow\downarrow\rangle\right\}$ (Yu, Yonac and Eberly 2002-2007) is given by

$$\hat{\rho}^{AB}=\begin{pmatrix} 0 & 0 & 0 & 0 \\ 0 & |x_1|^2 & x_1x_2^* & 0 \\ 0 & x_1^*x_2 & |x_2|^2 & 0 \\ 0 & 0 & 0 & |x_3|^2+|x_4|^2 \end{pmatrix}. \tag{12}$$

This is in the standard form of the two-qubit (quantum dots) mixed state, which was noted previously by (Yu T and Eberly J H 2007) in order to two level atoms case.

Once again the time-dependent matrix elements are given by (5), which we analyzing the case when the detuning is zero: $\Delta' = \omega - \varepsilon' = \Delta + W = 0 + W = W$,in resonance. It must be note that only to keep the Förster interaction constant. The total of constants defined into equations for coefficients in equations (8) and eigenvectors (5) are: $\Omega_1 = W - \delta - \Delta' = -2g,\quad \Omega_2 = W + \delta - \Delta' = 2g$ and $\delta = \left[W(W - 2\Delta') + (4g^2 + (\Delta')^2)\right]^{1/2} = 2g$ therefore the equations (5) and (8) now given by:

$$
\begin{aligned}
|\lambda_1\rangle &= \left(1/\sqrt{2}\right)\left[|\downarrow\downarrow,10\rangle - |\uparrow\downarrow,00\rangle\right],\\
|\lambda_2\rangle &= \left(1/\sqrt{2}\right)\left[|\downarrow\uparrow,01\rangle - |\uparrow\uparrow,00\rangle\right],\\
|\lambda_3\rangle &= \left(1/\sqrt{2}\right)\left[|\uparrow\downarrow,00\rangle + |\downarrow\downarrow,00\rangle\right],\\
|\lambda_4\rangle &= \left(1/\sqrt{2}\right)\left[|\uparrow\uparrow,00\rangle + |\downarrow\uparrow,00\rangle\right].
\end{aligned}
\tag{13}
$$

The coefficients must be normalized. Thus, the constants C_1 and C_2 into equations must to obey the normalization condition, also if compared to the eigenvectors obtained in eqs. (13), the latter are entangled states of Bell (resonant case) where the constants are actually of $1/\sqrt{2}$, except for the sign. Thus the equations for the coefficients are:

$$
\begin{aligned}
x_1(t) &= \frac{e^{-i2Wt}}{8\sqrt{2}g^2},\\
x_2(t) &= \frac{e^{i\phi_0}}{2\sqrt{2}}\left[e^{-i(W-g)t} + e^{-i(W+g)t}\right]\\
&= \frac{1}{\sqrt{2}}\cos\left(gt\right)e^{-iWt-i\phi_0},\\
x_3(t) &= -\frac{1}{2\sqrt{2}}e^{-i(W-g)t},\\
x_4(t) &= \frac{1}{2\sqrt{2}}e^{-i(W+g)t}.
\end{aligned}
\tag{14}
$$

Now we show that the concurrence of the density matrix (12), with references to equation (11), this is given first by function $Q_{AB}(t)$ as:

$$
\begin{aligned}
Q_{AB}(t) &= |z| - \sqrt{ad} = \left|x_1^* x_2 + x_1 x_2^*\right| - \sqrt{0}\\
&= \frac{1}{16g^2}\left|\cos(gt)\left(e^{-iWt}e^{-i\phi_0} + e^{iWt}e^{i\phi_0}\right)\right|,\\
Q_{AB}(t) &= \frac{1}{8g^2}\begin{cases} \left|\cos(\phi_0)\cos(gt)\cos(Wt)\right| & \Re(\text{part}),\\ \left|\sin(\phi_0)\cos(gt)\sin(Wt)\right| & \Im(\text{part}).\end{cases}
\end{aligned}
\tag{15}
$$

So that the Concurrence function we can be think in dual way, the first one as a function just of time, which is keeping constant, and the another one as a function of two variables, i.e. as function of the time and phase parameter.

For sake of simplicity we use only the real part in terms of the cosines functions. The imaginary part has a similar behavior. In the figures below we showed several cases for both functions with different values of parameters *W* and *g*. It must be noted that the plots have a behavior of cosine oscillations type, but self-modulate with a function of the same nature, i.e. cosine-cosine, and the amplitude not exceeding the one, as it should be for *Entanglement of Formation*. The graphics are showed in next section of results; and the functions for Concurrences are

$$\begin{aligned} C_{AB}(t) &= \frac{1}{8g^2}\left|\cos(\phi_0)\cos(gt)\cos(Wt)\right|, \\ \phi_0 &= \text{ fixed}, \\ C_{AB}(t,\phi_0) &= \frac{1}{8g^2}\left|\cos(\phi_0)\cos(gt)\cos(Wt)\right|, \\ \phi_0 &= \text{ independent variable.} \end{aligned} \tag{16}$$

5 Results

Before presenting graphical results with the plots simulations, first we want to show the analytical results without approach with limit cases on the physical parameters:

$$\begin{aligned} Q_{AB}(t) &= \left|\begin{matrix} \cos(\phi_0)\left(\cos(g+W)t+\cos((g-W)t)\right) \\ +i\sin(\phi_0)\left(\sin(g+W)t-\sin((g-W)t)\right) \end{matrix}\right| \times \frac{1}{16g^2}, \\ Q_{AB}(t) &= \frac{1}{8g^2}\cos(\phi_0)\cos(g)t, \qquad W=0. \end{aligned} \tag{17}$$

Now, when $g \gg W$, in this case, is the dominant parameter, i.e. the coupling constant between the radiation field and the QDs:

$$\begin{aligned} Q_{AB}(t) &= \frac{1}{8g^2}\left|\begin{matrix} \cos(\phi_0)\cos Wt\cos gt \\ +i\sin(\phi_0)\cos gt\sin Wt \end{matrix}\right|, \\ Q_{AB}^2(t) &= \left(\frac{1}{8g^2}\right)^2 \cos^2 gt \left(\begin{matrix} \cos^2(\phi_0)\cos^2 Wt \\ +\sin^2(\phi_0)\sin^2 Wt \end{matrix}\right), \\ Q_{AB}(t) &= \frac{1}{16g^2}\left|\begin{matrix} \cos(\phi_0)\left(\cos(g+W)t+\cos((g-W)t)\right) \\ +i\sin(\phi_0)\left(\sin(g+W)t-\sin((g-W)t)\right) \end{matrix}\right|. \end{aligned} \tag{18}$$

Another interesting case is when we add a parameter δ to the others parameters, which enables us to get analytical expressions more general, besides being able to manipulate this parameter numerically and perturbative way, i.e., $W = g+\delta;\ W \succ \delta,\ g \succ \delta$:

$$
\begin{aligned}
Q_{AB}(t) &= \frac{1}{16g^2}\left|\begin{matrix}\cos(\phi_0)\left(\cos(2g+\delta)t+\cos(\delta t)\right)\\ +i\sin(\phi_0)\left(\sin(2g+\delta)t+\sin\delta t\right)\end{matrix}\right|,\\
Q^2_{AB}(t) &= \left(\frac{1}{16g^2}\right)^2\left(\begin{matrix}\left(1+\cos 2gt\right)^2\left(\begin{matrix}\cos^2\delta t\cos^2(\phi_0)\\ +\sin^2\delta t\sin^2(\phi_0)\end{matrix}\right)\\ +\sin^2 2gt\left(\begin{matrix}\sin^2\delta t\cos^2(\phi_0)\\ +\cos^2\delta t\sin^2(\phi_0)\end{matrix}\right)\\ -2\left(1+\cos 2gt\right)\cos(2\phi_0)\times\\ \times\sin 2gt\cos\delta t\sin\delta t\end{matrix}\right).
\end{aligned}
\tag{19}
$$

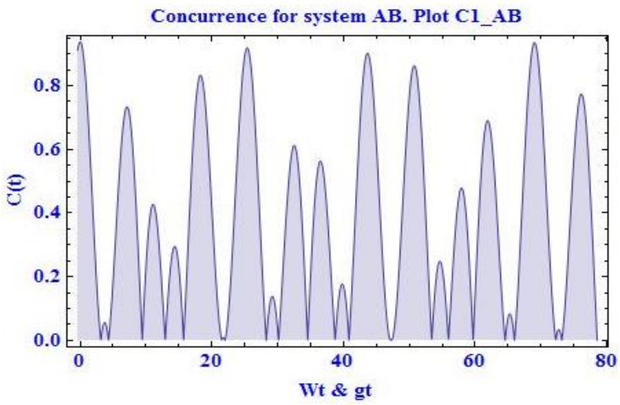

Fig. 2. Plot of the Concurrence for parameters: W=0.5; g=0.365; $\phi_0 = 0$. In this plot the oscillations fluctuate into of the time interval, almost become of top for entanglement of formation of one.

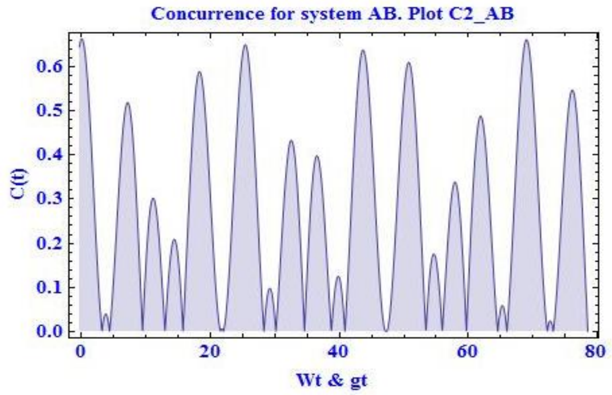

Fig. 3. Plot of the Concurrence for parameters: W=0.5; g=0.365; $\phi_0 = \pi/4$. In this case the plot decreases the amplitudes of the oscillations, because we do a change of $\pi/4$ to the phase.

Now we show the Concurrence plots in order to different parameters values, also in two, and three-dimensionally. The case 3D we consider the ϕ_0 as variable, which enables us visualize the contour zones of Sudden Death of concurrence.

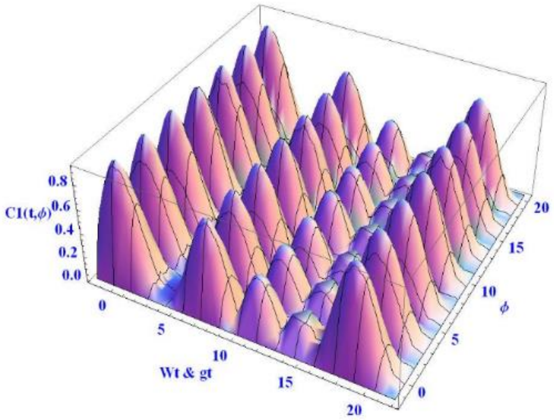

Fig. 4. Plot 3D for the Concurrence $C_{AB}(t, \Phi_0)$; for parameters: W=0.5; g=0.365.

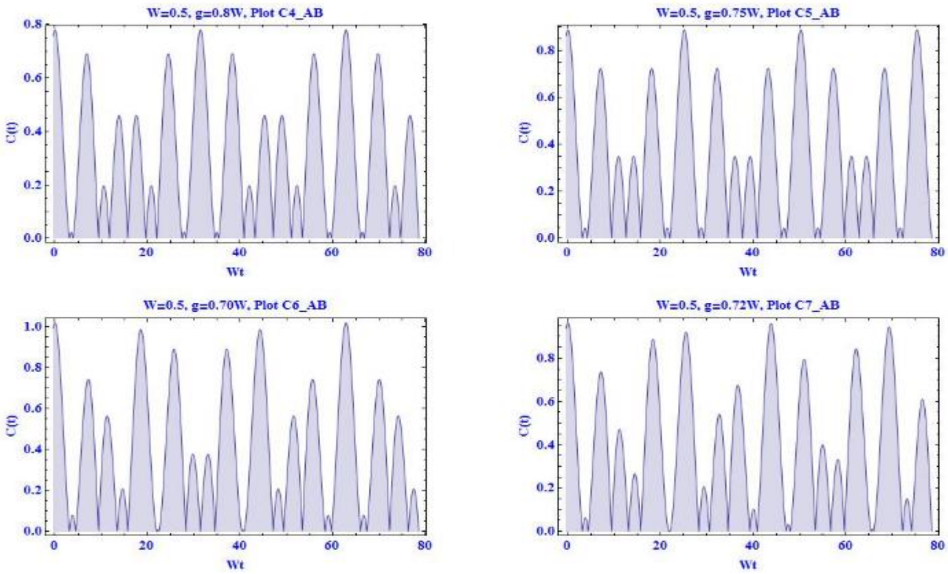

Fig. 5. Concurrence plots $C_{AB}(t)$; for parameters: W=0.5 and plot4 g=0.8W, plot5 g=0.75W, Plot6 g=0.70W, and plot7 g=0.72W. We can see that four combinations for constant g proportional to W. The more optimums combination is in order to plot5, and plot7. Plot6 slightly exceeds the allowable bound for Entanglement of formation and Concurrence of one. This is because the interaction constants differ by a percentage equal (or greater) to 30%, as is clearly noted in the data above.

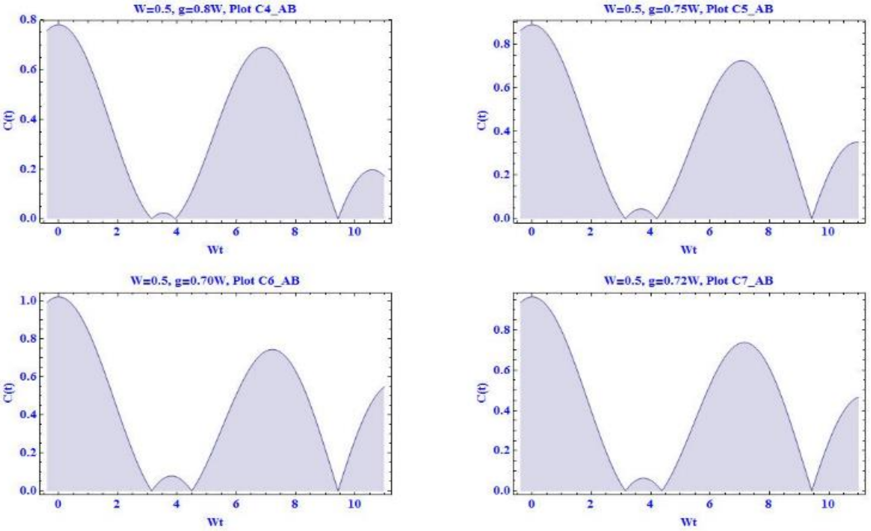

Fig. 6. Concurrence for the same parameters but plotted in a smaller domain, in order to show further details in the zones of minimum of the function $C_{AB}(t)$, the 3D case with (t,Φ_0) independent variables is showed in next figure 7. Parameters: W=0.5 and plot4 g=0.8W, plot5 g=0.75W, Plot6 g=0.70W, and plot7 g=0.72W.

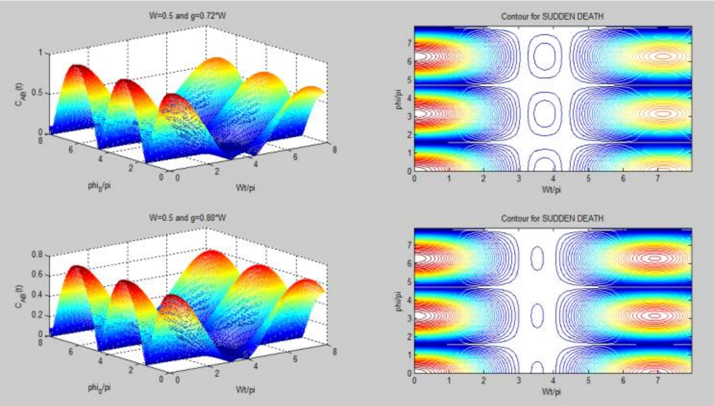

Fig. 7. Plots in 3D and Contours for so-called SUDDEN DEATH ZONES by $C_{AB}(t,\Phi_0)$; with two cases: W=0.5 and g=0.72W, g=0.80W and the parameter Φ_0 is variable, this is consequence of the initial state of Bell. We can see that contour zones of sudden death are minimums of the plots on the right. The interesting is to note that in this small zone rescaled for sake of simplicity that there is not a total sudden death as in the atomic case of the other authors [45-50]. What is also seen in previous plots from figures 2 to 6 into their minimum points.

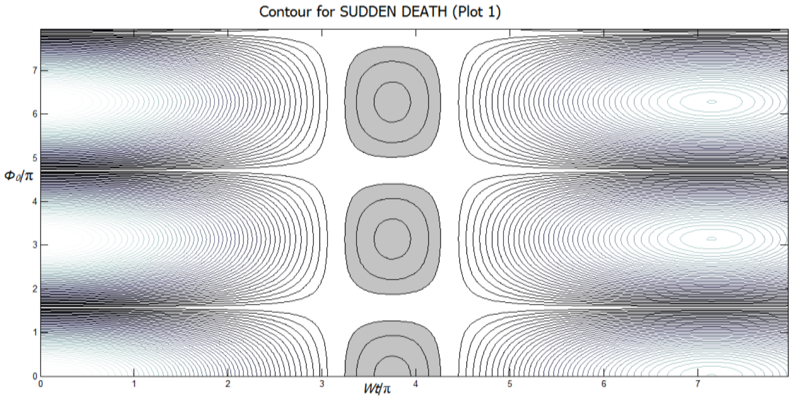

Fig. 8. Plots of Contours for so-called SUDDEN DEATH ZONES by $C_{AB}(t,\Phi_0)$; for the case: W=0.5 and g=0.72W, and the parameter Φ_0 is variable, this is consequence of the initial state of Bell. We can see the contour zones for sudden death that are minimums on the plots in gray color, but without become null totally.

6 Conclusions

In this paper we study the dynamics behavior of a system of two QDs embedded into own cavity, previously entangled, with initial state type Bell into of the context CQED and Förster interaction included into QDs Hamiltonian. This behavior let us insight the particular dynamics of transference and quantum communication correlations between two qubits, in this case represent for our two QDs, i.e. how is the entanglement process after that qubits are entangled and input into cavity in this situation of communication to distance without interaction, i.e. how evolve this entanglement with the time and consider the initial state of type Bell, which include the Φ_0 parameter. The way in order to understand and quantify this process without ambiguity is obtain a secure measure of the entanglement. This measure is the *Concurrence and Entanglement of Formation* for two qubits (Hill and Wootters 1997; Wootters, 1998) only. The measure is defined only for two qubits as entities of two states, because there is not an extension of this method to more qubits that to allow calculate with precision their entanglement.

Our results between the two cavity-QD, let us see that the entanglement depend of both parameters of interaction, i.e. the interaction field-QDs (*g*) and the Förster interaction (*W*). Both interactions must be of the same order, because if either of the two differs significantly from another the result found is that oscillations slightly exceed the bound of the one for entanglement of formation. In this way we find that the interaction parameters must be very well controlled and should not be very different in order of magnitude. Also the best way to control them is by making one of the two in terms of another one by a minimum percentage, as we can see in figures 5, 6 and 7. Another one very important is the so-called *Sudden Death* feature where we analyzed in multiples plots in figures 5 and 6, but with greater accurately in contour plots 7 and 8, how the *Sudden Death* zones are *minimums*, however there is not totally sudden death of entanglement as happen in the cases study for systems of atoms for other authors (Yu, Yonac and Eberly 2002-2007) or the case for QDs studied in references: (Quiroga-Jhonson 1999; Reina-Quiroga-Jhonson 2000; Mitra, Vyas Erenso 2007), in these papers the authors do not even mentioned the case of Sudden Death as in atomic situation. We can say that for these QDs system almost there is not sudden death because minimum zones are very sharp, i.e. they are smooth curves cosine in which do not we get semi-flat zones, that in atomic case is where entanglement sudden death occurs.

This allows us conclude that our QDs system featuring to two qubits is more efficient for propagation of entanglement without loss of quantum correlation.

Acknowledgment. The author S. Sánchez-Sánchez wants to acknowledge the organization of the international workshop LAOP 2014 held in Cancun, Mexico for the invitation and scholarship for the event. Also, authors S. Sánchez-Sánchez, V. I. Moreno Oliva, and E. Román Hernández acknowledge PROMEP (Programa de mejoramiento para el profesorado de la Secretaria de Educación Pública) by grant support UNISTMO-CA-13 projects in 2013-09 to 2014-09.

References

1. Bennett, C. H., Brassard, G., Crepeau, C., Jozsa, R., Peres, A., Wootters, W. K.: Phys. Rev. Lett. 70, pp. 1895 (1993)
2. Bennett, C. H., Wiesner, S. J.: Phys. Rev. Lett. 69, pp. 2881 (1992)
3. Bennett, C. H., DiVincenzo, D. P., Smolin, J. A., Wootters, W. K.: Phys. Rev. A 54 pp. 3824 (1996)
4. Bennett, C. H., Bernstein, H. J., Popescu, S., Schumacher, B.: Phys. Rev. A 53, pp. 2046 (1996)
5. Bennett, C. H., Brassard, G., Popescu, S., Schumacher, B., Smolin, J., Wootters, W. K.: Phys.Rev. Lett. 76, pp. 722 (1996)
6. DiVincenzo, D. P.: Science. 270, pp. 255 (1995)
7. Deutsch, D.: Quantum theory, the Church-Turing principle and the universal quantum computer. In: Proc. R. Soc., London, A 400, pp. 97–117 (1985)
8. Deutsch, D: Quantum computational networks. In: Proc. R. Soc., London, A 439, pp. 553–558 (1989)
9. Feynman, R. P.: Quantum mechanical computers. Optics News, 11, pp. 11–20 (1985)
10. Fuchs, C. A., Gisin, N., Griffiths, R. B., Niu, C. S., Peres, A.: Phys. Rev. A 56, pp. 1163 (1997)
11. Hill, S., Wootters, W. K.: Phys. Rev. Lett. 78, pp. 5022 (1997)
12. Joos, E, Zeh, H. D, Kiefer, C, Giulini, D, Kupsch, K., Stamatescu, I. O.: Decoherence and the Appearance of a Classical World in Quantum Theory. Germany: Springer (2003)
13. Kane, B. E., Loss, D., DiVincenzo, D. P.: Phys. Rev. A 57, pp. 120 (1998)
14. Burkard, D., Loss, D., DiVincenzo, D. P.: Phys. Rev. B 59, pp. 2070 (1999)
15. Barenco, A., Deutsch, D., Ekert, A., Jozsa, R.: Phys. Rev. Lett. 74, pp. 4083 (1995)
16. Imamoglu, A., Awschalom, D. D., Burkard, G., DiVincenzo, D. P., Loss, D., Sherwin, M., Small, A., Mitra, A., Vyas, R., Erenso, D., Phys. Rev. A 76 (2007)
17. Nielsen, M. A., Chuang, I. L.: Quantum Computation and Quantum Information. CambridgeUniversity Press, Cambridge, England (2000)
18. Quiroga, L., Johnson, N. F.: Phys. Rev. Lett. 83, pp. 2270 (1999)
19. Reina, J. H., Quiroga, L., Johnson, N. F.: Phys. Rev. A. 62 (2000)

20. Sanchez-Sanchez, S.: Dynamic behavior of collective and reduced Quantum dots system. Instituto Nacional de Astrofísica Óptica y Electrónica (INAOE), PhDr. Thesis, Tonantzintla, Puebla, Mexico (2011)
21. Sanchez-Mondragon, J. J., Alejo-Molina, A., Sanchez-Sanchez, S., Torres-Cisneros, M.: Comparison of the Dicke Model and the Hamiltonianfor n Quantum Dots, Quantum Dots, Nanoparticles, and Nanoclusters II. In: Proceedings of SPIE, Vol. 5734 (2005)
22. Alejo-Molina, A., Sánchez-Mondragón, J. J., Sánchez-Sánchez, S.: Detuning Colectivo Del Modelo De L Puntos Cuánticos. XLVIII Congreso Nacional Smf / Xviii Reunion Anual Amo Guadalajara Jalisco (2005)
23. Sánchez-Sánchez, S., Sánchez-Mondragón, J. J., Castillo-Soria, F. R.: Representación de Puntos Cuánticos en la Base Atómica Coherente. Memorias en extenso del LII Congreso Nacional de Física (SMF)/ Reunión Anual de Óptica (AMO), Acapulco Guerrero (2009)
24. Werner, R. F.: Phys. Rev. A 40, pp. 4277 (1989)
25. Peres, A.: Phys. Rev. Lett. 77, pp. 1413 (1996)
26. Wootters, W. K.: Phys. Rev. Lett. 80, pp. 2245 (1998Yönac M, Yu T and Eberly J H, J. Phys. B: At. Mol. Opt. Phys. 39, S621–S625 (2006)
27. Yönac, M., Yu, T., Eberly, J H.: J. Phys. B: At. Mol. Opt. Phys. 40, pp. S45–S59 (2007)
28. Yu, T., Eberly, J. H.: Phys. Rev. Lett. 93 (2004)
29. Yu, T., Eberly, J. H.: Opt. Commum. at press Preprint quant-ph/0602196 (2006)
30. Yu, T., Eberly, J. H.: 2002 Phys. Rev. B 66 193306;
31. Yu, T., Eberly, J. H.: Quantum Inf. Comp. 7 in press, Preprint quant-ph/0503089 (2007)

ISSN 1870-4069

Vector Theory for the Scattering of TM-polarized Hermite-Gaussian Electromagnetic Beams by a Double Metallic Slit

R. Salazar-Hernández, G. Montiel-González, J. Mulia-Rodríguez,
J. Sumaya-Martinez

Facultad de Ciencias, Universidad Autónoma del Estado de Mexico, Toluca, Mexico

jsm@uaemex.mx

Abstract. We present a rigorous theory for oblique incident Hermite-Gaussian beams, diffracted by two slits of width ℓ and separation d, in a thick metallic screen for the case of polarization TM(S). The far field spectra as a function of several opto-geometrical parameters, wavelength λ, slit width ℓ, separation d, incidence angle θ_i and Hermite order m is analyzed. In the vectorial diffraction region given when $\lambda/\ell > 0.2$, where ℓ is the incident wavelength and as a function of the separation between slits d; we have numerically analyzed: the far field spectra, the energy diffracted along the incident beam direction (E_i), and the validity of an approximate diffraction (scalar) property, namely $E_i = N\tau/\lambda$.

Keywords: diffraction, scattering, double slit.

1 Introduction

Currently there are several rigorous theories of diffraction by plane electromagnetic waves (Enriquez *et al.*, 2011) and Gaussian beams (Mata *et al*, 1993); (Mata *et al*, 1994) by two slits in metallic screens of zero thickness. However these theories do not treat with Hermite-Gauss or oblique incidence, nor thick screens of nonzero thickness (Mata *et al*, 2008).

In this paper we present a novel rigorous theory of diffraction that allows to consider the illumination by Hermite-Gaussian beams at oblique incidence on two slits of width ℓ and separation d in screens with infinite conductivity and thickness h.

In particular, we analyze the coupling between slits through the numerical study of the diffracted energy along the direction of the incident (E_i) beam energy as a function of the parameter of separation d between the slits. It is revealed the existence of oscillations in the energy E_i . We also show that in the case of TM(S) polarization, the energy E_i is special because when compared to other diffraction patterns. Finally, we show that the scalar property valid at the scalar region (λ/ℓ <0.2) $E_i = N\tau/\lambda$ (Alvarez-Cabanillas, 1995) is not longer valid.

2 A Vector Theory of Diffraction

In Fig.1 we have two slits on a screen of infinite conductivity, and non-zero thickness denoted by h. In this screen you have two parallel to the Oz axis, ℓ wide and spaced slits d. The display is in the gap and impinges perpendicularly on it a Hermite-Gaussian beam with wavelength $\lambda = 2\pi/k$ and order m. We will use the complex representation for the fields and omit the time factor going forward $e^{-i\omega t}$. H is the magnetic field when you have the TM (magnetic field parallel to the axis Oz) polarization. The H field satisfies the Helmholtz equation (Mata *et al*, 1994)

$$\partial^2 \mathrm{H}/\partial \mathrm{x}^2 + \partial^2 \mathrm{H}/\partial \mathrm{y}^2 + \mathrm{k}^2 \mathrm{H} = 0. \tag{1}$$

Denote by H_I the solution of Eq (1) in the region I ($y > h/2$), expressed by a plane wave expansion:

$$\mathrm{H_I}(\mathrm{x},\mathrm{y}) = \frac{1}{\sqrt{2\pi}} \int_{-\mathrm{k}}^{\mathrm{k}} \mathrm{A}(\alpha)\, \mathrm{e}^{\mathrm{i}(\alpha \mathrm{x} - \beta \mathrm{y})} d\alpha + \frac{1}{\sqrt{2\pi}} \int_{-\mathrm{k}}^{\mathrm{k}} \mathrm{B}(\alpha)\, \mathrm{e}^{\mathrm{i}(\alpha \mathrm{x} + \beta \mathrm{y})} d\alpha. \tag{2}$$

The first integral is identified with the incident beam due to the sign of the α and β k-components.

In region II, within the screen, $-h/2 < y < h/2$ the electromagnetic field will be represented by the following modal series:

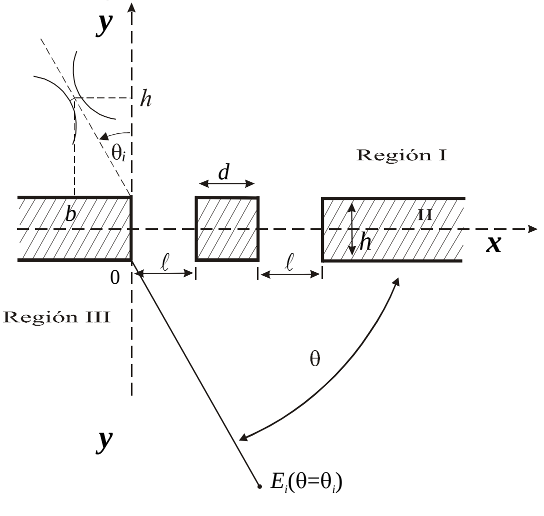

Fig. 1. Our system. Two slits of width ℓ and spacing d in an infinitely thick conducting screen h. The energy diffracted along the incident direction (E_i) is diffracted in the direction of θ(relative to the axis Oy) = θ_i (From the axis Ox).

$$H_{II}(x,y) = \sum_{n=0}^{\infty} a_n^1 \varphi_n^1(x,y) + \sum_{n=0}^{\infty} a_n^2\, \varphi_n^2(x,y), \tag{3}$$

where in $i = 1{,}2$ the set $\varphi_n^i(x)$, are functions whose normal derivative is zero at the walls for the TM polarization.

The diffracted field below the screen, for $y < -h/2$ (region III), could be expressed as a plane wave expansion too:

$$H_{III}(x,y) = \frac{1}{\sqrt{2\pi}} \int_{-\infty}^{\infty} C(\alpha)\, e^{i(\alpha x + \beta y)} d\alpha. \tag{4}$$

Our goal is to determine the transmitted field (Eq. (4)), for which one needs to determine $C\,(\alpha)$. Note that $C\,(\alpha)$ depends on the coefficients a_n^1 and a_n^2 and the incident amplitude $A(\alpha)$. For this, we use the appropriate conditions of continuity, which could be obtained from Maxwell's equations (Alvarez-Cabanillas, 1995). These conditions lead us to the following matrix system, in which the matrix columns $\boldsymbol{a_1}$ and $\boldsymbol{a_2}$ are formed respectively by the coefficient a_n^1 and a_n^2.

$$\begin{aligned} M_{11}a_1 + M_{12}a_2 &= S_1, \\ M_{21}a_1 + M_{22}a_2 &= S_2, \end{aligned} \tag{5}$$

where M_{ik} $(i,k = 1{,}2)$ are square matrices dependent on the opto-geometrical parameters and S_i $(i = 1{,}2)$ are matrices depending only on $A\,(\alpha)$. The determination of the modal coefficients a_n^1 and a_n^2. allow us to calculate the diffracted field in any region for TM polarization.

3 Results and Discussion

Using the complex Poynting vector is possible to obtain the diffracted intensity at the angle θ. For a Hermite-Gaussian beam, the spectral amplitude is (Mata *et al*, 2008):

$$A(\alpha) = \frac{L}{2} i^m H_m \left[-\frac{L}{2}(\alpha \sin\theta_i - \beta\cos\theta_i)\right] \times \left[\sin\theta_i + \left(\frac{\alpha}{\beta}\right)\cos\theta_i\right] e^{(-i\alpha b)} \times e^{\left[-(\alpha\sin\theta_i - \beta\cos\theta_i)^2 L^2/8\right]}, \tag{6}$$

where H_m is the Hermite polynomial of order m. The position of the beam waist is given by the parameter b (see Fig. 1).

In the figures relating to energy diffracted along the direction of the incident beam is $E_i(\theta = \theta_i)$ the diffracted angle in the direction of the incident beam, measured from the axis Ox and θ_i is the angle of incident beams to the axis Oy measured. The energy, the diffracted intensity $I(\theta)$ and the transmission coefficient τ are normalized to the total incident energy I_0. All parameters normalized opto-geometrical width lof the slots ℓ, that is, , ℓ= 1.

In Figs. 2 and 3 show the diffraction patterns of Hermite-Gaussian beams for the fundamental mode $m = 0$ at normal incidence and oblique incidence of 30 °; the wavelength of the incident beams is λ/ℓ=0.9, with extremely wide Gaussian beams L/$\ell= 500/\sqrt{2}$ and fixed at the position b/ℓ=0.5, the thickness of the screen is h/ℓ =1and the gaps between slits are d/ℓ= 0, 1, 3.5 and 5.

The shape of the diffraction patterns for the $m = 2$ mode, not shown, is identical to the spectra of FIGS. 2 and 3 (with the same opto-geometrical parameters) except for a scaling factor which provides a lower intensity for this mode, from the respective Hermite polynomial.

From these diffraction patterns we have taken the diffracted energy E_i along the direction of the incident beams. Figs. 4 and 5 show the behavior of the E_i separation according to d for $m = 0$ and 2 modes; opto-geometrical parameters of these figures are the same in Fig. 2 and 3.

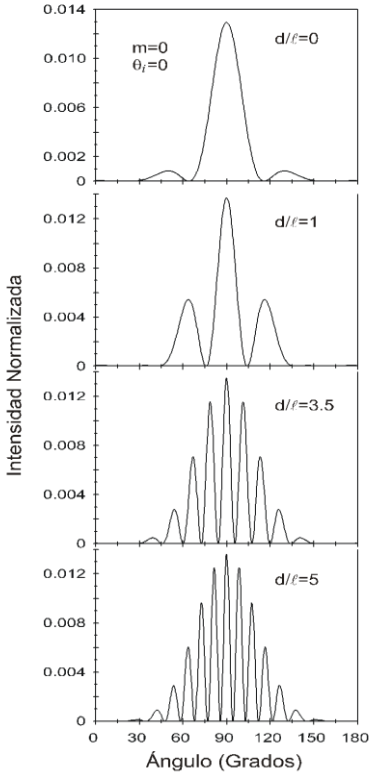

Fig. 2. Diffraction patterns normalized $(I(\theta)/I_0)$ of Hermite-Gaussian beams of $m = 0$ normally incident on two slits so. With λ/ℓ = 0.9, L/ℓ=500/$\sqrt{2}$, h/ℓ =1 and position b/ℓ=0.5 and for separations d/ℓ = 0, 1, 3.5 and 5.

The curves of FIGS. 4 and 5 show the oscillatory behaviors as E_i a function of the spacing d, in particular for the period is normal incidence to oblique incidence λ and the period is 2λ.

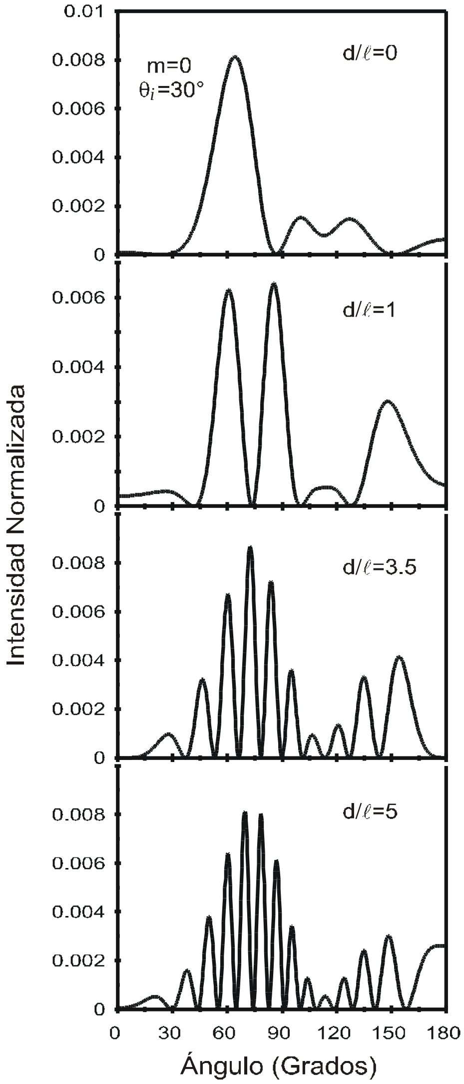

Fig. 3. Standard diffraction patterns $(I(\theta)/I_0)$ Hermite-Gaussian beam for $m = 0$ to $30\,°$ obliquely incident on two slits so. Same parameters of Fig.2.

In Fig. 5 has also been drawn in broken lines the 2τ/λ function. As you can see, this function does not overlap with the energy with E_i which we can say that the property of diffraction E_i =2τ/λ is not valid in the vector region at least for the separation parameter d and doing extremely wide.

Finally, in Fig. 6 different diffracted energy around the energy is E_i. The upper curves of Figure 6 correspond to normal incidence for the $m = 2$ mode, with the same parameters of Fig. 3; diffracted energies correspond to the angles diffracted $\theta = 90°, 91°, 92°\ and\ 94°$. The curves in the lower window of Fig. 6 correspond to oblique incidence of 30°, also for mode $m = 2$, with the same parameters of Fig. 4. The diffracted energies shown, corresponding to angles diffracted around of $\theta = 60$ ° (corresponding to the diffracted energy along the oblique incidence angle $\theta_i = 30$ °) and for the angles 58 °, 57 ° and 64 °.

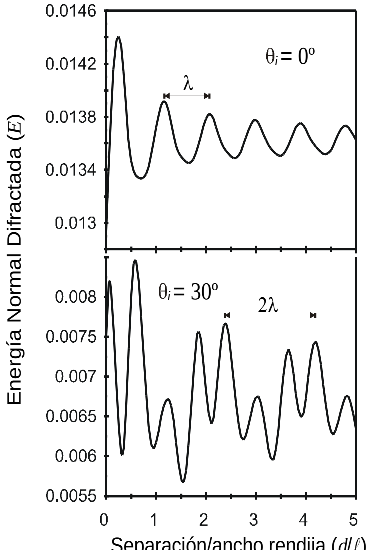

Fig. 4. Energy diffracted in the direction normal to the standard E_i to Hermite-Gauss beam, depending on the spacing d/ℓ screen. For the fundamental mode $m = 0$, at normal incidence and oblique incidence of 30°, with λ/ℓ=0.9, L/ℓ=500/$\sqrt{2}$, h/ℓ =1, y b/ℓ=0.5.

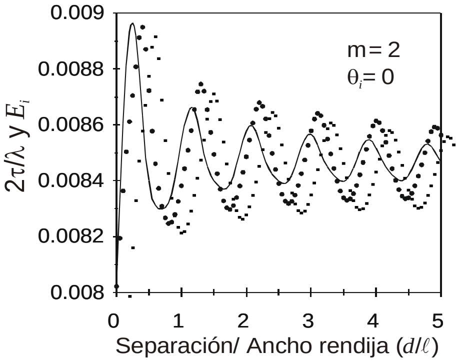

Fig. 5. Energy diffracted in the direction normal to the E_i (solid line) Hermite-Gauss beam, thus $m = 2$ and $2\tau/\lambda$ property (dashed line), in function of the spacing d/ℓ. Same parameters of Fig. 3.

Energy analyzing energy diffracted E_i around for $m = 0$ at normal incidence and oblique incidence of 30 ° as also carried out (data not shown) found similar patterns for mode $m = 2$ (see Fig. 6), the energy diffracted around the energy as E_i a function of the spacing d, decay to zero.

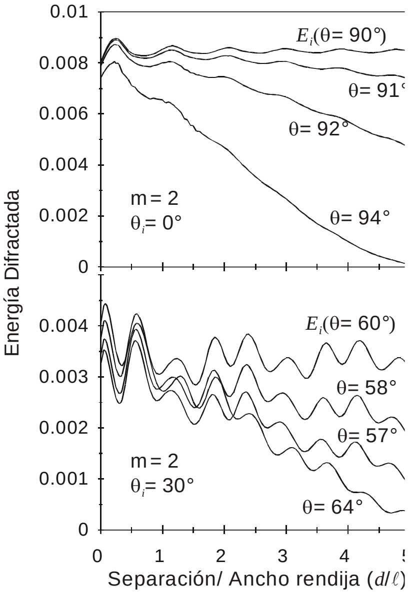

Fig. 6. Energy diffracted around energy $E_i(\theta = \theta i)$ Hermite-Gauss beam, for the $m = 2$ mode according to the distance between slits d/ℓ. Same parameters of Fig. 4.

4 Conclusions

Present a more rigorous theory of diffraction for the oblique incidence beam Hermite-Gaussian (HG) on a screen of thickness h with wide slits separating slits ℓ and d. In the case of TM(S) polarization and wavelengths in the vector region $\frac{\lambda}{\ell} > 0.2$, we have found that the diffracted along the direction of the incident beam energy has oscillations period λ as a function of the spacing d for modes $m = 0$ and 2, for the period 2λ at 30 ° oblique incidence. Finally, we note that the energy E_i has special characteristics compared diffracted energies in other directions and found numerically that ownership of scalar diffraction $(\lambda/\ell < 0.2)$ given by $E_i = 2\tau/\lambda$ is no longer valid in this region $(\lambda/\ell > 0.2)$.

References

1. Enriquez-Leon, G., Martinez-Flores, M. G., Torres-Morales, G., Sumaya-Martinez, J.: Rigorous diffraction of Hermite-Gaussian beams by a double slit. TM polarization. Eight Symposium Optics in Industry (2011)

2. Mata-Méndez, O., Chávez-Rivas, F.: Estudio teórico y numérico de la difracción en óptica electromagnética, II Teoría rigurosa de la difracción de un haz gaussiano por dos rendijas, Polarización TE. Revista Mexicana de Física, 39(5), pp. 706–721 (1993)
3. Mata-Méndez, O., Álvarez-Cabanillas, M. A.: Estudio teórico y numérico de la difracción en óptica electromagnética, III Teoría rigurosa de la difracción de un haz gaussiano por dos rendijas, Polarización TM. Revista Mexicana de Física, 40(6), pp. 846–856 (1994)
4. Mata-Méndez, O., Chávez-Rivas, F., Ortiz-Acebedo, A.: Diffraction of hermite–gaussian beams by Ronchi and aperiodic rulings. Revista Mexicana de Física, 54(1), pp. 35–4 (2008)
5. Álvarez-Cabanillas, M. A.: Tratamiento riguroso para la difracción de un haz Hermite-Gauss a través de N-rendijas. ESFM-IPN, Tesis Doctoral (1995)

ISSN 1870-4069

Radiant Flux Analysis of a System based in Imaging Fresnel Lens and Plastic Optical Fiber with Fiber Lenses

Perla M. Viera-González, G. E. Sánchez-Guerrero, D. E. Ceballos-Herrera,
R. Selvas-Aguilar

Centro de Investigación en Ciencias Físico Matemáticas,
Universidad Autónoma de Nuevo León, Nuevo León, México

marlene.viera.gzz@gmail.com

Abstract. Imaging Fresnel has been extensively studied to focus light in an effective and low-cost way; however, these lenses show low tolerances in alignment when they are coupled with plastic optical fibers (POFs). The principal factor is the high focal point movements produced by slight changes in the incidence angle of the source rays. In order to study these movements and its effects over the coupling between Fresnel lens and POFs, a mathematical analysis using Geometrical Optics and simulations in Zemax OpticStudio® were performed. The results show that the asymmetry of the numeric aperture of the Fresnel lens has higher sensitivity to low incidence angles and the coupling of the focused light to POFs with different fiber lenses at the input have a better performance using a plane face end. The results confirm the low tolerance, <1º, to source angular misalignments and suggest the use of a secondary optical element.

Keywords: Imaging Fresnel lens; fiber lenses; plastic optical fiber; radiometry; geometrical optics.

1 Introduction

Since its invention in 1822 by Augustin Fresnel, the Fresnel lenses have been used with different purposes as lighthouses, imaging systems and light concentration; indeed, focus light, in particular Solar light, using Fresnel lens is an effective way to make full use of sunlight (Leutz & Suzuki, 2001; Xie, Dai, Wang, & Sumathy, 2011).

Indoor illumination by sunlight concentration with Fresnel lenses is one of the uses of imaging Fresnel lenses which has grown its implementation due to the importance of reduce the energy consumption in modern societies (Xie et al., 2011).

Imaging Fresnel lenses offer flexibility in optical design thanks to its high manufacture error tolerance, light-weight, small volume and low cost in contrast with conventional lenses; but the Imaging Fresnel lenses are prone to focal point movements due to changes in the incidence angle of the source rays, this leads, in the case of sunlight collection, to the need of high-precision Solar tracking for focal foreshortening and longitudinal focal movements (Leutz & Suzuki, 2001).

This work shows a mathematical analysis of the variations presented in the focal point position when the source rays arrive parallel between them but form an angle from the optical axis. Considering the afore mentioned analysis, a numeric analysis for compute the changes produced in the output power in a system composed by an Imaging Fresnel lens and a Plastic Optical Fiber (POF) with different fiber lenses in its input was performed, the light source has parallel rays arriving with angles from 0° to 4° from the system optical axis.

2 Materials and Methods

The Fresnel lens are essentially chains of prisms and can be studied using Geometrical Optics considering the phenomena of reflection and refraction in each prism (Leutz & Suzuki, 2001).

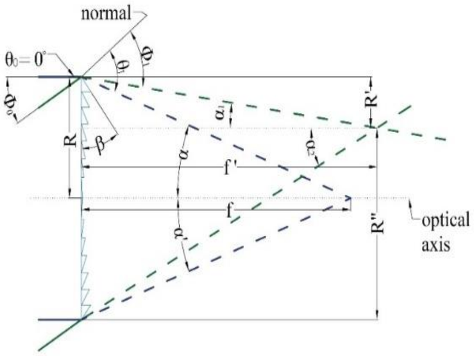

Fig. 1. Imaging Fresnel lens with grooves facing inward and source rays arriving parallel to optical axis, θ_0, and other arriving with an angle ϕ_0. The marginal rays for the 2 inputs generate 2 different output cones delimited by the marginal rays in each case.

For the coupling analysis between the Imaging Fresnel lens and the POF it is necessary know the output generated by a Fresnel lens. According to this, Snell's law was used (Leutz & Suzuki, 2001):

$$n \, sin \, \theta = n' \, sin \, \theta'. \tag{1}$$

And the relations for the angles α and β, which are (Leutz & Suzuki, 2001):

$$\alpha = tan^{-1} {}^{R}\!/_{f} = \theta_{output} - \beta, \tag{2}$$

$$\beta = tan^{-1}\left(\frac{R}{n'\sqrt{R^2+f^2} - f}\right). \tag{3}$$

Where the angle α is the semi-angle of the output cone, β is the angle of the prism, R is the radial length of the Fresnel lens, f its focal length, n' represents the refractive index of the Fresnel material and θ_{output} is the angle of the marginal ray with the normal of the prism (Figure 1). The equation for the β angle is only valid for Fresnel lens with grooves facing inward (Leutz & Suzuki, 2001).

With the aforementioned equations and applying the Snell's law in every interface in the marginal prism, the relation between the radial length and the focal length, when the source rays arrive with an angle $\theta_0=0°$ and the output ray has a marginal ray with an angle θ1, can be expressed as follow:

$$^{R}/_{f} = tan(\theta_1 - \beta) = tan[sin^{-1}(n' \sin\beta) - \beta]. \tag{4}$$

For this case, the output cone is radially symmetric with the optical axis:

$$\alpha = \alpha'. \tag{5}$$

Now, for the case when the source rays arrive with an angle ϕ_0 from the optical axis and considering β as a constant physical parameter of the marginal prism, the relation between R' and f', shown in Figure 1, is defined as:

$$\frac{R'}{f'} = tan\left[-\beta + sin^{-1}\left(n' \, sin\left[\beta - sin^{-1}\left(\frac{sin\,\phi_0}{n'}\right)\right]\right)\right] = tan\,\alpha_1. \tag{6}$$

And, as this case is not radially symmetrical, $\alpha_1 \neq \alpha_2$ the relation between R'' and f', shown in Figure 1, is:

$$\frac{R''}{f'} = tan\left[-\beta + sin^{-1}\left(n' \, sin\left[\beta + sin^{-1}\left(\frac{sin\,\phi_0}{n'}\right)\right]\right)\right] = tan\,\alpha_2. \tag{7}$$

For a quantitative analysis of the equations obtained, a Fresnel lens with a radius of 14.29 cm, a focal length of 16.51 cm and a refractive index of 1.491 was considered. This lens was used to see the differences angles, α_1 and α_2, generated by the tilt angle in the incidence light source, considering angles $\phi_0 = 0.0°: 5.0°$ with steps of 0.1°. The results of this analysis are shown in the next section (Figure 4) and present the lineal increase of the asymmetry in the output cone of the Fresnel lens.

A conventional POF, which has a Polymethyl methacrylate core ($n = 1.491$) and with a fluorinated polymer cladding ($n = 1.418$), has an acceptance semi-angle $\sim 27.23°$, which represents a Fresnel lens as the one used for the above analysis will not be able to couple with a POF, for this reason it is necessary look for alternative ways to increase the coupling between the Fresnel lens and the POF.

Considering the acceptance angle of a POF can be modified using fiber lenses (Bescherer, Munzke, Reich, & Loock, 2013), Zemax OpticStudio® was used to simulate an optical system composed by a D65 light source, a Fresnel lens and 10 cm of POF (Figure 2).

Different input shapes were analyzed at the input POF, being the 4 fiber lenses shown in Figure 3 the shapes with the best results. The parameters for the fiber lenses were taken from (Viera-González et al., 2013).

During the simulations the radiant flux was measured tilting the light source from 0° to 5°, in steps of 0.1°, for every fiber lens; the output power and coupling was analyzed. The output of a POF with planar input when the incidence angle of the source rays is 0° was taken as the base output power (100%).

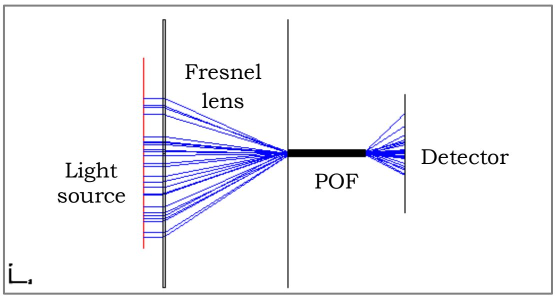

Fig. 2. Optical system design in Zemax OpticStudio®: the Fresnel lens has an output semi-angle of 40.87˚, the POF has an acceptance semi-angle of 27.23˚.

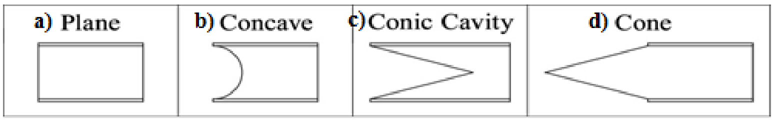

Fig. 3. Fiber lenses. a) Conventional POF with planar input. b) POF with concave fiber lens, the curvature corresponds to a parabolic surface with curvature radius of 10. c) POF with a conic cavity in the input, the aperture semi-angle of the cone is 17°. d) Fiber lens with conic form, the semi-angle of the cone is the same as the one of the conic cavity.

3 Results

The Figure 4 shows the results of the mathematical analysis, where $\Delta\alpha = |\alpha_1 - \alpha_2|$, where is proved the focal movements due to angular misalignment between light source and Fresnel lens; these changes in the focal length also reflect a change in the output cone, breaking the symmetry presented in the case when the light arrives totally perpendicular to the Fresnel lens.

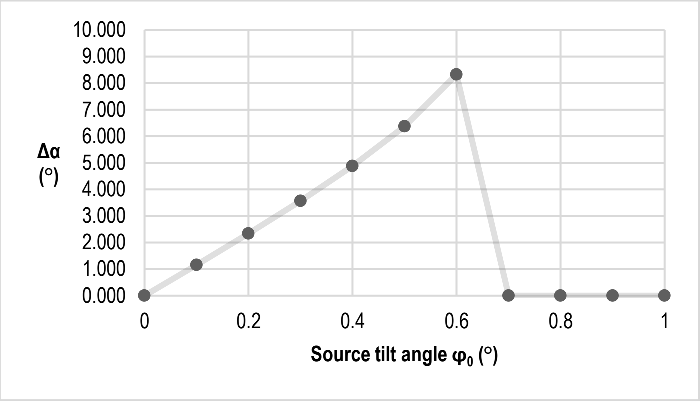

Fig. 4. The graph shows a lineal growth of the asymmetry in the output cone in the range between $\phi_0 = 0.1°: 0.6°$, out of this range it is not possible determine te output angle in one of the marginal prisms, because for this cases the total internal reflection is presented.

For the particular case of the Fresnel lens used for the mathematical analysis, when the incidence angle of the light is higher than $\phi_0 = 0.6°$, the marginal prisms presents total internal reflection that generated losses.

The results of the simulation mentioned in the last section are summarized in Fig. 5, this graph shows the decrement of the system efficiency for the angular misalignment between the light source and the Fresnel lens.

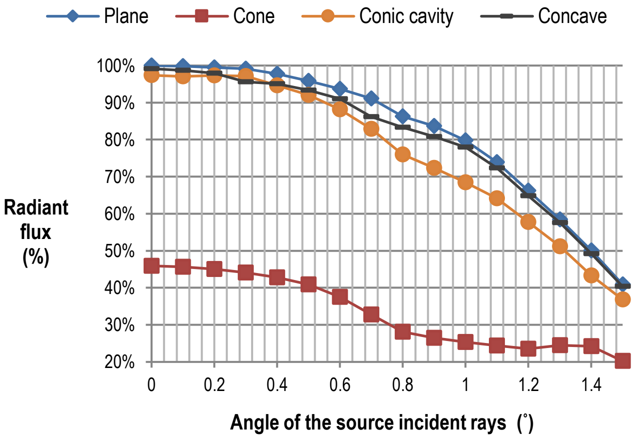

Fig. 5. Plane and concave FOP faces have better performance. The plane, concave and conic cavity fiber lenses show similar performance and have, in the theoretical critical tilt of the Fresnel lens (0.7˚), efficiency around 80-90%.

4 Discussion

The mathematical analysis made for the asymmetry generated by angular misalignments between the light source and the Fresnel lens shows low tolerance ($<$ 1°), because the asymmetry is increased; also, with the mathematical relations found it is possible calculate the changes produced in the focus position. This low tolerance represents a problem for applications with sources in movement, as solar illumination systems.

The results obtained in (Viera-González et al., 2013) could not be applied in fiber inputs to increase the angular coupling between POF and Fresnel lens; then, for achieve a higher coupling, without use tracking systems, will be necessary the use of a secondary optical element for reduce the angle of the light that arrives to the POF and, at the same time, generate a uniform and radially symmetrical spot which couples with the fiber.

Acknowledgments. The presented research was made thanks to the support of the Facultad de Ciencias Físico Matemáticas, the Academic Group ‘Photonics and Telecommunications’ and the Consejo Nacional de Ciencia y Tecnología (CONACyT) through the scholarship 338144.

References

1. Bescherer, K., Munzke, D., Reich, O., Loock, H. P.: Fabrication and modeling of multimode fiber lenses. Applied Optics, 52(4), pp. 5–40 (2013)
2. Leutz, R., Suzuki, A.: Nonimaging Fresnel Lenses. Vol. 83, Berlin, Heidelberg: Springer Berlin Heidelberg (2001)
3. Viera-González, P., Sánchez-Guerrero, G., Cárdenas-Ortíz, G., Guzmán-Ramos, V., Castillo-Guzmán, A., Peñalver-Vidal, D., Selvas-Aguilar, R.: Design and optimization of fiber lenses in plastic optical fibers for indoor illumination. In: R. Winston & J. Gordon (Eds.), Proc. SPIE, Vol. 8834, pp. 88340 (2013)
4. Xie, W. T., Dai, Y. J., Wang, R. Z., Sumathy, K.: Concentrated solar energy applications using Fresnel lenses: A review. Renewable and Sustainable Energy Reviews, 15(6), pp. 2588–2606 (2011)

ISSN 1870-4069

Procesamiento digital de imágenes con LabVIEW: Aplicaciones en sistemas biológicos y nanomateriales

T. Córdova-Fraga[1], J.A. Álvarez-Gutiérrez[2], J.F. Gómez-Aguilar[3],
R. Guzmán-Cabrera[4], J.C. Martínez-Espinosa[5], C.R. Contreras-Gaytán[2],
J.J. Bernal-Alvarado[1], M.A. Vallejo-Hernández[1]

[1] Universidad de Guanajuato, Campus León,
Depto. de Ingeniería Física , León, Guanajuato,
México

[2] Universidad de la Salle Bajío,
Facultad de Ingeniería en Computación y Electrónica, León Guanajuato,
México.

[3] CONACyT, Cuernavaca, Morelos,
México.

[4] Universidad de Guanajuato Campus, Irapuato-Salamanca,
Depto. de Ingeniería Eléctrica, Guanajuato,
México

[5] Instituto Politécnico Nacional-UPIIG, Guanajuato,
México.

{teo, jfga, bernal}@dci.ugto.mx, ing.juan.antonio.alvarez@outlook.com,
jgomez@cenidet.edu.mx, guzmanc81@gmail.com, jcmartineze@ipn.mx

Resumen. Las imágenes se han utilizado desde hace varias décadas como una herramienta para la identificación o cuantificación de ciertas propiedades físicas. En el campo de la medicina se han aplicado para la identificación de malformaciones, tumores, fracturas, entre otras. Los algoritmos implementados en este trabajo son, apertura y corte de sección de imagen, operadores de filtrado y cuantificación de pixeles. Se usan para crear una aplicación virtual en el entorno de programación LabVIEW (LV) como un modelo de utilidad que aplica diferentes algoritmos para medir, cuantificar y determinar las diferencias de cambios y formas en las imágenes que se tomaron a través de un microscopio utilizando tres amplificaciones diferentes. En esta aplicación se trabaja con imágenes de células obtenidas del fémur de un animal y la cuantificación de la distribución de tamaños de nanomateriales mediante la medición individual de las áreas de cada célula o partícula en el campo de visión, con el propósito de mostrar que esta aplicación es aceptable.

Palabras clave: procesamiento digital de imágenes, LabVIEW, distribución de tamaños, contador de células.

pp. 125–130; rec. 2017-05-17; acc. 2017-11-17

T. Córdova Fraga, J. A. Álvarez Gutiérrez, C. R. Contreras Gaytán, J. F. Gómez Aguilar, et al.

Digital Image Processing with LabVIEW: Applications in Biological Systems and Nanomaterials

Abstract. Images have been used for several decades as a tool for the identification or quantification of certain physical properties. In the field of medicine, they have been applied for the identification of malformations, tumors, fractures, among others. The algorithms implemented in this work are: opening and cutting of image section, filtering operators and pixel quantification. They are used to create a virtual application in the LabVIEW programming environment (LV) as a utility model that applies different algorithms to measure, quantify and determine the differences of changes and shapes in the images that were obtained through a microscope using three different amplifications. In this application, we work with images of cells obtained from the femur of an animal and the quantification of the size distribution of nanomaterials by measuring the individual areas of each cell or particle in the field of vision, in order to show that this application is acceptable.

Keywords: digital image processing, LabVIEW, size distribution, cell counter.

1. Introducción

Podría considerarse que el procesamiento digital de imágenes (PDI), inicia en 1921, con la codificación de la primera fotografía para su transmisión de datos a través del cable submarino entre las ciudades de Londres y Nueva York. La resolución de las imágenes ha ido evolucionando durante el tiempo en función del desarrollo de las nuevas tecnologías de hardware [1].

De igual manera el desarrollo de los lenguajes de programación, los sistemas operativos y las plataformas de Windows han hecho posible el crecimiento continuo de aplicaciones relacionadas al procesamiento digital de imágenes, tales como: imágenes médicas, satelitales, astronómicas, geográficas, arqueológicas, biológicas y aplicaciones industriales, entre otras [2].

Por otro lado, se sabe que la teoría de las primeras técnicas de procesamiento digital de imágenes se desarrolla en el Laboratorio de Propulsión a Chorro, Massachusetts Institute of Technology, de los Laboratorios Bell, de la Universidad de Maryland desde la década de 1960 y algunas otras instalaciones de investigación, con aplicación a las imágenes, alambre-photo conversión de normas por satélite, imágenes médicas, videoteléfono, el reconocimiento de caracteres y el mejoramiento fotografía. El costo del tratamiento fue en su momento bastante alto, sin embargo, con los equipos informáticos de la época, esto cambió a partir de la década de 1970, cuando el procesamiento de imágenes digitales proliferó con el incremento en la disponibilidad de las computadoras y hardware dedicado llegó al PDI, lo que permitió que las imágenes pudieran ser procesadas en tiempo real, para algunos problemas específicos, tales como la conversión de normas de televisión. Mientras que las computadoras de propósito general se hicieron más rápidas, comenzaron a asumir el papel de un hardware dedicado para todos [3].

Fig. 1. Izquierda: Selección de una porción de la imagen para el PDI, Centro: Equalización de la imagen seleccionada. Derecha: Se muestra la imagen con un filtrado (Square) cuadrado.

Un sistema de visión artificial actúa sobre una representación de una realidad que le proporciona información sobre brillo, colores, formas, etc. Estas representaciones suelen estar en forma de imágenes estáticas, escenas tridimensionales o imágenes en movimiento. La digitalización, es el proceso de paso del mundo continuo (o analógico), al mundo discreto (o digital), mediante el cual se genera una imagen bidimensional, que es una función para cada par de coordenadas (x, y), que se le asocia un valor relativo a alguna propiedad del punto que representa (por ejemplo, su brillo o su matiz) [4].

Este proyecto está enfocado en comparar imágenes, con la finalidad de verificar las diferencias de cambios en cada una de ellas. Partiendo de un concepto de visión artificial, se pretende dar una explicación de cómo cargar, contrastar, filtrar y contabilización la binarización de imágenes mediante el uso de las herramientas de LabVIEW e IMAQ Visión, para facilitar el tratado de las imágenes y tener salidas como una distribución de áreas de los tamaños de las nanopartículas y las células.

2. Análisis y digitalización de imágenes (ADI)

El análisis digital de imágenes (ADI) es una herramienta capaz de procesar y de analizar los objetos que forman una imagen de interés para un estudio específico. El ADI es un método de evaluación simple, no invasivo y no destructivo, que proporciona información en un tiempo determinado con el fin de caracterizar diversos tipos de formas irregulares, que tienen determinada similitud entre sí, logrando cuantificar cualidades en los objetos [5]. Algunas aplicaciones se han desarrollado enfocadas a diferentes cuantificaciones, tales como el conteo de células tipo T, glóbulos rojos o el Frotis de sangre que requieren determinar la cantidad de células presentes en una muestra, esto con el fin de descartar o confirmar la presencia de alguna enfermedad o cuando el médico sospecha de una anomalía de algún tipo de célula. Uno de los métodos que se emplea en la actualidad se denomina el de la Cámara de contaje celular o Cámara de Neubauer. La exactitud y la velocidad con que se obtiene el resultado de este examen dependen en parte, de la experiencia de la persona que examina la muestra, ya que el conteo se realiza de forma manual [6, 7, 8].

Considérese a la imagen como un objeto plano con representación bidimensional o matriz numérica, donde la resolución de la imagen es estática/dinámica y puede ser un mapa de bits o un gráfico vectorial. El mapa de bits es utilizado en PDI ya que puede ser manipulada por una herramienta informática.

Fig. 2. Izquierda: Segmentación por umbralización, Centro: Rellenar huecos, Derecha: Remover objetos pequeños.

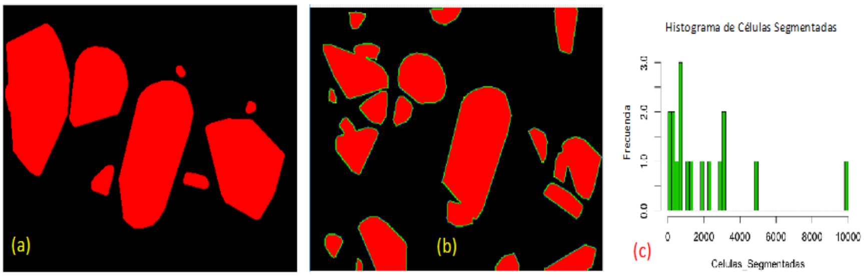

Fig. 3. (a) Redondeo envolvente y rellenado de huecos en los objetos, (b): Determinación de área, (c): Histograma de áreas de segmentos de cuadro (b).

Una imagen monocromática es representada como una función continua f (x, y), donde (x, y), son sus coordenadas y el valor de f es proporcional a la intensidad de luminosidad (pixel) o niveles de gris, en ese punto [9-10].

El procesamiento digital de Imágenes en LV se realiza mediante el uso del módulo de visión y la plataforma de visión builder, en donde se permite procesar en diferentes formatos de imagen (BMP, JPEG, TIF o PNG). Además de experimentar y acondicionar los diferentes algoritmos a nuestro análisis de interés.

3. Resultados

Para el conteo de células se selecciona una región de 400 × 300 pixeles de una imagen de células fue seleccionada y con una resolución de 200 pp. Fig. 1. Una ecualización de cada segmento seleccionado permite la distribución de las distintas tonalidades y ayuda a controlar la exposición en muestras de fotografías, corregir los colores y determinar el contraste o exposición de una imagen digital.

Esta ecualización ayuda en el proceso de filtrado para eliminar elementos de no interés en la sección de análisis. También se hizo un mejoramiento de contraste y brillo mediante Lookup Table y una estandarización con la función Square para reducir el contraste en las regiones oscuras de la región de interés y exponer un efecto más gradual, ver Fig. 1.

Utilizado el algoritmo erosionar se pudo reducir el brillo en los pixeles que se encuentran rodeados por otros con una intensidad más baja.

Con ello se realizó una segmentación por umbralización y así poder hacer diferentes transformaciones morfológicas sobre las imágenes binarias.

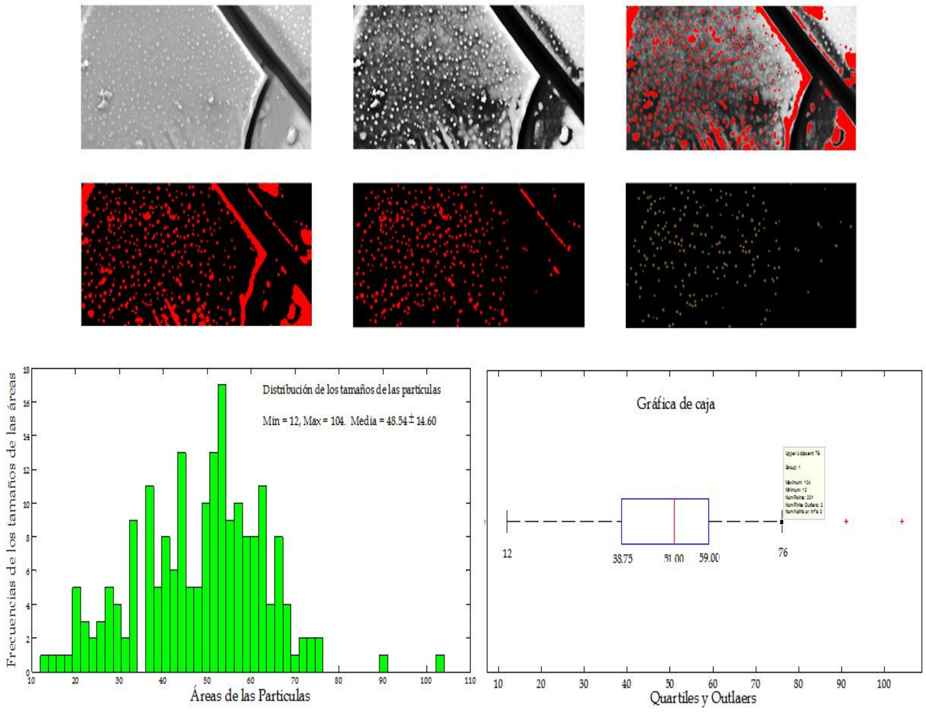

Fig. 4. Esquematización del procesamiento digital de imágenes y análisis gráfico estadístico de imágenes TEM.

Se utilizó una conectividad 4/8 para verificar la adyacencia entre los pixeles y poder remover los objetos pequeños erosionados. Posteriormente se aplicó un redondeo envolvente y fueron rellenados los huecos en cada objeto de interés. (Fig. 3)

Para el análisis de nanopartículas, a partir de una imagen del microscopio de trasmisión electrónica (TEM), donde se aplica un procedimiento de imágenes similar al previo, se puede llegar a una gráfica de distribución de los tamaños (cuadro de histogramas), donde se complementa con una gráfica de caja que da información precisa de la distribución de estos tamaños.

4. Discusión/Conclusión

Se ha mostrado que la implementación de la rutina en ambiente LabVIEW para el procesamiento digital de imágenes aquí discutida puede ser útil para la cuantificación de células y determinación de su área, lo que permite tener una cuantificación en grupo control vs. grupo experimental en experimentos de proliferación celular.

Por otro lado, este mismo procedimiento se puede usar para determinar el área de nanopartículas y con los registros de estas, tener una gráfica de distribución de tamaños que puede mostrarse en un histograma o bien en una gráfica de caja.

Agradecimientos. Los autores agradecen a la DAIP/proyectos 2016-59023.

Referencias

1. García, V. M.: Introducción al procesamiento digital de imágenes. Universidad Tecnológica de la Mixteca, pp. 1–5 (2009)
2. http://www.kramirez.net/Robotica/Material/Libros/VisionArtificial_Procesamientodigitalimágenes usando Matlab/Cap-III.pdf
3. Larcher, L. I., Biasoni, E. M., Cattaneo, C. A., Ruggeri, A. I.: Algoritmo para detección de bordes y ulterior determinación de objetos en imágenes digitales. Facultad de Agronomía y Agroindustrias, Universidad Nacional de Santiago del Ester, 1 (2011)
4. Moreira, Q. J., Valencia, D. V., Chávez, B. P.: Implementación de un Algoritmo para la detección y conteo de células en imágenes microscópicas. Facultad Ingeniería en Electricidad y Computación, 1 (2008)
5. Foster, I., Kesselman, C., Nick, J., Tuecke, S.: The Physiology of the grid: an open grid services architecture for distributed systems integration. Technical report, Global Grid Forum (2002)
6. Sabino, B. A., Márquez, J. A., Campos, J. M.: Segmentación de Células de la Levadura Saccharomyces cerevisiae. Temas de Ciencia y tecnologías. 1. (2011)
7. http://www.biologia.arizona.edu/cell/act/onion/activity_description.html. Proyecto Biológico-Biología Celular (1998)
8. http://www.slideshare.net/ingenieriageologica1/capitulo-vi-procesamiento-digital-de-una imagen (2013)
9. http://www.teledet.com.uy/tutorial-imagenes-satelitales/estructura-imagenes-digitales.htm (2013)
10. Atienza, V. V.: Histograma de una imagen digital. Informática de sistemas y computadores (DISCA). Universidad Politécnica de Valencia (2013)

ISSN 1870-4069

Digital Mammography and Thermography Processing for Breast Cancer Detection

C.M. Gómez-Sarabia[1], R. Guzmán Cabrera[2], J.R. Guzmán-Sepúlveda[3],
M. Torres-Cisneros[4], J. Ojeda Castañeda[4]

[1] Universidad de Guanajuato, Digital Arts Department, DICIS, Salamanca, Guanajuato, Mexico

[2] Universidad de Guanajuato, Electrical Engineering Department, DICIS, Salamanca, Guanajuato, Mexico

[3] University of Central Florida, CREOL, The College of Optics and Photonics, Orlando, FL, USA

[4] Universidad de Guanajuato, Electronics Department, DICIS, Salamanca, Guanajuato, Mexico

maggie_gomezsa@yahoo.com, guzmanc81@gmail.com, jrafael_guzmans@yahoo.com.mx,
mtorres37@me.com, jorge_ojedacastaneda@yahoo.com

Abstract. Primary prevention in early stages of breast cancer becomes crucial for diagnosis and, at the same time, complicated to achieve since the causes remain practically unknown. X-ray mammography is the most widely used screening technique due to cost effectiveness and its capability to provide valuable structural information thus allowing detection of characteristic cancer signatures such as masses and microcalcifications. Recently, thermography has gained a lot of interest since it has been demonstrated to be a non-invasive technique capable of revealing the health condition of the breasts in terms of physiological changes due to cancer formation. In this paper an approach based on intensity-based segmentation by means of morphological operators is proposed in order to detect regions potentially containing cancer in digital mammograms and thermograms. The algorithm is tested over several images taken from the Digital Database for Screening Mammography and the American College of Clinical Thermography, and the results suggest that the proposed algorithm is a suitable tool to successfully identify and extract regions of interest in a variety of environments and conditions, among which are several types of cancer and different image angles.

Keywords: breast cancer, digital image processing, mammography, thermography.

1 Introduction

Breast cancer is the most common cause of death in women and the second leading cause, after lung cancer, of death around the world [1-2]. The risk of a woman developing invasive breast cancer at some time in her life is about 12% [3]: the National

Cancer Institute of Canada estimates that 1 in 9 women will develop breast cancer and that 1 in 27 will die from this disease [4], while the incidence of developing breast cancer in the United Stated is estimated to be 1 in 8 women [5]. There is not an effective way to prevent and avoid breast cancer since the causes remain practically unknown; therefore, early detection plays a major role in diagnosis and treatment.

In this regard, the most recent advances in early detection include techniques such as digital mammography, tomosynthesis, contrast-enhanced mammography, screening ultrasound, and contrast-enhanced magnetic resonance imaging (MRI) [6]. None of these techniques have demonstrated to be completely satisfactory; however some specific conditions have been discovered to be determinant in the selection of the appropriate technique in order for the performance to be more effective.

For instance, MRI has been demonstrated to be more sensitive than mammography in high-risk patients and the combination of these two would be advisable in this case; screening ultrasound is suggested in patients having a high-risk condition who cannot tolerate MRI; and ultrasound screening together with supplemental screening techniques is recommended for intermediate-risk patients and women with dense breasts.

Some other imaging modalities for breast cancer screening, such as breast-specific gamma imaging and positron emission mammography, have not been supported mainly due to the radiation doses, which are 15 to 30 times higher than the dose from digital mammography [7].

In order to improve the accuracy and efficiency of the diagnosis in breast imaging, Computer-Aided Diagnosis (CAD) has been introduced within the screening process to support radiologists and internists in terms of image interpretation. CAD systems aim to complement the screening techniques and they can be found mainly in two forms depending on their purpose: Computer-Aided Detection (CADe) and Computer-Aided Diagnosis (CADx). The latter are oriented at image classification (i.e. malignancy, benignity) while CADe systems are focused on identifying regions of interest (i.e. suspicious regions) thus providing a second opinion on potentially abnormal regions that may contain breast cancer [8].

In this work, a CADe scheme is proposed to effectively analyze digital mammograms and thermograms based on texture segmentation for the detection of early stage tumors and cancerous activity. Regarding mammography, the algorithm was tested on several images taken from the Digital Database for Screening Mammography (DDSM) [9-10] while thermography images were taken from the website of the American College of Clinical Thermography (ACCT) [11].

The identification of the regions of interest (i.e. image segmentation) is done by means of morphological operators and the extraction is then performed through machine learning techniques and the clustering algorithm for intensity-based segmentation. In both cases the images were previously hand-labeled and classified by specialists thus allowing a reliable clinical baseline.

The results show that the proposed CADe algorithm is a suitable tool for qualitative evaluation of both digital mammograms and thermograms, since it allows effective processing to successfully extract the regions of interest where the characteristic signatures of breast cancer can be found.

2 Mammography and Thermography

To date X-ray mammography is the most widely used technique in clinical practice due to its low cost and accessibility and it is actually the only method shown to decrease mortality in two-thirds of studies. Direct data shows a mortality decrease of 30% in the United States since the advent of mammography [12].

Although screening mammography exhibits some limitations, such as low reliability among young women or women who have undergone surgery, the debatable rate of “overdiagnosis”, and the dependence of the sensitivity on the density of the breast tissue [13-16], it is recognized as the most effective method for early detection of breast cancer since it provides high sensitivity on fatty breasts and good performance on micro-calcification detection [17]. Some health, medical, and professional agencies and societies, among which are the American Cancer Society (ACS), the American College of Radiology (ACR), the Centers for Disease Control and Prevention (CDCP), the National Cancer Institute (NCI), and the Society of Breast Imaging (SBI) [18], agree with the Food and Drug Administration (FDA) [19] that mammography is the most effective method for breast cancer detection in its earliest, most treatable stages [20].

In addition to cost effectiveness and accessibility, mammography gained popularity in the last decade due to several improvements on image-processing methods proposed to address the problem of tumor detection. These improvements include a large variety of techniques among which the most widely studied are those based on wavelet transforms and machine learning. In terms of techniques based on wavelet transforms, proposals using fractal analysis, discrete wavelet transform, and Markov random fields can be found in the literature [21]. On the other hand, regarding machine learning techniques, some relevant proposals include a neural network architecture based on multiple circular path convolutions for the analysis of tumor and tumor-like structures [22], as well as a two-stage adaptive density-weighted contrast enhancement algorithm for tumor detection [23].

However, the great need for non-invasive methods makes screening techniques such as thermography of interest to specialists. Thermography is a biologically inert method that screens the temperature distribution across the skin surface and it is based on the biological characteristic of the temperature increase of the tissue due to a rise in the metabolic activity (i.e. carcinogenesis).

Studies on thermographic breast imaging have been reported prior [24] and recent studies demonstrate that thermography performs better compared to mammography: thermography has a sensitivity of 100%, specificity of 79%, and proportion of true results of 92%, compared to sensitivity of 85%, specificity of 84%, and proportion of true results of 85% for mammography [6].

Unlike mammography, thermography has not been validated as a screening or adjunctive diagnostic tool, neither by the SBI nor the FDA, due to the lack of conclusive evidence and the sensitivity of the results to statistical treatment [25].

Nevertheless, the bottom line is that thermography is a non-invasive technique to monitor breast health (i.e. no radiation or breast compression involved) and it offers crucial advantages over mammography such as the capability to detect hormonal imbalances and physiologic changes related to cancer while in cellular phase, years before it is detectable by means of mammographic techniques. Furthermore, based on the fact that only 25% of the cases have a genetic component [12], the characteristics mentioned above make thermography a suitable assessment tool since the risk of developing breast cancer is significantly modifiable in early stages.

3 Method

The identification of regions of interest related to breast cancer is performed by means of texture analysis, which depends not only on the image itself but also on the purpose for which it is used [21]; and indeed, it has been demonstrated that the dataset itself can be significantly influential on the results [17].

The proposed algorithm deals with 8-bit gray-scale images obtained from the Digital Database for Screening Mammography (DDSM) [9-10] and the website of the American College of Clinical Thermography (ACCT) [11]. Based on the fact that abnormalities in the breast tissue are represented by regions of the image with their own properties, different from the general characteristics of the rest of the image [26-28], the image analysis is focused on regional properties such as texture and intensity variations. Texture differences, encoded in the transition regions, are then identified by means of morphological analysis and, in this particular case, an entropy-based algorithm is preferred over a gradient-based one due to the several intensity changes that take place in a single transition region [27].

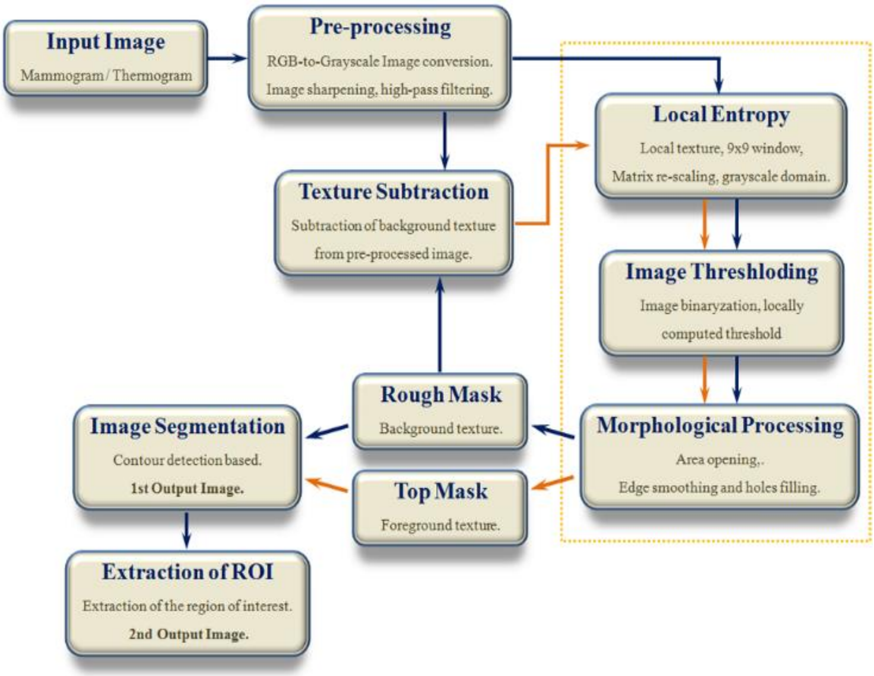

Fig. 1. General flowchart of the proposed algorithm.

Fig. 1 shows a general flowchart of the proposed algorithm containing the main stages of the process: image preprocessing, identification of the background texture, identification of the texture of the region of interest (ROI), and results display.

The preprocessing stage consists of image sharpening, only, in order to enhance the details in the input image and it is not strictly required. The blocks inside the box are the most important ones since the texture analysis is performed in these stages; they will be further explained in detail. It can be noticed from the diagram that the background texture is used as a contrast mask to identify the ROIs, consequently the rough mask (i.e. background texture) directly determines what is identified as "abnormal" in the top mask (i.e. textures of ROIs).

The first critical stage in the proposed algorithm is the computation of the local entropy of the image. According to the literature, the local entropy of a small region $\boldsymbol{\Omega_k}$ within the image, with dimensions (window size) $\mathbf{M_k} \times \mathbf{N_k}$, is defined as follows [27-28]:

$$E(\Omega_k) = -\sum_{i=0}^{L-1} P_i \log(P_i), \tag{1}$$

where:

$$P_i = \frac{n_i}{M_k \times N_k} \tag{2}$$

is the probability of occurrence of the discrete intensity **i** in the neighborhood $\boldsymbol{\Omega_k}$ and $\mathbf{n_i}$ is the number of pixels in the neighborhood that happen to have intensity of **i**. **L** is the maximum discrete intensity and $\mathbf{E(\Omega_k)}$ is the local entropy of the windowed region.

The discrete intensity **i** is defined as a global parameter and can be adjusted to be close to the intensity of the region where the abnormality is suspected to be. A 9x9 sized window was used to compute the local entropy and the texture properties were defined only by the adjacent neighbors of the actual pixel.

After the local entropy of the image is computed using Eq. (1)-(2), a primitive version of the background texture is available, however, in order to use the background texture as a contrast mask, a binarization process takes place right after computing the local entropy.

Subsequent intermediate stages constituting the morphological treatment will determine the final version of the background texture. Firstly, a process of area opening is performed to remove the "small objects"; then edges smoothing (i.e. dilation followed by erosion) using a square 9x9 mask takes place; finally, the binary mask is filled by connecting the isolated background pixels.

The binary mask obtained in previous stages based on the background texture is now used to subtract the background component from the input image. After subtraction, the same texture analysis (stages inside the box) is performed over the non-background image using the same parameters than in the case of the background texture. The regions filtered by the binary mask (background) do not contribute to or affect the results related to the ROIs since the local entropy is minimal for regions consisting of pixels with the same intensity [29].

The morphological treatment of the binary image obtained for the ROIs consists of the same intermediate processes than in the previous case but, unlike the background texture case, the thresholding of the non-background region is performed using a local threshold considering the image where the background is ignored. Once the binary mask of the ROIs is obtained, the contours of the ROIs are outlined for the output (i.e. segmented and extracted), and images are displayed.

4 Results

The proposed algorithm was tested on both mammographic and thermographic images that allow qualitatively illustration of its performance under a variety of conditions.

As mentioned before, the input images in all cases are 8-bit gray-scale images; in the case of mammograms, the images were obtained from the Digital Database for Screening Mammography (DDSM) [9-10] while the thermograms were obtained from the website of the American College of Clinical Thermography (ACCT) [11].

4.1 Breast Mammography

The mammograms upon which the proposed algorithm was tested were previously analyzed, diagnosed, classified, and hand-labeled by specialists. The images processed include marks indicating the actual location of the lesions but, as it will be seen later, the algorithm is insensitive to the hand-made label and the ROIs can be successfully identified and extracted.

Fig. 2 shows the main results of the segmentation and extraction processes for a mammogram diagnosed with malign cancer. Fig. 2a shows the original image, which highlights the abnormal region, while Figs. 2b-c show the segmented and extracted images. The original image was converted from RGB to gray-scale by forming a weighted sum of the R, B, and G components with the respective standard coefficients 0.2889, 0.5870, and 0.1440.

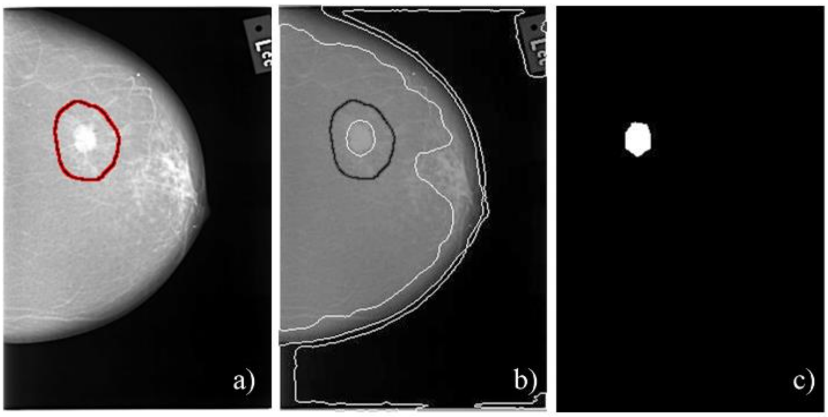

Fig. 2. Digital image processing of a mammogram diagnosed with malign breast cancer. (a) Original hand-labeled image, (b) segmented image, and (c) extracted image. Volume 02 – Case C0037 – Left CC [9-10].

In this particular case, the segmentation and extraction were found to be successful for a relative threshold intensity of 0.750 and a reference opened area of 250 pixels.

One single ROI, with area of 535 pixels, was successfully extracted and, as can be confirmed by Fig. 2b, the hand-made label does not contribute, interfere, or affect the segmentation: the contour of the ROI can be outlined independently from the label.

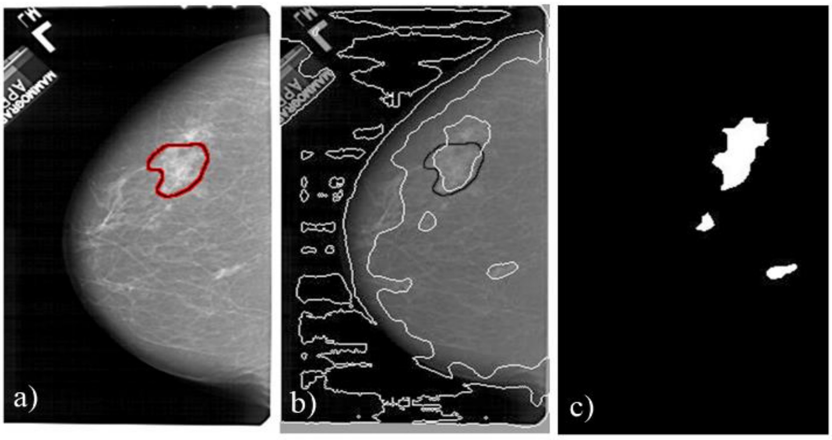

Fig. 3. Digital image processing of a mammogram diagnosed with benign breast cancer. (a) Original hand-labeled image, (b) segmented image, and (c) extracted image. Volume 02 – Case A1237 – Left CC [9-10].

The fact that the ROI found by the proposed algorithm is smaller than that defined by the hand-made label can be explained based on the fact that the label encloses a larger area than that occupied by the lesion while the lesion in this case is well defined, significantly non-outspread, and located over a region with considerably clear boundaries, appreciable by naked eye.

The second case study is a mammogram diagnosed with benign cancer. Fig. 3 shows the results of the segmentation and extraction processes. In similar fashion to the previous case, Fig. 3a shows the original image, which highlights the lesion, while Figs. 3b-c show the segmented and extracted images, respectively. The original image was converted from RGB to gray-scale using the same standard set of coefficients.

Contrary to the previous case, the lesion is not clearly defined and the hand-made label encloses an outspread region with undefined boundaries. However, the segmentation and extraction processes were found to be successful for a relative threshold intensity of 0.762 and a reference opened area of 200 pixels.

In this case, three different ROIs were found over the image with similar texture properties. The total area of the ROIs is 1763 pixels and, once again, the ROIs can be successfully identified independently from the hand-made label.

Unlike the previous case, the largest ROI found extends over a considerably larger region than that defined by the hand-made label. Moreover, the proposed algorithm found two more regions having the same texture than that from the lesion that were not previously identified. This does not mean that the additional regions also contain benign cancer but it means that in terms of texture characteristics these regions have similar properties; further analysis is required to diagnose the additional regions.

4.2 Breast Thermography

The thermograms over which the proposed algorithm was tested were previously analyzed, diagnosed, and classified by specialists; in this case the images are not hand-labeled.

The fact that the thermogram screens the temperature distribution across the skin surface and not the structural properties of the breast tissue leads to specific implications that are to be taken into account further in the processing. The value of the threshold intensity around which the texture analysis is performed is expected to be higher only due to the color scale used in the pseudo-coloring process: the higher temperatures, meaning the regions containing the lesions, are closer to white.

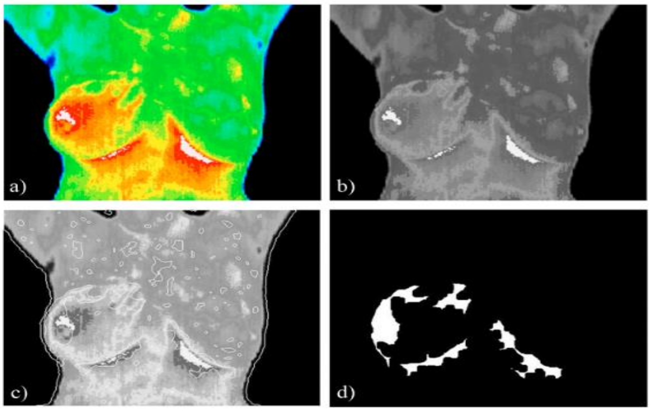

Fig. 4. Digital image processing of a thermogram diagnosed with inflammatory breast cancer [11]. a) Original pseudo-colored image, b) gray-scale image, c) segmented image, and d) extracted image.

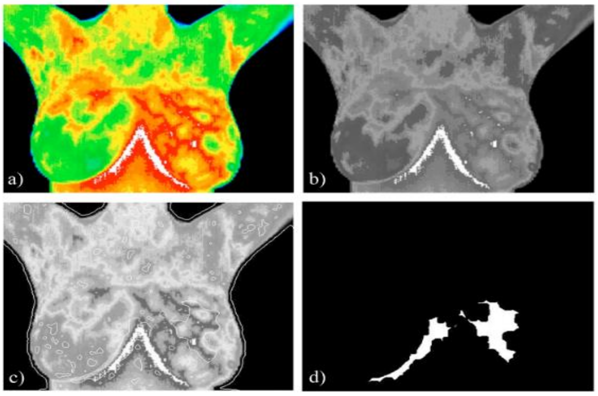

Fig. 5. Digital image processing of a thermogram diagnosed with breast fibrosis [11]. a) Original pseudo-colored image, b) gray-scale image, c) segmented image, and d) extracted image.

On the other hand, in terms of the ROIs themselves, much larger regions are expected to be extracted due to the fact that temperature distributions gradually extend over larger areas, leading to smooth transition regions between the background and the ROIs, then resulting in outspread and geometrically undefined regions.

Fig. 4 shows the main results of the segmentation and extraction processes for a thermogram diagnosed with inflammatory breast cancer. Fig. 4a-b show the original pseudo-colored and gray-scale images, respectively; while Figs. 4b-c show the processed images, segmented and extracted, respectively. The original pseudo-colored image was converted from RGB to gray-scale using the standard set of coefficients mentioned before.

In this particular case, the segmentation and extraction were found to be successful for a relative threshold intensity of 0.830 and a reference opened area of 1000 pixels. Several ROIs, with total area of 8060 pixels, were successfully extracted.

The second case study is a thermogram diagnosed with breast fibrosis. Fig. 5 shows the main results of the segmentation and extraction processes. Fig. 5a-b show the original pseudo-colored and gray-scale images, respectively, while Figs. 5b-c show the segmented and extracted processed images, respectively. The original pseudo-colored image was converted from RGB to gray-scale using the same standard set of coefficients.

In this particular case, the segmentation and extraction were found to be successful for a relative threshold intensity of 0.840 and a reference opened area of 1400 pixels. Several ROIs, with total area of 6885 pixels, were successfully extracted.

5 Conclusions

In this paper a texture segmentation approach is demonstrated for the detection of regions potentially containing cancer in both digital mammograms and thermograms. The proposed Computer-Aided Detection (CADe) system, consisting mainly of intensity-based segmentation by means of morphological operators, was tested on several images from the Digital Database for Screening Mammography and the American College of Clinical Thermography. Both cases have a reliable clinical baseline as the images were previously hand-labeled and classified by specialists.

In the case of mammography two case studies, diagnosed with malign and benign cancer, respectively, are reported; while regarding thermography, the case studies reported are diagnosed with inflammatory cancer and fibrosis, respectively. This variety of cases allows testing the effectiveness and robustness of the proposed algorithm; the obtained results show actual, successful, segmentation and extraction of the regions of interest in all the cases.

The input parameters of the algorithm are reference values of the normalized intensity and area of the regions that are to be found. In this regard, there are significant differences for mammograms and thermograms, due only to the nature of the screening techniques: both the reference intensity and the area are significantly larger in the case of thermograms due to the pseudo-coloring and the smoothness of the transitions between the background and the ROIs, respectively.

In the particular case of mammography, the mammogram diagnosed with malign cancer was successfully processed and the extracted ROI just confirmed the hand-labeling. Unlike this case, the mammogram diagnosed with benign cancer does not have a well-defined lesion and, in fact, the extracted ROI extends over a larger area than that of the hand-labeling. Moreover, as a result of the processing, additional ROIs not present in the hand-labeling were found to have identical texture properties than those of the lesion.

In the case of thermography, both case studies present thermograms with large ROIs having smooth transition regions between ROIs and background. The algorithm still operates successfully over the thermograms and, despite that the ROIs do not have well defined boundaries, a significant correlation between the original and extracted images can be qualitatively depicted.

Overall, the proposed CADe algorithm is demonstrated to be stable and robust while processing breast images with a variety of different characteristics resulting in a reliable and suitable tool for the qualitative evaluation of both digital mammograms and thermograms.

References

1. Deserno, T. M.: Biomedical Image Processing. Springer, Berlin (2010)
2. Garcia, M., Jemal, A., Ward, E., Center, M., Hao, Y., Siegel, R., Thun, M.: Global, Cancer Facts & Figures. American Cancer Society, Atlanta, GA (2007)
3. Breast Cancer Statistics. Available: http://www.breastcancer.org (2009)
4. Canadian cancer statistics. Canadian Cancer Society/National Cancer Institute of Canada, available: http://www.cancer.ca or http://www.ncic.cancer.ca (2013)
5. Probability of breast cancer in American women. National Cancer Institute, available: http://www.cancer.gov/cancertopics/factsheet/Detection/probability-breast-cancer (2013)
6. Kolarić, D., Herceg, Z., Nola, I. A., Ramljak, V., Kuliš, T., Katančić-Holjevac, J., Antonini, S.: Collegium Antropologicum. 37(2), pp. 583–588 (2013)
7. Mainiero, M. B., Lourenco, A., Mahoney, M. C., Newell, M. S., Bailey, L., Barke, L. D., Haffty, B. G.: J. Am. Coll. Rad. 10(1), pp. 11–14 (2013)
8. Giger, M. L., Karssemeijer, N., Schnabel, J. A.: Annual review of biomedical engineering. 0 (2013)
9. Heath, M., Bowyer, K., Kopans, D., Moore, R., Kegelmeyer, W. P.: The Digital Database for Screening Mammography. In: Proceedings of the Fifth International Workshop on Digital Mammography, M.J. Yaffe, ed., Medical Physics Publishing, pp. 212–218 (2001)
10. Heath, M., Bowyer, K., Kopans, D., Kegelmeyer, W. P., Moore, R., Chang, K., Munish-Kumaran, S.: Current status of the Digital Database for Screening Mammography. In: Proceedings of the Fourth International Workshop on Digital Mammography, pp. 457–460 (1998)
11. http://www.thermologyonline.org/index.html, American College of Clinical Thermography (ACCT).
12. Hudson, T., Poulsen, C. A.: Brush and Quill Productions. Journey to Hope, 2nd Ed (2011)
13. Calonge, N., Petitti, D. B., DeWitt, T. G., Dietrich, A. J., Gregory, K. D., Grossman, D., Wilt, T.: Annals of Internal Medicine. 151(10), pp. 716-W236 (2009)
14. Kopans, D. B., Smith, R. A., Duffy, S. W.: Radiology. 260(3), pp. 616–620 (2011)
15. Smith, R. A., Duffy, S. W., Tabár, L.: Oncology. 26(5), pp. 471–475 (2012)
16. Jørgensen, K. J., Keen, J. D., Gøtzsche, P. C.: Radiology. 260(3) pp. 621–627 (2011)
17. Bottema, M. J., Lee, G. N., Lu, S.: Series in Machine Perception and Artificial Intelligence. 39, pp. 17–54 (2000)
18. Food and Drug Administration. FDA, available: http://www.fda.gov
19. Society of Breast Imaging. SBI, available: http://www.sbi-online.org

20. http://www.fda.gov/MedicalDevices/Safety/AlertsandNotices/ucm257259.htm
21. Zheng, L., Chan, A. K.: IEEE Trans. Med. Imaging. 20(7), pp. 559–567 (2001)
22. Li, H., Shih-Chung, B.L., Wang, Y., Kinnand, L., Freedman, M. T.: IEEE Trans. Med. Imaging. 21(2), pp. 150–158 (2002)
23. Chan, H. P., Petrick, N., Sahiner, B.: Computer-aided breast cancer diagnosis: artificial intelligence techniques in breast cancer diagnosis and prognosis series in machine perception and artificial intelligence. World Scientific Publishing Co. Pte. Ltd., 39, pp. 179–264 (2000)
24. Feig, S. A., Shaber, G. S., Schwartz, G. F., Patchefsky, A., Libshitz, H. I., Edeiken, J., Wallace, J. D.: Radiology. 122(1), pp. 123–127 (1977)
25. Brkljačić, B., Miletić, D., Sardanelli, F.: Collegium Antropologicum. 37(2), pp. 589–593 (2013)
26. Gerbrands, J. J.: Segmentation of noisy images. Ph.D. Dissertation, Delft University, The Netherlands (1988)
27. Yan, C., Sang, N., Zhang, T.: Pattern Recognition Lett. 24, pp. 2935–2941 (2003)
28. Gonzalez, R. C., Woods, R. E., Eddins, S. L.: Digital Image Processing Using MATLAB. Prentice Hall, Chap. 11 (2003)
29. Thum, C.: Optica Acta: Int. J. Optics, 31(2), pp. 203–211 (1984)

Impreso en los Talleres Gráficos
de la Dirección de Publicaciones
del Instituto Politécnico Nacional
Tresguerras 27, Centro Histórico, México, D.F.
enero de 2017
Printing 500 / Edición 500 ejemplares